



**HAL**  
open science

# Vibroacoustic modelling of aircraft double-walls with structural links using Statistical Energy Analysis (SEA)

Bruno Campolina

► **To cite this version:**

Bruno Campolina. Vibroacoustic modelling of aircraft double-walls with structural links using Statistical Energy Analysis (SEA). Acoustics [physics.class-ph]. Université de Sherbrooke; Université Pierre et Marie Curie - Paris VI, 2012. English. NNT: . tel-00736619

**HAL Id: tel-00736619**

**<https://theses.hal.science/tel-00736619>**

Submitted on 28 Sep 2012

**HAL** is a multi-disciplinary open access archive for the deposit and dissemination of scientific research documents, whether they are published or not. The documents may come from teaching and research institutions in France or abroad, or from public or private research centers.

L'archive ouverte pluridisciplinaire **HAL**, est destinée au dépôt et à la diffusion de documents scientifiques de niveau recherche, publiés ou non, émanant des établissements d'enseignement et de recherche français ou étrangers, des laboratoires publics ou privés.





UNIVERSITÉ DE SHERBROOKE  
Faculté de génie  
Département de génie mécanique  
Sherbrooke (Québec) Canada  
Spécialité : génie mécanique

UNIVERSITÉ PIERRE ET MARIE CURIE  
École doctorale SMAER (ED 391)  
Sciences mécaniques, acoustique, électronique & robotique de Paris  
Paris, France  
Spécialité : acoustique

MODÉLISATION VIBROACOUSTIQUE DE  
DOUBLE-PAROIS AÉRONAUTIQUES  
AVEC LIENS MÉCANIQUES PAR LA  
MÉTHODE DE L'ANALYSE STATISTIQUE  
ÉNERGÉTIQUE

VIBRO-ACOUSTIC MODELLING OF AIRCRAFT  
DOUBLE-WALLS WITH STRUCTURAL LINKS USING  
STATISTICAL ENERGY ANALYSIS

Thèse de doctorat (cotutelle)

Bruno L. CAMPOLINA

Jury:	Nicolas DAUCHEZ,	SUPMECA	Co-directeur
	Noureddine ATALLA,	U. de Sherbrooke	Co-directeur
	Pascale NEPLE,	Airbus Operations SAS	Co-encadrante
	Jean-Louis GUYADER,	INSA Lyon	Rapporteur
	Alain BERRY,	U. de Sherbrooke	Rapporteur
	Vincent MARTIN,	CNRS/UPMC	Président
	José R. F. ARRUDA,	UNICAMP	Examineur
	Marshall DOWNING,	LORD Corporation	Examineur

Juillet 2012



# RÉSUMÉ

La prédiction du bruit intérieur des avions nécessite la modélisation vibroacoustique de l'ensemble fuselage et traitements acoustiques. Cet ensemble est composé d'un panneau raidi métallique ou composite, sur lequel est posé un traitement thermo-acoustique (laine de verre) et connecté par des liens anti-vibratiles à un panneau d'habillage de type sandwich nid d'abeille. L'objectif de ce travail consiste à optimiser les traitements acoustiques en prenant en compte les contraintes de design telles que la masse et les dimensions. A ce propos, une double-paroi représentative d'avion est modélisée par la méthode de l'analyse statistique énergétique (SEA). Des excitations académiques telles que le champ diffus et la force ponctuelle sont utilisées et des tendances sont données pour des applications sous excitation aérodynamique, du type couche limite turbulente.

Une première partie porte sur l'effet de compression d'une couche poreuse. Pour des applications aéronautiques, la compression de ce type de matériaux peut se produire lors de l'installation d'équipements et câbles. Elle est étudiée, de manière analytique et expérimentale, pour une simple-paroi recouverte par une couche de matériau fibreux. Le matériau est comprimé sur toute sa surface. Une réduction de la perte par transmission (TL) jusqu'à 5 dB est observée principalement en moyennes fréquences (autour de 800 Hz) lorsque l'épaisseur du poreux est comprimé de 50%. Cependant pour des cas plus réalistes, cet effet est supposé moins important pour une compression locale et plus faible.

Dans une seconde partie, la transmission par les connections structurales entre panneaux est étudiée par une approche quadripolaire qui relie la paire force-vitesse de chaque côté du lien mécanique. La modélisation intègre la raideur dynamique mesurée par un banc d'essai dédié. La transmission structurale est par la suite validée avec des essais et intégrée au modèle de double-paroi comme un facteur de couplage entre panneaux. Comme les structures sont non-courbées, seule la transmission axiale est considérée.

Enfin, les voies de transmission dominantes sont identifiées dans la gamme de fréquences entre 100 Hz et 10 kHz pour des double-parois sous champ diffus et sous excitation structurale ponctuelle. La transmission non-résonante est plus importante en basses fréquences (jusqu'à 1 kHz) alors que les parties structurale et aérienne dominant respectivement en moyennes et hautes fréquences. Une validation avec des résultats expérimentaux montre que le modèle est capable de prédire les changements au niveau de la transmission, causés par les différents couplages structuraux (couplage rigide, couplage via liens anti-vibratiles et découplage structural). Des différentes solutions en termes de traitement acoustique, comme par exemple l'absorption, l'amortissement et le découplage structural, peuvent par la suite être dérivées.

**Mots-clés :** Analyse statistique énergétique, Lien anti-vibratile, Double-paroi, Analyse de chemins de transfert, Perte par transmission.



# ABSTRACT

The prediction of aircraft interior noise involves the vibroacoustic modelling of the fuselage with noise control treatments. This structure is composed of a stiffened metallic or composite panel, lined with a thermal and acoustic insulation layer (glass wool), and structurally connected via vibration isolators to a commercial lining panel (trim). The goal of this work aims at tailoring the noise control treatments taking design constraints such as weight and space optimization into account. For this purpose, a representative aircraft double-wall is modelled using the Statistical Energy Analysis (SEA) method. Laboratory excitations such as diffuse acoustic field and point force are addressed and trends are derived for applications under in-flight conditions, considering turbulent boundary layer excitation.

The effect of the porous layer compression is firstly addressed. In aeronautical applications, compression can result from the installation of equipment and cables. It is studied analytically and experimentally, using a single panel and a fibrous uniformly compressed over 100% of its surface. When compression increases, a degradation of the transmission loss up to 5 dB for a 50% compression of the porous thickness is observed mainly in the mid-frequency range (around 800 Hz). However, for realistic cases, the effect should be reduced since the compression rate is lower and compression occurs locally.

Then the transmission through structural connections between panels is addressed using a four-pole approach that links the force-velocity pair at each side of the connection. The modelling integrates experimental dynamic stiffness of isolators, derived using an adapted test rig. The structural transmission is then experimentally validated and included in the double-wall SEA model as an equivalent coupling loss factor (CLF) between panels. The tested structures being flat, only axial transmission is addressed.

Finally, the dominant sound transmission paths are identified in the 100 Hz to 10 kHz frequency range for double-walls under diffuse acoustic field and under point-force excitations. Non-resonant transmission is higher at low frequencies (frequencies lower than 1 kHz) while the structure-borne and the airborne paths dominate at mid- and high-frequencies, around 1 kHz and higher, respectively. An experimental validation on double-walls shows that the model is able to predict changes in the overall transmission caused by different structural couplings (rigid coupling, coupling via isolators and structurally uncoupled). Noise reduction means adapted to each transmission path, such as absorption, dissipation and structural decoupling, may be then derived.

**Keywords:** Statistical energy analysis, Vibration isolator, Double-wall, Transfer path analysis, Transmission Loss.



# ACKNOWLEDGEMENTS

I thank M. Armand Malagoli, ex-responsible for the Airbus Acoustics & Environment department for accepting my application to integrate the Near-field & Interior noise team and start the present PhD thesis in collaboration with the University of Sherbrooke, the *Institut Supérieur de Mécanique de Paris* (Supméca), the University Pierre and Marie Curie (UPMC), and the *Association nationale de la recherche et de la technologie* (ANRT).

I would like to express my sincere gratitude to my thesis supervisors Pascale Neple, Near-field & Interior Noise research coordinator at Airbus; Nicolas Dauchez, professor at Supméca and Noureddine Atalla, professor at the University of Sherbrooke. Their valuable advices and attentive supervision were major contributors to the achievement of my objectives. I appreciate their availability, insightful discussions and expertise shared. I thank them also for encouraging my participation to several international conferences.

I address my acknowledgements to all the members of the thesis defence board for their participation as well as for the interest and time dispensed to this work. Special thanks go to Alain Berry and Jean-Louis Guyader for their detailed reports. Sören Callsen is acknowledged for his participation in the defence board during the defence presentation. Stéphane Moreau is also acknowledged for his advices during the pre-PhD examination.

Thanks to all my colleagues of the Acoustics & Environment department at Airbus, specially the Near-field & Interior noise team at Toulouse and Hamburg for all the technical discussions and good time spent together. Fabien Vieuille, from the numerical simulations group, is also acknowledged for the technical assistance related to Actran FEM modelling. I would also like to acknowledge Rüdiger Thomas, Sylvain Miklaszewski, Pierre Lempereur, Klaus Renger, Christophe Ligu and Hugues Rémy for their support, confidence in this work and for the feedback on research documents.

Thanks to all the members of GAUS laboratory for their contribution to this work: Maxime Bolduc, Rémi Oddo and Patrick Levesque are acknowledged for their technical assistance during vibroacoustic tests and research discussions. Celse Kafui Amédin, for providing NOVAFEM results and for helping on topics related to NOVA software. Maxime Bolduc and Vincent Pointel, for providing additional experimental results. Olivier Doutres, for the feedback on compression effect. In addition, I would like to thank Andrée Paradis for all the administrative assistance. Finally, thanks to all the students for the friendly atmosphere and animated discussions.

I am grateful to the Supméca team for the reception and administrative assistance. I am also grateful to the *Laboratoire d'Acoustique de l'Université du Maine* (LAUM) team for the reception in the beginning of the thesis. D. Fonseca and A. Garcia, former students at the *Ecole Nationale Supérieure d'Ingénieurs du Mans* (ENSIM), A. Geslain, former PhD student at LAUM and the *Centre de Transfert de technologie du Mans* (CTTM) team are also acknowledged for the help during experiments related to the compression effect.

Finally, I thank my family and friends for the encouragement and unconditional support.



# TABLE OF CONTENTS

<b>1</b>	<b>INTRODUCTION</b>	<b>1</b>
1.1	Industrial context . . . . .	1
1.2	Objectives . . . . .	2
1.3	Literature review . . . . .	4
1.3.1	Aircraft interior noise: sources and control treatments . . . . .	4
1.3.2	Vibroacoustics of aircraft panels . . . . .	6
1.3.3	Sound transmission through double-walls . . . . .	9
1.3.4	Compression effects on the acoustic performance of porous materials	20
1.3.5	Vibration isolating mounts . . . . .	21
1.4	Summary and methodology . . . . .	26
<b>2</b>	<b>INFLUENCE OF FIBROUS MATERIAL COMPRESSION ON THE SOUND TRANSMISSION OF COVERED PANELS</b>	<b>29</b>
2.1	Chapter introduction . . . . .	29
2.2	Résumé de l'article publié dans le journal Applied Acoustics . . . . .	30
2.3	Paper published on the Applied Acoustics Journal - Introduction . . . . .	32
2.4	Theory . . . . .	33
2.4.1	Modelling sound absorbing materials . . . . .	33
2.4.2	Effects of compression on porous physical parameters . . . . .	35
2.4.3	Sound transmission through multilayer structures . . . . .	37
2.5	Description of the experiment . . . . .	39
2.6	Results and discussion . . . . .	41
2.6.1	Influence of compression on the TL response . . . . .	41
2.6.2	Influence of fibrous properties on the TL . . . . .	42
2.6.3	Influence of compression on the radiation efficiency . . . . .	43
2.7	Conclusion . . . . .	45
2.8	Appendix: Modelling sound absorbing materials (complementary theory) .	46
<b>3</b>	<b>MODELLING OF COUPLING LOSS FACTOR OF AIRCRAFT DOUBLE- WALLS COUPLED VIA VIBRATION ISOLATORS</b>	<b>49</b>
3.1	Chapter introduction . . . . .	49
3.2	Résumé de l'article publié dans le journal NCEJ . . . . .	50
3.3	Paper published on the NCEJ Journal - Introduction . . . . .	51
3.4	Theory . . . . .	52
3.4.1	SEA modelling of a double-wall . . . . .	53
3.4.2	Isolator modelling and structural coupling loss factor determination	54
3.5	Description of the experiments . . . . .	56
3.5.1	Measurement of isolator's dynamic stiffness . . . . .	56
3.5.2	SEA measurements on a double-wall . . . . .	57
3.6	Results and discussion . . . . .	62
3.6.1	Isolator dynamic stiffness . . . . .	62

3.6.2	Results in configuration 1 . . . . .	65
3.6.3	Results in configuration 2 . . . . .	69
3.7	Conclusion . . . . .	74
<b>4</b>	<b>SOUND TRANSMISSION THROUGH UNCOUPLED AIRCRAFT DOUBLE-WALLS</b>	<b>77</b>
4.1	Chapter introduction . . . . .	77
4.2	Résumé de l'article soumis au journal Acta Acustica united with Acustica .	78
4.3	Paper submitted to Acta Acustica United with Acustica Journal - Introduction	79
4.4	Theory . . . . .	80
4.4.1	Transfer matrix method (TMM) . . . . .	80
4.4.2	Statistical energy analysis (SEA) . . . . .	82
4.5	Description of the measurements . . . . .	86
4.5.1	Description of the systems . . . . .	86
4.5.2	Damping loss factor . . . . .	88
4.5.3	Modal density . . . . .	89
4.5.4	Radiation efficiency . . . . .	90
4.5.5	Transmission loss . . . . .	91
4.6	Results and discussion . . . . .	91
4.6.1	Modal density . . . . .	92
4.6.2	Radiation efficiency . . . . .	93
4.6.3	Transmission loss comparisons between TMM, SEA and measurements	95
4.7	Conclusion . . . . .	101
4.8	Supplementary analysis on academic double-walls . . . . .	102
<b>5</b>	<b>SOUND TRANSMISSION THROUGH MECHANICALLY COUPLED AIRCRAFT DOUBLE-WALLS</b>	<b>107</b>
5.1	Chapter introduction . . . . .	107
5.2	Double-wall SEA modelling under acoustic excitation (diffuse field) . . . .	107
5.2.1	Résumé de l'article à être soumis au Journal of the Acoustic society of America . . . . .	108
5.2.2	Paper to be submitted to the Journal of the Acoustical Society of America - Introduction . . . . .	109
5.2.3	Theory . . . . .	111
5.2.4	Description of the experiments . . . . .	117
5.2.5	Results and discussion . . . . .	120
5.2.6	Conclusion . . . . .	129
5.3	Double-wall SEA modelling under structural excitation (uncorrelated point forces) . . . . .	131
<b>6</b>	<b>GENERAL CONCLUSION AND FUTURE WORK</b>	<b>145</b>
<b>A</b>	<b>Principles for double-wall SEA modelling under aerodynamic excitation (turbulent boundary layer)</b>	<b>149</b>
	<b>LIST OF REFERENCES</b>	<b>151</b>

# LIST OF FIGURES

1.1	Representation of the (a) cockpit and (b) cabin components. . . . .	2
1.2	Aircraft sidewall panel components. . . . .	2
1.3	Double-wall transmission model. . . . .	3
1.4	Non dimensional mean-square velocity of the plate excited by a plane wave: <b>————</b> (1) stiffened plate, <b>■ ■ ■ ■</b> unstiffened plate, <b>- - - -</b> orthotropic plate, <b>————</b> (0.1) stiffened plate (ribs with reduced cross-section). From reference [1] . . . . .	9
1.5	Reflection, absorption and transmission of a sound wave in contact with a partition. . . . .	10
1.6	Transmission loss of a typical double-wall, composed of two aluminium pan- els (having equal thickness) and separated by an air gap, subjected to a plane-wave excitation at oblique incidence angle. . . . .	11
1.7	Wavevector spectra for different types of random excitations at $f=1$ kHz and corresponding to the same root-mean-square wall pressure, as a function of the stream-wise wavenumber $k_y$ : <b>————</b> TBL, <b>- - - -</b> DAF, <b>————</b> Spatially random (from reference [2]). . . . .	13
1.8	Transfer matrix representation of a plate lined with a porous layer immersed in air. . . . .	14
1.9	Statistical energy analysis model of a double-wall system with structural connections (from reference [3]). . . . .	16
1.10	Elastomeric panel isolator for aircraft interiors manufactured by <i>LORD cor-          poration</i> . . . . .	22
1.11	Schematic representation of the transmission through an isolator. . . . .	22
1.12	Hysteresis curve for an elastomeric isolator (from ASD-STAN prEN 4662 standard). . . . .	25
2.1	Relative variation of physical parameters as a function of uni-axial com- pression rate of a fibrous layer (base 100 for $n=1$ ): a) airflow resistivity, b) Young's modulus. . . . .	37
2.2	Schematical illustration of the studied structure. . . . .	38
2.3	Experimental set-up: a) Tested structure, b) A-A cut view: 1- Room's wall, 2- Rubber strip, 3- Rigid metallic grid, 4- Fibrous sample, 5- Isotropic plate, 6- Intensimetry probe. . . . .	40
2.4	Responses of the thick plate with glass wool: a) prediction, b) measurement	41
2.5	Influence of a $n=2$ compression of the porous layer on the TL: a) thin plate, b) thick plate. . . . .	42
2.6	Predicted influence of variations in fibrous parameters due to a $n=2$ com- pression on the TL of the system with the thick plate. . . . .	43
2.7	Comparison of the response of the rigid frame, limp and Biot models for the system with the thick plate: a) $n=1.25$ , b) $n=2$ . . . . .	44

2.8	Radiation efficiency of the structure with the thin plate under mechanical excitation. . . . .	44
2.9	Limp porous material wavenumber multiplied by the thickness: a) real part, b) imaginary part. . . . .	45
3.1	Schematic representation of the double-wall system. . . . .	53
3.2	Schematic representation of the isolator. . . . .	55
3.3	Measurement setups: (a) Vertical, (b) Impact hammer, (c) Horizontal, (d) Static. . . . .	59
3.4	Experimental SEA measurements - configuration 1: (a) setup and (b) detail of the connections. 1- plate 1, 2- plate 2, 3- isolator, 4- stud. . . . .	61
3.5	Experimental SEA measurements - configuration 2: (a) setup and (b) detail of the connections. 1- trim panel, 2- stiffened panel, 3- rigid connection element, 4- vertical stiffener. . . . .	61
3.6	Orthogonally stiffened panel: geometrical characteristics and links location. . . . .	62
3.7	Location of isolators ( $\square$ ), accelerometers ( $\circ$ ) and excitation points ( $\times$ ). . . . .	62
3.8	Dynamic stiffness of the isolator. . . . .	63
3.9	Internal damping of the isolator. . . . .	63
3.10	Damping loss factor of the plates (configuration 1). . . . .	66
3.11	Modal densities of the plates. . . . .	66
3.12	Coupling loss factors - rigid coupling (configuration 1). . . . .	67
3.13	Coupling loss factors - soft coupling (configuration 1). . . . .	67
3.14	Vibration transmissibility - rigid configuration, excitation on 3.2 mm plate. . . . .	69
3.15	Vibration transmissibility - Soft configuration, excitation on 3.2 mm plate. . . . .	69
3.16	Damping loss factor of the panels (configuration 2). . . . .	70
3.17	Modal density of the panels. . . . .	70
3.18	Coupling loss factors - rigid coupling (configuration 2). . . . .	72
3.19	Coupling loss factors - soft coupling (configuration 2). . . . .	72
3.20	Vibration transmissibility - rigid configuration, excitation on stiffened panel. . . . .	73
3.21	Vibration transmissibility - Soft configuration, excitation on stiffened panel. . . . .	73
4.1	Double-wall structure: 1-diffuse field excitation, 2-source panel, 3-porous layer, 4-receiving sandwich panel, 5-air gap. . . . .	80
4.2	Transfer matrix representation of the transmission through the studied double-wall system. . . . .	81
4.3	SEA representation of the double wall system. . . . .	84
4.4	Dimension and spacing of the stiffeners: a) aluminium panel, b) composite panel . . . . .	88
4.5	Picture of the measurement setups: (a) damping loss factor, (b) radiation efficiency. . . . .	89
4.6	Modal density of the aluminium panel: comparisons between theory and measurement. . . . .	92
4.7	Modal density of the composite panel: comparison between theory and measurement. . . . .	93

4.8	Modal density of the sandwich panel: comparison between theory and measurement. . . . .	93
4.9	Radiation efficiency of a 3 mm unstiffened aluminium panel: comparison between theory and measurement. . . . .	94
4.10	Radiation efficiency of the sandwich panel: comparison between theory and measurement. . . . .	94
4.11	Transmission Loss of the aluminium panel: comparison between transfer matrix method (TMM), statistical energy analysis (SEA) and measurements for a bare panel and a panel with porous layer. . . . .	96
4.12	Transmission Loss of the composite panel: comparison between transfer matrix method (TMM), statistical energy analysis (SEA) and measurements for a bare panel and a panel with porous layer. . . . .	97
4.13	Difference between the Transmission Loss with and without the porous layer: comparison between transfer matrix method (TMM) and measurement for the composite skin panel. . . . .	97
4.14	Transmission Loss of the sandwich panel: comparison between transfer matrix method (TMM), statistical energy analysis (SEA) and measurement. . . . .	98
4.15	Transmission Loss of the double wall with the orthogonally-stiffened aluminium skin panel: comparison between transfer matrix method (TMM), statistical energy analysis (SEA) and measurement. . . . .	99
4.16	Transmission Loss of the double wall with the vertically-stiffened composite skin panel: comparison between transfer matrix method (TMM), statistical energy analysis (SEA) and measurement. . . . .	100
4.17	Difference between the DWL Transmission Loss with the composite skin panel and the DWL Transmission Loss with the aluminium skin panel: comparison between transfer matrix method (TMM), statistical energy analysis (SEA) and measurement. . . . .	100
4.18	Representation of the three studied configurations. . . . .	102
4.19	Experimental setup for the transmission loss measurement of the double-wall: (a) source side and (b) receiver side. 1-Aluminium panels, 2-heavy bags, 3-plywood, gypsum and glass wool, 4-measurement niche. . . . .	103
4.20	Transmission loss of the double-wall composed of a 2 mm aluminium panel, 3.5 in. of air gap and 1 mm aluminium panel. . . . .	104
4.21	Transmission loss of the double-wall composed of a 2 mm aluminium panel, 2 in. of melamine foam, 1.5 in. of air gap and 1 mm aluminium panel. . . . .	105
4.22	Transmission loss of the double-wall composed of a 2 mm aluminium panel, 3 in. of glass wool (0.6 pcf), 0.5 in. air gap and 1 mm aluminium panel. . . . .	105
5.1	Representation of the double-wall structure: a) aluminium skin panel, b) composite skin panel. 1-diffuse field excitation, 2-skin panel, 3-porous layer, 4-trim panel, 5-vibration isolator, 6-stiffener. . . . .	110
5.2	SEA representation of the double-wall system. . . . .	111
5.3	Sound transmission paths of the double-wall SEA system. 1-Source cavity, 2- skin panel, 3-inner cavity, 4-trim panel, 5-receiver cavity. . . . .	112
5.4	Composite stiffened panel: dimensions and links location. . . . .	119

5.5	Aluminium stiffened panel: dimensions and links location. . . . .	119
5.6	Transmission loss through the double-wall with the aluminium skin panel in a structurally decoupling configuration: — SEA and ···· measurements. . . . .	121
5.7	Transmission loss through the double-wall with the aluminium skin panel in a rigid coupling configuration: — SEA (dynamic stiffeners), - · SEA (rigid stiffeners) and ···· measurements. . . . .	122
5.8	Transmission loss through the double-wall with the aluminium skin panel in a coupling via isolators configuration: — SEA (dynamic stiffeners), - · SEA (rigid stiffeners) and ···· measurements. . . . .	123
5.9	Theoretical and measured delta transmission loss of uncoupled or soft-coupled (via isolators) compared to a rigid-coupling configuration. Aluminium skin panel case. —▲ Uncoupled - Rigid: SEA, —× Soft - Rigid: SEA, ···· Uncoupled - Rigid: tests, ···· Soft - Rigid: tests. . . . .	123
5.10	Theoretical and measured delta transmission loss of uncoupled or soft-coupled (via isolators) compared to a rigid-coupling configuration. Composite skin panel case. —▲ Uncoupled - Rigid: SEA, —× Soft - Rigid: SEA, ···· Uncoupled - Rigid: tests, ···· Soft - Rigid: tests. . . . .	124
5.11	Theoretical transmission loss contributions of each transmission path: aluminium skin, uncoupled configuration. — double-wall non-resonant transmission, ···· trim non-resonant transmission, — trim airborne radiation, — total. . . . .	126
5.12	Theoretical transmission loss contributions of each transmission path: aluminium skin, rigid coupling configuration. — double-wall non-resonant transmission, ···· trim non-resonant transmission, — trim airborne radiation, - · trim structure-borne radiation, — total. . . . .	126
5.13	Theoretical transmission loss contributions of each transmission path: aluminium skin, coupling via isolators configuration. — double-wall non-resonant transmission, ···· trim non-resonant transmission, — trim airborne radiation, - · trim structure-borne radiation, — total. . . . .	127
5.14	Theoretical transmission loss contributions of each transmission path: composite skin, uncoupled configuration. — double-wall non-resonant transmission, ···· trim non-resonant transmission, — trim airborne radiation, — total. . . . .	128
5.15	Theoretical transmission loss contributions of each transmission path: composite skin, rigid coupling configuration. — double-wall non-resonant transmission, ···· trim non-resonant transmission, — trim airborne radiation, - · trim structure-borne radiation, — total. . . . .	128
5.16	Theoretical transmission loss contributions of each transmission path: composite skin, coupling via isolators configuration. — double-wall non-resonant transmission, ···· trim non-resonant transmission, — trim airborne radiation, - · trim structure-borne radiation, — total. . . . .	129
5.17	SEA representation of the double-wall system under structural excitation. . . . .	131
5.18	Sound transmission paths of the double-wall SEA system. 2-skin panel, 3-inner cavity, 4-trim panel. . . . .	133

5.19	Vibration transmissibility of the double-wall composed of a 2 mm unstiffened panel, 2 in. of glass wool, 2 in. of air gap and a 3 mm aluminium panel: comparisons between FEM, TMM and SEA. . . . .	135
5.20	AMCE of the double-wall composed of a 2 mm unstiffened panel, 2 in. of glass wool, 2 in. of air gap and a 3 mm aluminium panel: comparisons between FEM, TMM and SEA. . . . .	135
5.21	Transfer path analysis of the double-wall composed of a 2 mm unstiffened panel, 2 in. of glass wool, 2 in. of air gap and a 3 mm aluminium panel, using the SEA model. . . . .	136
5.22	FEM representation of the double-wall system with the orthogonally stiffened aluminium panel. . . . .	138
5.23	FEM representation of the double-wall system with the uni-directionally stiffened laminate composite panel. . . . .	139
5.24	Vibration transmissibility of the uncoupled double-wall composed of the 2 mm stiffened aluminium panel, 2 in. of glass wool, 2 in. of air gap and the sandwich trim panel: comparisons between FEM, TMM, SEA and tests.	139
5.25	AMCE of the double-wall composed of the 2 mm stiffened aluminium panel, 2 in. of glass wool, 2 in. of air gap and the sandwich trim panel: comparisons between FEM, TMM, SEA and tests. Uncoupled configuration. . . . .	140
5.26	Transfer path analysis of the double-wall composed of the 2 mm stiffened aluminium panel, 2 in. of glass wool, 2 in. of air gap and the sandwich trim panel: uncoupled configuration. . . . .	140
5.27	AMCE of the double-wall composed of the 2 mm stiffened aluminium panel, 2 in. of glass wool, 2 in. of air gap and the sandwich trim panel: comparisons between FEM, SEA and tests. Rigid coupling configuration. . . . .	141
5.28	Transfer path analysis of the double-wall composed of the 2 mm stiffened aluminium panel, 2 in. of glass wool, 2 in. of air gap and the sandwich trim panel: rigid coupling configuration. . . . .	141
5.29	AMCE of the double-wall composed of the 2 mm stiffened aluminium panel, 2 in. of glass wool, 2 in. of air gap and the sandwich trim panel: comparisons between FEM, SEA and tests. Coupling via isolators configuration. . . . .	142
5.30	Transfer path analysis of the double-wall composed of the 2 mm stiffened aluminium panel, 2 in. of glass wool, 2 in. of air gap and the sandwich trim panel: comparisons between FEM, SEA and tests. Coupling via isolators configuration. . . . .	142
5.31	Influence of mechanical links on the AMCE of the double-wall composed of the 2 mm stiffened aluminium panel, 2 in. of glass wool, 2 in. of air gap and the sandwich trim panel: comparisons between SEA and tests. . . . .	143
5.32	Influence of mechanical links on the AMCE of the double-wall composed of the 2.75 mm stiffened laminate panel, 2 in. of glass wool, 2 in. of air gap and the sandwich trim panel: comparisons between SEA and tests. . . . .	143



# LIST OF TABLES

1.1	Transfer functions, (a) transfer and (b) input dynamic stiffness and damping loss factor calculated for a displacement $x_2 = 0$ . . . . .	24
2.1	Porous material properties measured for each compression rate, $n=1$ , $n=1.25$ and $n=2$ . . . . .	40
4.1	Source panels properties . . . . .	87
4.2	Receiving sandwich panel properties . . . . .	87
4.3	Porous material properties . . . . .	87
4.4	Single and double-walls tested configurations . . . . .	88
4.5	Melamine foam properties . . . . .	103
5.1	Energy ratio between source and receiver cavity for each transmission path.	116
5.2	Skin panels properties. . . . .	118
5.3	Porous material properties. . . . .	118
5.4	Receiving sandwich panel properties. . . . .	119



# LIST OF ACRONYMS

AMCE	Acoustic / mechanical conversion efficiency
BEM	Boundary element method
CFRP	Carbon fibre reinforced plastic
CLF	Coupling loss factor
DAF	Diffuse acoustic field
DLF	Damping loss factor
DRM	Decay rate method
DWL	Double-wall layer
ECS	Environmental Control System
FEM	Finite element method
FTMM	Finite Transfer matrix method
GAUS	Groupe d'Acoustique de l'Université de Sherbrooke
JASA	Journal of the Acoustical Society of America
LISMMA	Laboratoire d'Ingénierie des Systèmes Mécaniques et des Matériaux
NCEJ	Noise Control Engineering Journal
NR	Noise reduction
PIM	Power input method
SEA	Statistical energy analysis
SIL	Speech interference level
TBL	Turbulent boundary layer
TL	Transmission loss
TMM	Transfer matrix method
TPA	Transfer path analysis
UPMC	Université Pierre and Marie Curie



# CHAPTER 1

## INTRODUCTION

This chapter starts with the description of the industrial context of this research. The main objectives of the study are defined and a literature review is performed on essential topics. Next, the state-of-the-art on the subject is summarized and the steps of the research methodology are outlined. Finally, the structure of the report is presented.

### 1.1 Industrial context

The cockpit and cabin acoustic comfort is an important design driver for modern air transport aircraft. Besides, a low level of noise helps improving the work environment of the Crew (intelligibility, work load). Consequently, Airbus aims at further improving aircraft noise levels beyond the state of the art and therefore is promoting research activities that could enable an even quieter design in this area for future products.

In the context of turbo-jet aircraft, the multi-source broadband noise is directly linked to communication intelligibility and acoustic comfort. The overall noise is composed of mainly (1) the turbulent boundary layer (TBL), (2) the avionics system and other systems (hydraulic, electrical, etc), (3) the environmental control system (ECS), consisting of the thermo and the air conditioning systems, and (4) the engine noise. Basically, the turbulent boundary layer is the dominant source of cockpit and front cabin interior noise during flight at frequencies higher than 300 Hz. At the rear part of the cabin, jet noise is also important [4].

The cockpit and cabin structures are mainly composed of an assembly of multilayer glass windows, cabin doors and curved stiffened panels (Fig. 1.1). These metallic or composite panels are lined with a thermal and acoustic insulation layer and a commercial lining. They are an important transmission path of airborne and structure-borne noise. The reduction of aircraft noise level is linked to the improvement of the acoustical properties of the assembly composed of the fuselage skin, the insulation layer, the commercial lining and different structural links, as shown in figure 1.2.

In order to cover the extended frequency range of the problem (40 Hz - 12500 Hz), models based on analytical methods, finite elements (FEM/BEM) and statistical energy analysis

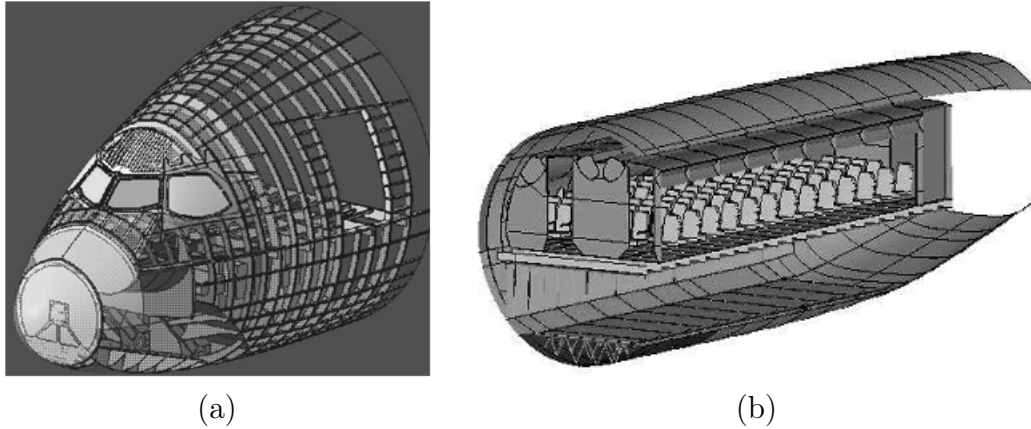


Figure 1.1 Representation of the (a) cockpit and (b) cabin components.

(SEA) are widely employed. These models are validated with experiments having three degrees of complexity: (i) academic structures (cylinders, plates), (ii) aircraft sections under acoustic excitation and (iii) in-flight tests. The characterisation of the transmission properties of the materials on one side and the excitation field on the other side constitute a key point to ensure the prediction aspect of such tools.

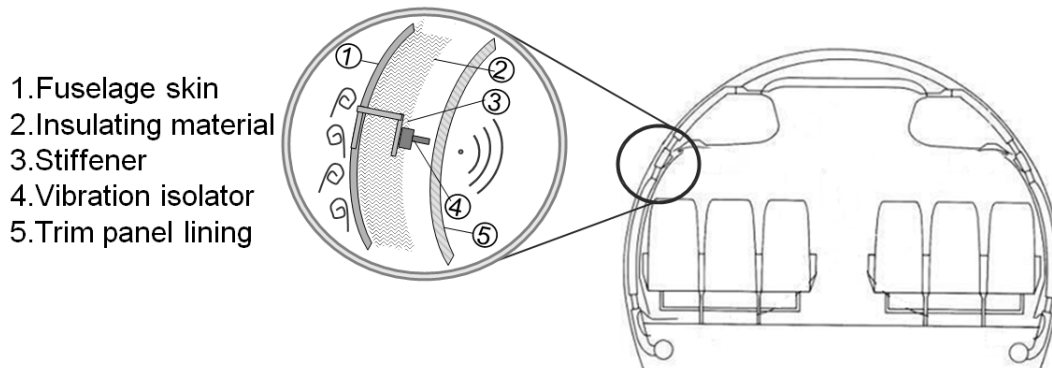


Figure 1.2 Aircraft sidewall panel components.

## 1.2 Objectives

The proposed work is included in the topic of noise reduction and has as main objective the development of an optimised configuration of the fuselage, connections, sound insulation and commercial lining ensemble, accounting for the compromise between acoustical performance and weight of the treatment. The developed vibroacoustic model should be a fast and accurate tool to be used at the conception stage of an aircraft project, considering the industrial context. Particular attention will be paid to installation effects on the porous layer (compression), noise transmission through structural mounts linking

the panels, and transmission mechanisms linked to different excitation fields (acoustic and structural).

The vibroacoustic modelling strategy is summarized in Fig. 1.3. It consists of developing a double-wall model for flat structures, including structural transmission between panels via vibration isolators. The thermo-phonic insulation is taken into account using existing models such as equivalent fluid or Biot. Effects of compression of the porous layer on the sound transmission are also analysed. Extensive tests are to be performed on single and double-walls including isotropic, orthotropic and sandwich composite materials. The acoustic indicators analysed are the sound transmission and insertion loss. Theoretical results are then to be compared to tests in order to identify the limits of the model. Finally, as a basis to understand the sound transmission under in-flight turbulent boundary layer excitation, an analysis of the transmission mechanisms under acoustic and mechanical excitations is to be performed.

From the industrial perspective, the model should be able to predict the influence in the sound transmission caused by modifications of parameters of the double-wall, compared to a given baseline configuration. In addition, it should predict the contribution of each transmission path (airborne and structure-borne paths) to the total sound transmission through the double-wall in order to identify adapted noise control treatments.

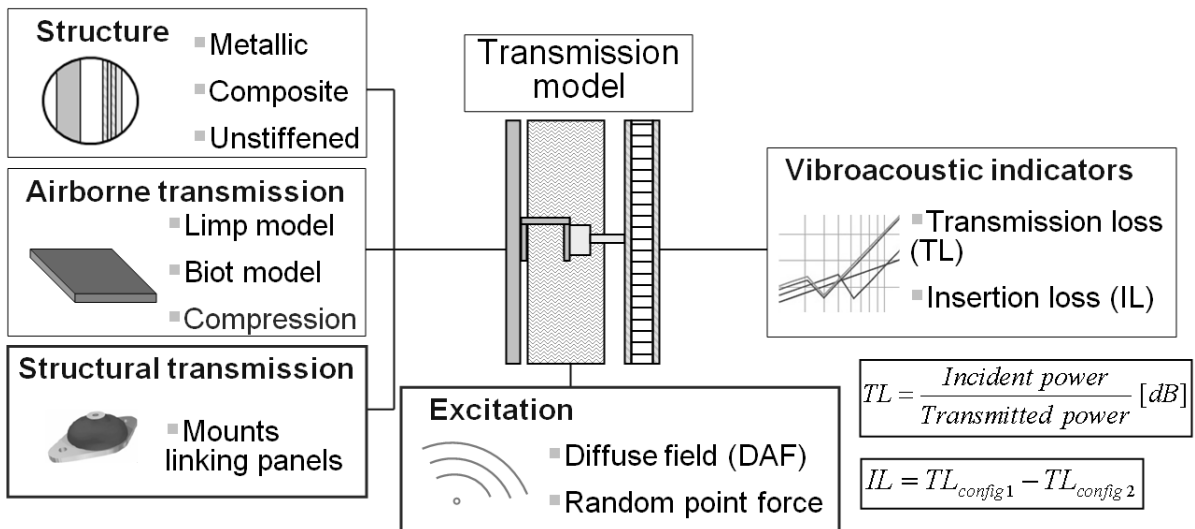


Figure 1.3 Double-wall transmission model.

## 1.3 Literature review

This section summarizes the state-of-the-art on the main subjects related to this research. It starts with a description of the aircraft interior noise. Then, the main phenomena on the vibroacoustic of aircraft panels are outlined. Different approaches to compute the sound transmission through double-walls are discussed. Finally, a literature review is performed on the effect of compression of porous materials as well as on vibration isolating mounts.

### 1.3.1 Aircraft interior noise: sources and control treatments

The main acoustic indicators used by Airbus and airlines are: (1) "Speech interference level" (SIL), computed from the average of acoustic pressure levels in the octaves of 1, 2 and 4 kHz, (2) overall sum of pressure levels between 44 Hz and 11.3 kHz in dB(A).

Several means of decreasing aircraft interior noise can be enumerated. They are an important subject from the pre-design phase of conception, passing to the understanding of the different sources, to the solutions for an already existent aircraft. They are mainly described as passive and active or semi-active treatments. Examples of passive treatments are porous materials [5] and damping treatments [6]. Active treatments are represented by noise cancelling techniques and smart-foams [7–9]. The work by Wilby [10] and Kuznetsov [11] summarize means employed in the reduction of aircraft interior noise since the late 1950's and the noise control problems of passenger aircraft. As a compromise between acoustical performance and weight should be kept, optimisation of sound treatment has gained a lot of importance in parallel to reduction of noise at the source itself [10].

*Turbulent boundary layer:* The generation of noise by the TBL became an important topic since the advent of turbo-jet aircraft. It was then demonstrated that this type of noise contributed significantly to the increase of mid- and high frequency sound pressure in the cabin (above 300 Hz). Because the noise generated by turbulent airflow over the surfaces of high-speed aircraft is a major source of annoyance during cruise, there is an important economic interest in reducing the transmission of TBL noise within the aircraft. This problem has to be addressed at the design stage and requires a simple model, in order to save computational effort while providing the best physical insight [12]. Some advances in defining the pressure field, the auto- and cross-spectra and coherence functions were due to the work of Corcos [13], Willmarth [14, 15], and Bull [16]. It is known that the pressure fluctuations involve a wide range of frequencies and are dominated by wavenumber components centred around the convective wavenumber of the flow. Recent investigations make use of the wavenumber-frequency representation of the spectrum [2] but the selection

of the most adapted turbulent layer pressure field representation is still up to debate. The integration of TBL in sound transmission models is important since the transmission mechanisms are different compared to an acoustical excitation [17].

*Jet noise:* Jet noise remains an important source of noise during cruise at the rear part of the cabin. The influence of jet noise on the fuselage vibration increases as the engine is installed closer to the cabin. The separation of jet and TBL noise is often difficult since both are broadband. However, some differences are noticeable as the vibration of the fuselage induced by jet noise is highly correlated over several panels both in the longitudinal and circumferential directions, which is not the case for the TBL, especially in the circumferential direction [18]. The typical values of fuselage critical frequencies are between 6 kHz - 12 kHz, and 400 Hz for the ring frequency. Jet noise transmission through metallic fuselage lies below the critical frequency but includes the ring frequency, meaning it is controlled mainly by non-resonant modes. Moreover, the pressure mismatch of the outflow pressure at the engine nozzle exit with respect to ambient air leads to the formation of a series of compression and expansions in the jet plume, called shock-cell. The interaction between the turbulence in the mixing layers and the compression/expansions generates an additional component of the jet noise, the shock-cell noise [19].

*Structure-borne noise:* Represented by the vibrations originated at the engine or by a high-level acoustic source inducing vibrations. It is associated with the resonant response of the fuselage structure. The importance of this type of noise has been recognised in the past and first preventions made use of rubber supports between engine and nacelle connections showing the importance of vibration isolation in engine mounts [20]. It has also been indicated that fuel in the wing provides substantial attenuation. Direct measurement of structure-borne noise requires measurement of the power flow of flexural, longitudinal and torsional waves.

Wilby [10] points out that almost all aircraft make use of only passive methods to control interior noise. The general concept, remained constant over the years, comprises a fibrous material layer with a density of about  $10 \text{ kg.m}^{-3}$ , a trim panel attached to the fuselage at the frames usually by means of isolating mounts. The emphasis is put in the compromise between weight and an adequate sound level. Constrained layer damping, effective at cruise flight temperatures, is sometimes applied to the fuselage skin. Helmholtz resonators and dynamic absorbers are also used in an attempt to attenuate discrete frequency components mainly caused by noise coming from the propeller or engine's fundamental tone. Despite the fact that the last decades showed numerous investigations on active noise control,

its current commercial implementations are mainly directed to the control of discrete frequency components, mainly in propeller-driven aircraft.

### 1.3.2 Vibroacoustics of aircraft panels

Thin stiffened panels are widely used in the aeronautic industry in order to account for reinforcement (bending rigidity) and stability and at the same time remaining light. The understanding of the behaviour and modelling of such structures are an open point, specially under TBL excitation. The present work deals only with the modelling of unstiffened panels but the knowledge of the vibroacoustic behaviour of stiffened panels and a comparison with unstiffened panels is important in order to understand the limitations of the proposed modelling.

The problem of modelling the dynamic behaviour of metallic stiffened structures was first solved by modelling an equivalent orthotropic structure [21]. This means that the propagation of plane bending waves occurs with different velocities for different directions. The Kirchhoff's thin-plate hypothesis and Euler-Bernoulli theory were applied at a first stage, giving place to Reissner-Mindlin approach for thin plates and Timoshenko theory for beams. Such approaches are valid at low frequencies where the wavelength of bending waves is larger compared to the spacing between the stiffeners. Heckl [22] suggested that a periodic ribbed plate could be treated as an orthotropic plate when the distance between the adjacent ribs is less than a quarter of the shortest plate-bending wavelength.

In the context of Statistical Energy Analysis, Bremmer [23] has explained the distinct behaviours in terms of the wavenumbers of a flat ribbed plate of width  $L_x$  and height  $L_y$  stiffened bidirectionally with stiffeners spaced by  $S_x$  and  $S_y$  in each direction. As the modal half-wavelength in the x and y direction goes below the  $S_x$  or  $S_y$  dimensions, the plate behaviour shifts from global, over the plate area, to periodic, over areas limited by  $L_x$ ,  $S_y$  and  $S_x$ ,  $L_y$ . Finally, when the modal half-wavelength goes below the stiffeners spacing, the modal behaviour is determined by the behaviour of a flat uniform subpanel delimited by the stiffeners. Those are the zones to take into account when modelling the modal behaviour of a stiffened plate over a large frequency band.

It is worth noting that while there is an extensive literature on the response of isotropic flat plates to TBL excitation, e.g. [24, 25], only a few published studies are available on the vibroacoustic response of stiffened panels under TBL excitation [26–28].

More recently, composite panels were introduced in aerospace because of their high strength characteristics and low weight compared to the equivalent metallic structures. One of the

most common form of composite materials is the crossplied laminated, in which a sequence of unidirectionally reinforced plies is layed up to form the material. Each ply is typically a thin sheet of collimated fibres impregnated with an uncured epoxy resin. The orientation of each ply is arbitrary, and the layup sequence is tailored to achieve the properties desired of the laminate. Laminated plates are usually modelled as a two-dimensional problem so the thin isotropic plate theories can be extended to the laminated plate theories, which are based either on the Kirchhoff hypothesis or on the shear deformation assumptions.

A wave-approach based numerical method is proposed in [29] to solve the relation of dispersion of flat laminated composite panels. The dispersion relation is written in the form of a polynomial generalised complex eigenvalues problem. The results are used to calculate the group velocity, the modal density and the radiation efficiency. These indicators are used in the statistical energy analysis framework to estimate the sound transmission of the laminate composite structures. The model proposed in [30], accounting for orthotropy, uses a discrete displacement field formulation and allows for out of plane displacements and shearing rotations. Each discrete layer is considered laminated (composite) but the physical properties are smeared through the thickness of each layer so that the problem's dimension remains unchanged. More recently, a semi-analytical method based on modal expansion technique is proposed in [31] to predict the vibration and acoustic radiation of both metallic and composite flat panels stiffened with uni- and bidirectional eccentric stiffeners. The response to point force, diffuse acoustic field and turbulent boundary layer are analysed.

Together with laminate composites, sandwich structured composite materials are also largely used in the aeronautic industry, notably for the fabrication of the commercial lining and the floor. They are usually made of thin face sheets and a shearing core, which is generally made up of a softer material than the skins. The vibroacoustic modelling of sandwich panels is investigated in a large number of papers. A review of the different modelling approaches is presented in [30, 32]. Models in references [30, 32, 33] allow for the prediction of the sound transmission through: (i) infinite laminate and sandwich composite panels [30, 33] and (ii) cylindrical shells [32] under DAF. The first is limited to symmetrically laminate composite shells and the second is more general and is based on a discrete layer theory. For each model, membrane, bending, transverse shearing as well as rotational inertia effects and orthotropic ply angle of the layers are considered. They were extensively validated numerically and experimentally. Its main limitation, as the majority of classical sandwich models, is its inability of representing symmetric motions of the sandwich panels.

Maidanik [34], evaluating the response of a stiffened plate excited by a diffuse field, found that the stiffeners increase the radiation resistance of the panel. In addition, Fahy [35] states that the stiffeners deteriorate the sound transmission loss (TL) of the panel, defined in section 1.3.3, because the wave reflections produced by the stiffeners have wavenumber components of supersonic phase velocity that may propagate at frequencies below the uniform plate critical frequency, increasing thus the sub-critical radiation efficiency. Guigou-Carter [36], using a wave approach to calculate the diffuse field TL of a periodically stiffened aluminium plate, showed that the stiffeners have limited effect in the low frequency range and deteriorate the TL in the mid frequency range (below the critical frequency). The author also states that the stiffeners slightly lower the critical frequency and have a damping effect broadening the critical frequency gap. Similar results are obtained in [37] for the noise reduction (NR) of unstiffened and stiffened plates (refer to [37, 38] for the definition of the NR indicator). Finally, the effect of stiffeners under diffuse field and turbulent boundary layer is analysed on the transmission loss of a plate [39]. For both excitations, the stiffeners decrease the transmission loss compared to unstiffened structures. It is also found out that stiffeners have almost no effect in the aerodynamic coincidence region.

Koval [40] concluded that while the curvature increases the transmission loss of a structure at low frequencies creating a minimum at the ring frequency, the pressurisation decreases the TL, slightly increases the ring frequency and decreases the critical frequency. For frequencies higher than the ring frequency (approximately above twice the ring frequency), curved panels present the same behaviour as flat plates. In a second paper [41], Koval concluded that stiffeners increase the transmission of a cylindrical structure for frequencies higher than the ring frequency while they do not modify the TL at lower frequencies. In addition, in-plane stresses caused by the cabin pressurisation and acting on the boundaries of the panel lead to an increase of the fundamental resonance frequency of the panel by a factor of about 3 [12].

A recent study [42] treats of the determination of two important statistical energy analysis (SEA) parameters, the modal density and the radiation efficiency of a longitudinally stiffened cylindrical shell. It is shown that the presence of longitudinal stiffeners do not change the value of the ring frequency, and that the maximum of the modal density is of the same order for unstiffened and stiffened shells and occurs at the ring frequency. However, above the ring frequency the modal density of stiffened shells is higher than that of unstiffened shells because same order modes have lower frequencies when the cylinder is

stiffened and the difference in the modal frequencies between the stiffened and unstiffened cylinders increases as the frequency increases.

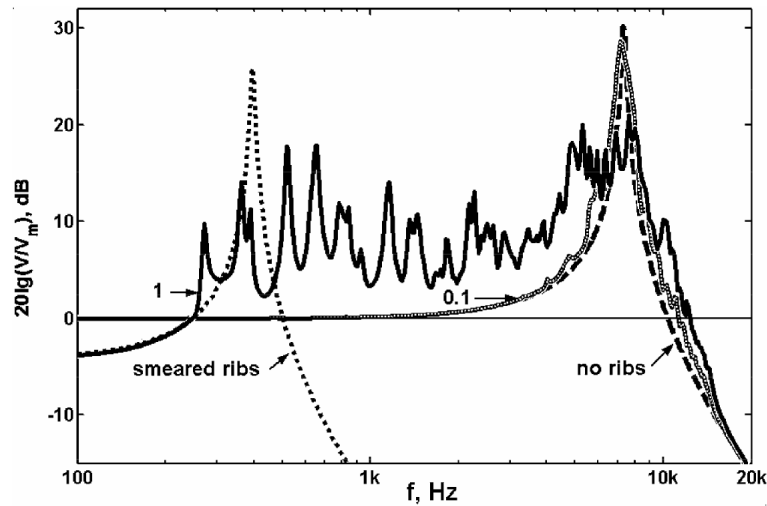


Figure 1.4 Non dimensional mean-square velocity of the plate excited by a plane wave: **—** (1) stiffened plate, **- - -** unstiffened plate, **· · · ·** orthotropic plate, **—** (0.1) stiffened plate (ribs with reduced cross-section). From reference [1]

Efimtov et al. [1], using a space-harmonic modelling for the vibration of an orthogonally stiffened plate that allows three displacement components and rotation, compares (figure 1.4) the responses of a stiffened plate (solid line 1), an unstiffened plate (dash line) and an orthotropic plate with smeared ribs (dotted line), excited by a plane wave. Figure 1.4 shows the mean-square velocity of the plate normalised by  $V_m$  at purely inertial behaviour of the unstiffened plate (the plate is treated as an equivalent mass). The single maximum for isotropic or orthotropic plate models are due to the coincidence of the acoustic wavenumber and the plate eigen-wavenumber. At low frequencies the stiffened plate behaves like the orthotropic one while at high frequencies it behaves like the unstiffened one. The plate with discrete ribs manifests its highly resonance excitation at other frequencies due to the interaction of a large number of vibration shapes. The stiffened plate response approaches that of an unstiffened one when the stiffeners become smaller (solid line 0.1 refers to ribs with 10 times diminished cross-section).

### 1.3.3 Sound transmission through double-walls

When a sound wave strikes a partition, some portion of its energy is reflected, another portion is absorbed and the remaining portion is transmitted through (see figure 1.5). The amounts of reflection, absorption and transmission depend upon the properties of the

partition. A partition can be any panel or any combination of panels or panels with sound packages. A sound package may be sound absorbent materials, or material attachments to panels for stiffening, absorption and/or damping purposes. There is hence a vast variety of partitions that are available and one single theory cannot adequately describe the sound transmission characteristics. Aircraft fuselage, trim panel, noise treatment materials in between the fuselage and trim panel, structural links and windows all make up the partition that separates the interior of the aircraft from the outside.

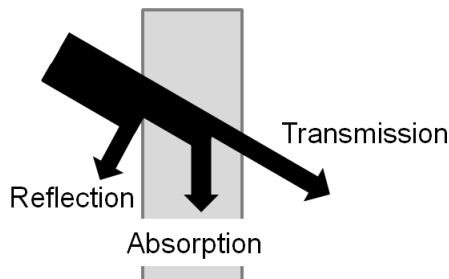


Figure 1.5 Reflection, absorption and transmission of a sound wave in contact with a partition.

One acoustic indicator employed to quantify the transmission through such structures is the Transmission loss [35, 43–45], defined as the logarithm ratio between incident,  $W_I$  and transmitted  $W_T$  powers,  $\tau = \frac{W_T}{W_I}$ :

$$TL = 10 \log_{10} \left( \frac{1}{\tau} \right).$$

Under DAF field excitation, the incident power is  $W_I = \frac{\langle p_{rev}^2 \rangle A_1}{4\rho_0 c_0}$ . Here,  $\langle p_{rev}^2 \rangle$  is the mean squared pressure in the reverberant room,  $A_1$  is the area of the panel,  $\rho_0$  and  $c_0$  are the density and the speed of the sound.

The diffuse field transmission loss of an infinite panel is obtained by averaging the transmission coefficient  $\tau$  over all incidence angles ( $\theta$ ).

A typical transmission loss curve is shown in figure 1.6 for a double-wall immersed in air, composed of two aluminium panels (having equal thickness) and separated by an air gap, subjected to a plane-wave excitation at oblique incidence angle.

Zone 1 corresponds to the response of an equivalent single-wall having the mass per unit surface of the double-wall up to the decoupling frequency in zone 2, given by:

$$f_D = \frac{1}{2\pi \cos(\theta)} \sqrt{\frac{\rho_0 c_0^2 (m_1 + m_2)}{h m_1 m_2}}, \quad (1.1)$$

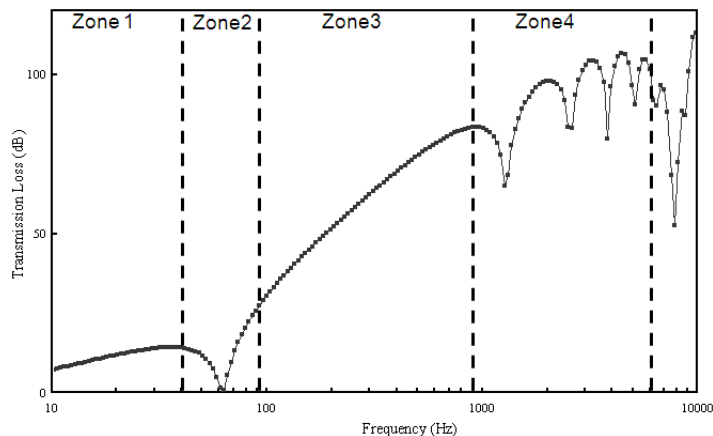


Figure 1.6 Transmission loss of a typical double-wall, composed of two aluminium panels (having equal thickness) and separated by an air gap, subjected to a plane-wave excitation at oblique incidence angle.

where,  $\rho_0$ ,  $c_0$ ,  $m_1$ ,  $m_2$  and  $h$  denote the density of the fluid, the speed of sound in the fluid, the mass of panels 1 and 2 and the distance separating the panels, respectively. There is a significant reduction in transmission loss at the double-wall panel resonance. The addition of damping within the cavity results in an improvement of the TL at  $f_D$ . In addition, an increase of the incidence angle leads to a increase of  $f_D$ , while the addition of porous inside the cavity leads to a decrease of this frequency.

Then, in zone 3 the TL increases at a rate of 18 dB per octave (after the double-wall panel resonance). This increase is maintained until the first air-gap resonance appears (in zone 4). These air-gap resonances can be minimised and significant improvements can be achieved in the transmission loss by the inclusion of sound absorbing material within the cavity between panels. In zone 4, the transmission loss increases at a rate of 12 dB per octave up to the coincidence frequency of the panels. Under diffuse acoustic field, due to the average over the incidence angle, only the lowest coincidence frequency remains and it is called critical frequency. For an isotropic plate, it is given by:

$$f_c = \frac{c_0^2}{2\pi h} \sqrt{\frac{12\rho_s(1-\nu^2)}{E}} \quad (1.2)$$

where  $h$ ,  $\rho_s$ ,  $\nu$  and  $E$  are respectively, the thickness, the density, the Poisson ratio and the Young's modulus of the panel.

The present thesis deals mainly with the response of structures under acoustic and structural excitation but the understanding of transmission mechanisms under aerodynamic excitation is important in order to consider trends for in-flight applications.

Under TBL excitation another coincidence dip appears in the transmission curve at the aerodynamic coincidence frequency when the velocity of bending waves matches the convective flow velocity  $U_c$ . This frequency is given by equation 1.3 and is, for an aircraft, around 1000 Hz depending on flight conditions.

$$f_{c,aero} = \frac{U_c^2}{2\pi h} \sqrt{\frac{12\rho_s(1-\nu^2)}{E}} \quad (1.3)$$

For a DAF, a large proportion of non-resonant modes and resonant modes are efficiently excited over a broad frequency range below the acoustic coincidence frequency. A similar situation occurs for the TBL only below the aerodynamic coincidence frequency. For a given mean-square pressure level, the levels for the vibrating response of a panel excited by a DAF are higher than those observed for a TBL in the low-frequency domain. It implies that modes that contribute to the panel response under DAF are more efficiently excited and have a better coupling than in the case of a TBL excitation. For the latter, the panel modes are uncorrelated, the cross modal excitation terms are negligible with respect to the diagonal terms, and the sound power radiated by the panel is obtained from the sum of the sound power radiated by each structural mode [2, 12].

A recent work [2] compares the diffuse acoustic field (DAF), the turbulent boundary layer and a spatially random field (rain-on-the-roof) excitation using a wavenumber-frequency approach. The wavenumber spectra of each excitation field associated with the same mean-square wall pressure are plotted in figure 1.7 at a fixed-frequency  $f=1$  kHz, in the stream-wise direction ( $y$ ) for a finite aluminium plate at Mach=0.77 (using Corcos model for the TBL [46]). For the DAF, the energy content is limited to the wavenumber range  $[-\frac{\omega}{c_0}, \frac{\omega}{c_0}]$ , where  $\omega$  is the radian frequency and  $c_0$  the sound velocity in the air. For the TBL excitation the main energy fluctuations in the wavenumber spectrum are concentrated around the convecting scales of the flow, i.e., near the convective ridge ( $k_x \sim 0, k_y \sim \frac{\omega}{U_c}$ ), where  $k_x, k_y$  and  $U_c$  are the wavenumber in the x and y directions and the convective flow velocity, respectively. The levels for the rain on the roof excitation are low compared to the others since it is uniformly distributed over the entire wavenumber-frequency range.

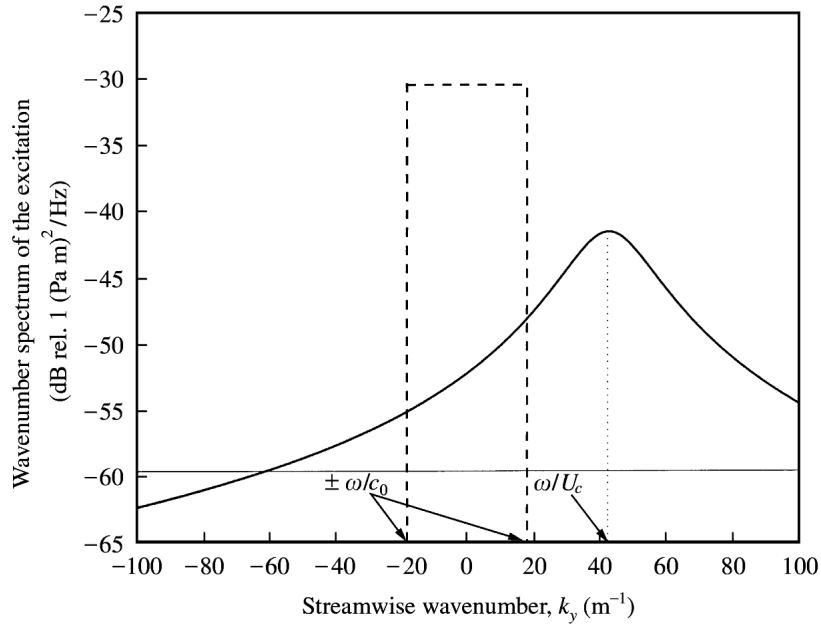


Figure 1.7 Wavevector spectra for different types of random excitations at  $f=1$  kHz and corresponding to the same root-mean-square wall pressure, as a function of the stream-wise wavenumber  $k_y$ : **—** TBL, **- - -** DAF, **—** Spatially random (from reference [2]).

In the case of the figure it is limited in the wavenumber domain to a bandwidth of  $500 \text{ m}^{-1}$ .

### Transfer Matrix Method (TMM)

Sound propagation of plane waves in layers of stratified media can be modelled using transfer matrices [5, 47]. The media can be of different nature: elastic solid, thin plate, fluid, rigid porous, limp porous and poroelastic. Each layer is represented by a vector  $V$  composed of velocities and stresses (solids, porous) or pressure (fluids) caused by the propagating wave.

Figure 1.8 shows a system composed of a solid layer (aluminium plate) and a porous layer immersed in air. The incident and reflected wave at side (i), the solid (1) and the porous (2) layers, and the transmitted wave at side (o) are represented. Each layer is considered of infinite lateral dimensions. The propagation through M1-M2 is given by  $V(M1) = [T]V(M2)$ , where  $T$  is the transfer matrix of the layer and depends on the thickness and the physical properties of each medium. Boundary conditions at interfaces A-M1, M2-M3, M4-B are the continuity of velocities and stresses/pressures.

The transfer matrix method can be generalised to account for other domains such as thick plates, orthotropic plates, composite and sandwich panels, transversely isotropic porous

materials [5]. Different excitation fields can be modelled, e. g. plane waves, point-forces, monopoles and imposed velocities. The generalisation to curved sound packages and the integration of the turbulent boundary layer excitation, both important in the context of aircraft applications, are still an open issue.

Typical acoustic indicators obtained with this method are the surface impedance, reflection, absorption and transmission coefficients, the air-borne and structure-borne transmission loss. The classical TMM assumes a structure of infinite lateral dimensions. Such assumption can generate discrepancies at low frequencies, specially for small-size panels. However, results can also be corrected to account for the finite dimensions of structures [5, 48, 49].

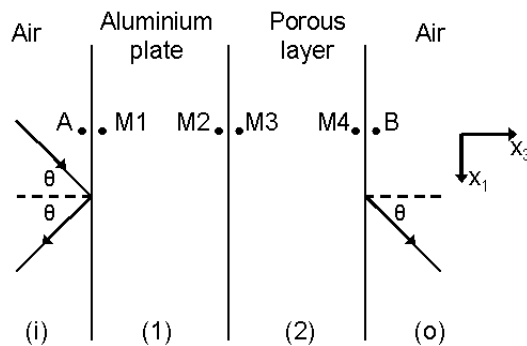


Figure 1.8 Transfer matrix representation of a plate lined with a porous layer immersed in air.

Vigran [50] integrates the structure-borne transmission in the transfer matrix method using a technique derived from the semi-empirical model put forward by Sharp [51]. The links are modelled as rigid mass-less connections. The model is then extended to account for resilient elements by introducing a spring with a frequency-dependent translational stiffness [52]. The modelling relies on the determination of the radiation efficiency for point- and line-driven plates. The diffuse field sound transmission index of a double-wall partition after Sharp is then composed of two independent contributions (airborne and structure-borne). It is given by:

$$TL = 10 \log \left( \frac{\Pi_i}{\Pi_{2,P} + \Pi_{2,B}} \right) = TL_p - 10 \log \left( 1 + \frac{\Pi_{2,B}}{\Pi_{2,P}} \right), \quad (1.4)$$

where  $\Pi_i$  is the incident power,  $\Pi_{2,P}$  is the power radiated from the plate 2 without connections,  $\Pi_{2,B}$  is the power radiated from the plate 2 due to the action of the bridges,

$TL_p$  is the transmission loss of the double panel without connections. The ratio of the transmitted power may be expressed as [50]:

$$\frac{\Pi_{2,B}}{\Pi_{2,P}} = n\sigma_B \left| \frac{v_B}{v_1} \right|^2 \left\langle \left| \frac{v_1}{v_2} \right|^2 \right\rangle, \quad (1.5)$$

where  $\sigma_B$  is the radiation factor of the second plate driven by one of a number  $n$  bridges acting over the partition area  $S$ . The second term contains the velocities at the bridge location  $v_B$  and the average velocity of plate 1, dependent on the model taken into account for the bridges (e.g. rigid links, mass-spring-mass approximation). the ratio of the velocities can be obtained through the transfer matrix linking the force and the velocities at each side of the link, which is given in the case of a massless spring, by:

$$\left| \frac{v_B}{v_1} \right|^2 = \left| \frac{Z_{p1}}{T_{22}Z_{p1} + T_{11}Z_{p2} + T_{21}Z_{p1}Z_{p2} + T_{12}} \right|. \quad (1.6)$$

Here,  $Z_{pi}$  is the point impedance of the plates 1 and 2 and  $T_{ij}$  are the components of the transfer matrix linking the force and the velocities at each side of the link.

The last term in equation 1.5 is the averaged squared ratio of the velocities of plate 1 and 2 in the absence of the bridges. This term is obtained from the transfer matrix comprising the construction without the bridges (airborne path).

### Statistical energy analysis (SEA)

Many noise and vibration problems deal with complex structures consisting of many different components and very large ranges of frequencies. The combination of a high demand on time and computational resources makes conventional forms of analysis both uneconomic and unattractive. In addition, since the geometries and properties of the product are subjected to uncertainties, an estimation of the ensemble average response is often required. SEA models provide an alternative form to represent the system's vibroacoustic behaviour. In the SEA context, a complex vibroacoustic system is represented as an assembly of coupled subsystems that can receive, store, dissipate and transmit energy. The vibrational state is expressed in terms of vibrational energies of individual components; the applied excitations are expressed in terms of input powers and the coupling between

components is expressed in terms of energy flow. A detailed description of the method is performed in [38, 53–56].

References on SEA modelling of double-walls can be found in [3, 57–59]. Figure 1.9, from reference [3] shows a SEA model of a double-wall system with structural connections placed between a source and a receiving room. The square brackets indicate that the mechanism is non-resonant and the word inside the brackets identifies the component through which transmission occurs.

The possible transmission paths are:

- 1-2-5-3-4 represents the pure resonant path. It dominates at high frequencies, at which the cavity supports resonant modes and the panels are at their critical frequency regions or above,
- 1-2-[cavity]-3-4 occurs at low frequencies at the region where the cavity is not able to support modes with particle motion normal to the surface of the panels.
- 1-[wall]-5-[wall]-4 represents the non-resonant transmission through the panels while the cavity is in its resonant region. When one panel is in its resonant region while the other behaves in a non-resonant manner, transmission occurs through the following two paths: 1-2-5-[wall]-4 or 1-[wall]-5-3-4. These are important transmission paths in the frequency region below the panel’s critical frequency (in the case of an unstiffened panel).
- 1-2-[ties]-3-4 is dominant below the first longitudinal resonance of the connections,
- 1-[wall]-[cavity/ties]-[wall]-4 is the pure non-resonant transmission path, which is important at low frequencies (below the double-wall decoupling frequency).

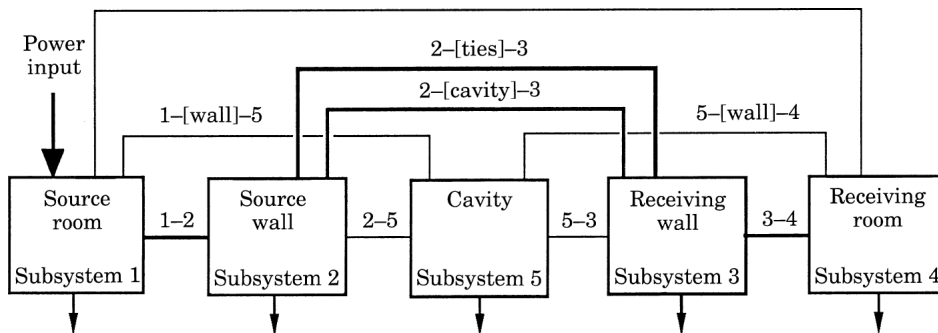


Figure 1.9 Statistical energy analysis model of a double-wall system with structural connections (from reference [3]).

In general, the power balance equations for  $N$  coupled subsystems may be written in matrix form in terms of the subsystems modal energies as:

$$\begin{bmatrix}
n_1 \left( \eta_{11} + \sum_{i \neq 1} \eta_{1i} \right) & -\eta_{21}n_2 & \cdot & -\eta_{N1}n_N \\
-\eta_{12}n_1 & n_2 \left( \eta_{22} + \sum_{i \neq 2} \eta_{2i} \right) & \cdot & \cdot \\
\cdot & \cdot & \ddots & \cdot \\
-\eta_{1N}n_1 & \cdot & \cdot & n_N \left( \eta_{NN} + \sum_{i \neq N} \eta_{Ni} \right)
\end{bmatrix}
\times
\begin{bmatrix}
\frac{E_1}{n_1} \\
\cdot \\
\cdot \\
\frac{E_N}{n_N}
\end{bmatrix}
=
\begin{bmatrix}
\Pi_1 \\
\cdot \\
\cdot \\
\Pi_N
\end{bmatrix},
\tag{1.7}$$

where  $\eta_{ij}$  is the coupling loss factor (CLF) between subsystems  $i$  and  $j$ ,  $E_i$  is the internal energy,  $\Pi_i$  is the input power,  $\eta_{ii}$  is the damping loss factor (DLF) and  $n_i$  is the modal density of subsystem  $i$ . In addition, the reciprocity relation is given by  $n_i\eta_{ij} = n_j\eta_{ji}$ .

This formulation is based on many hypothesis. The major ones are:

- coupling between subsystems is linear, low and conservative,
- reciprocity between subsystems is upheld,
- resonant modes in a particular frequency band have the same amount of energy,
- the damping loss factor is low and equal for all modes in a particular frequency band,
- power flow from subsystem to subsystem is due to resonant modes in the frequency band,
- power flow between subsystems is proportional to their energy level,
- the system is excited by random incoherent broadband noise,
- mode count in the frequency band is statistically high.

The power approach for modelling energy transmission between adjacent subsystems relies on the calculation of power flow between two connected subsystems. In principle CLF could also be determined experimentally knowing that injected energy in a subsystem equals the energy dissipated in this subsystem itself plus the transmitted energy to the connected subsystems. It is also suggested in [60] that knowing *a priori* the DLF of the driven subsystem from separated measurements, the total loss factor of the coupled subsystems can be measured and equated to the CLF (unknown) and DLF(known). However, when low coupling exists between both subsystems i.e. natural frequencies of both subsystems are not close enough, this method will not be appropriate since damping loss factor will tend to be up to two order of magnitude greater than the coupling loss factors [56].

Structural connections such as vibration isolators are then represented by a coupling loss factor between the two panels, which can then be determined from the above SEA system of

equations when only one panel is excited and using the reciprocity relation or by switching the excitation to the other panel. Analytically, they can be computed using a simplified formulation proposed in [3] or by using a periodic approach [61, 62].

A detailed description on the estimation of the SEA input parameters of plates is given in references [53, 60, 63–67]. The determination of the damping loss factor using the decay rate and the power injection methods is discussed [60, 63, 64]. The estimation of the input power and modal density from input mobility measurements is also outlined. In particular, the influence of shaker-structure interaction and impedance head response are addressed in [67]. A method to obtain damping and coupling loss factors using experimental SEA is described in [65, 66]. Practical issues such as ill-conditioning of the SEA matrix, matrix inversion techniques and equivalent mass estimations are discussed.

A path by path analysis is proposed by Craik [68] in order to obtain the sound transmission through structures from the sum of the contribution of individual paths. This approach is an alternative to the classical one, which relies on the solution of a series of simultaneous linear equations of a SEA system. The infinite possible paths from the source to the receiver is approximated by a finite number of paths with high contribution, while ignoring long paths with negligible contribution. Greater insight is thus given into the identification of dominant transmission paths. Examples of the applications of this approach can be found in aeronautical [69] and building [58] noise reduction context.

Several documents describe the application of SEA modelling in the context of aircraft interior noise [59, 69–76]. Lin [70] and Cordioli et al. [71, 72] mention the ease modelling of different sources of noise and vibration and the application of this approach in the early stages of design, considering the lack of detailed information about the new structure. Cotoni et al. [73] integrate a hybrid approach by modelling the isolators (coupling via complex junctions) and the frame stiffeners (stiff structures with low number of modes) using FEM. A general periodic SEA subsystem is also used in order to obtain SEA properties of large structures composed of a large number of unit cells. References [59, 75] emphasize that the accuracy of the model depends strongly on the accuracy of input parameters such as geometry, material properties, non-resonant transmission, cabin absorption, pressurization, isolators and input load (ECS, TBL, engine noise). Davis [69] recalls that uncertainties in the SEA model are mainly due to the following sources: input power, transfer functions, input parameters and the definition of the SEA model and subsystems. These uncertainties can be calculated using a power law prediction. In addition, a transfer path analysis is outlined using Craik’s algorithm [68]. Reference [76] describes the validation of an SEA model for predictions of noise inside the flight deck.

The difficulties in characterizing the TBL noise are pointed out. Finally, Peiffer et al. [77] present the general modelling strategy of a generic single aisle aircraft. They state that in mid and low frequencies some parts cannot be described by the SEA modelling due to their deterministic behaviour. Moreover, due to the lack of valid analytical models for complex structures, some parts such as the floor-fuselage linkage should be described by other modelling approaches such as the FEM method.

### Other approaches

Some other approaches to predict the sound transmission through double-walls, directed mainly to building acoustics, in which the airborne and the structure-borne transmissions are supposed independent and additive are outlined in [61]. They are the models of Sharp [51, 78], Fahy [35], Gu and Wang [79], and Davy [80, 81]. The first two only provide a rough estimation of the influence of the connections. By accounting for the resilient aspect and the resonant response of the links, Davy's model extended its range of applicability in the vicinity and above the critical frequency of the panels. However, in the context of lightweight structures when the mass of the connections are integrated, its agreement is reduced.

Legault et al. [61] developed a periodic model, treating the periodicity of the structure and links and adapting it for the case of aircraft structures. The studied structure is composed of two lightweight aluminium panels connected by five periodic aluminium c-shape stiffeners and insulated with glass wool. The connection via stiffeners are modelled either under a mass-spring-mass approximation, or as a beam-type with or without rigidity and mass. Results show that the presence of connections reduces the TL considerably at mid- and high-frequency ranges (above 300 Hz). In a second work [62], the authors integrate the modelling of composite plates, the Biot formulation to model the porous layer and the modelling of resilient mounts using a four-pole approach. The main conclusions are that the resilient mounts could reduce the structureborne transmission path but could however create undesirable resonances due to interactions with the panels.

At low frequencies, numerical methods are applied to solve the problem of complex geometries of finite structures. While finite element method (FEM) is mainly used in the prediction of the interior vibroacoustic response of stiffened structures, acoustic radiation inside a cavity [82–85], boundary element method [86] is used to treat the exterior problem. In general, the modal method is adopted for the structure, developing the vibration response in terms of the *in vacuo* eigenmodes of the structure. The fluid-structure coupling is described by an integral formulation. This approach allows for the characterisation of

the radiation mechanisms through modal phenomena. However, it is limited to a low frequency range since the number of modes increases with frequency, demanding thus a high computational effort. In addition, other drawbacks are linked to difficulties in modelling joints and predicting component interactions.

Elements having a low number of modes at certain frequency ranges can not be well characterised by the SEA approach. A hybrid approach, combining different modelling strategies could then be employed. One classical hybrid approach is SEA enhanced by virtual experimental data; it consists of modelling components with low mode count with a deterministic method (modal, FEM) and components with high modal density with a SEA method, then the components are coupled together. The coupling occurs through junctions referred to as hybrid junctions [77, 87–93]. This approach is similar to the standard SEA that employs CLF computed from experimental data. Since it makes use of the deterministic modelling, computational cost is higher in comparison to classical SEA.

Another approach is the SEA enhanced by the component mobility modelling technique. It is based on the input mobilities of deterministic and stochastic subsystems for determining the forced response of a system. It allows for evaluating the response of the structure as a whole from the knowledge of the dynamic properties of the different substructures respectively, which are known from their input mobilities [94].

### **1.3.4 Compression effects on the acoustic performance of porous materials**

During installation, the thermal and acoustic insulation present in aircraft cockpit can be submitted to a certain degree of compression and the effects related to its acoustical performance have to be studied. Castagnède et al. [95] describe the effect of compression on the absorption coefficient of porous materials by developing some heuristic formulas to predict the evolution of porous materials properties with compression. Results show that resistivity and tortuosity tend to increase with compression while porosity and characteristics lengths tend to decrease (a definition of the porous material properties can be found in [5]). The material is modelled as an equivalent fluid [5, 96–101] and different equations are proposed for a 1D or a 2D compression. The assumed hypotheses are that the acoustic incident field is normal to the material surface, the material is supposed to have a fibrous network, the fibres are supposed not experiencing any deformation during the compression and keep their initial radius unchanged and the compression rate is close to one (defined as the ratio between nominal and compressed thickness).

Castagnède et al. [102] also present measurements of the absorption coefficient of a standard fibrous material used in the automotive industry. The main effect caused by compression is the net diminution of the absorption coefficient mainly due to the decreasing in thickness, which is prominent in front of variations in porous materials properties. The opposite case of a 1D expansion shows a significant increase in the absorption coefficient. The influence of compression on the absorption coefficient of automotive felts is also treated, applying the equations derived previously. The measurements were performed for compression rates from 1 to 4. The main conclusions point out that the modelling used is not sufficient to capture the physics of the problem, especially concerning the porous material's airflow resistivity.

In the work of Wang et al. [103], further research on the compression of porous materials is carried out based on previous work by Castagnède et al. Here, the Biot's theory [5, 104, 105] is applied instead of the equivalent fluid model to consider the effect of the stiffness of the porous material. It is found out that by keeping the same thickness value constant and changing the fibrous properties, if the compression rate increases, the absorption coefficient increases at low frequencies, below the first absorption peak due to an increasing of the frictional viscous effect of the pores apertures. In parallel, at high frequencies, the airflow resistivity increases, causing a higher reflection of the incident sound, and thus, decreasing the absorption coefficient.

### 1.3.5 Vibration isolating mounts

In scientific literature, materials with long molecular chains are often referred to as elastomeric polymers. Due to their elevated deformability, damping capacity and wide range of mechanical properties, they have numerous applications in vibration control [106]. For those reasons, elastomeric mounts have been used for many years in order to reduce vibration between structures. In many applications, unwanted noise is a direct result of structural vibration, therefore, mounts also provide noise reduction benefits [107]. They are generally compact, cost-effective and maintenance-free.

Different types of vibration isolators exist depending on their application: from automobile engine mounts to building elastic mounts and boat engine shaft couplings. In aeronautical applications they are often used to connect a frame stiffener of the fuselage to the commercial lining. A representation of an elastomeric panel isolator for aircraft interiors manufactured by *LORD corporation* is shown in figure 1.10. It is composed of an outer member in aluminum, one inner member made of stainless steel and a silicone elastomer.

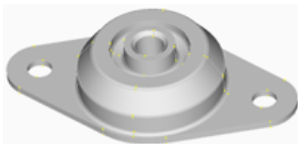


Figure 1.10 Elastomeric panel isolator for aircraft interiors manufactured by *LORD corporation*.

In order to predict the vibration transmitted through isolators over a large frequency range, information is required on the dependence of its properties on frequency. The vibration mount is classically integrated in transmission models as a mass and a complex stiffness term. The later can be determined based on experimental values, FEM or analytical modelling.

Several methods exist to measure mount's dynamic stiffness. They are described in details in the following documents [106, 108–113]. Reference [111] treats specifically of isolators for the aerospace industry application. Elastomeric mounts typically show a non-linear elastic and dissipative behaviour with respect to frequencies when excited with periodic forces. Moreover, the static preload applied to the elastomer also has an influence on the dynamics of the system. Other parameters influencing the stiffness measurement is the temperature and the velocity at which the specimen is deformed, in the case of the static stiffness [106]. Most measurements assume a linear vibration behaviour of the isolator for a given preload and temperature, and a point connection to the source and reception structures. It is pointed out that there is still a substantial room for improvement in passive elastomeric mounts by using nonlinear stiffness and damping characteristics [113].

Figure 1.11, adapted from reference [108], shows the structural path of the transmission through an isolator.  $F_i$  represent the orthogonal components of the force and of the moments and  $x_i$  represent the translational and rotational components of the displacement. Assuming only axial vibration, the equilibrium equations are given by equations 1.8.  $k_{11}$  and  $k_{22}$  are the input stiffness (when the opposite side  $x_2$  or  $x_1$  is blocked respectively).  $k_{12}$  and  $k_{21}$  are the blocked transfer stiffness, the ratio between the force at the blocked side and the displacement of the opposing side.

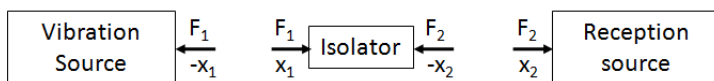


Figure 1.11 Schematic representation of the transmission through an isolator.

$$\begin{Bmatrix} F_1 \\ F_2 \end{Bmatrix} = \begin{vmatrix} K_{11} & K_{12} \\ K_{21} & K_{22} \end{vmatrix} \begin{Bmatrix} x_1 \\ x_2 \end{Bmatrix} \quad (1.8)$$

Noting  $k_r = -\frac{F_2}{x_2}$ , from equations 1.8 the dynamic stiffness of the reception structure at the connection point, the following relation is obtained:

$$F_2 = \frac{K_{21}}{1 + \frac{K_{22}}{k_r}} x_1. \quad (1.9)$$

If  $|K_{22}| < 0.1 |k_r|$ ,  $F_2$  tends to the blocked force. The equation 1.9 becomes  $F_{2\text{blocked}} = K_{21}x_1$ . Since isolators are efficient only when placed between structures having a high dynamic stiffness, this expression is a good approximation in most cases. If the condition  $|k_{22}| < 0.1 |k_r|$  is not satisfied, the term  $\frac{K_{22}}{k_r}$  should be taken into account.

A simple formulation accounting for efforts and movements only in the axial direction leads to 2x2 transfer matrix relating the force-velocity pair at each side of the mount (equation 1.8). Using this formulation, the mounts can be represented by a mass, a spring and a viscous damper and are characterised by their dynamic stiffness function. Other approaches exist including series and parallel combinations of those elements [112, 114–116]. More sophisticated approaches integrate other elements such as the influence of displacement amplitude on the dynamic stiffness by integrating friction damping [106]. Alternatively, in order to account for the fundamental modes of the outer case and of the elastomeric material, FEM is used [117, 118].

Assuming the mount is modeled by a mass  $M$  and a complex stiffness  $K^* = K(1 + j\eta)$ , where  $j = \sqrt{-1}$  and  $\eta$  the damping loss factor, the following system of equations can be derived:

$$\begin{Bmatrix} F_1 \\ F_2 \end{Bmatrix} = \begin{vmatrix} K(1 + j\eta) - \omega^2 M & -K(1 + j\eta) \\ -K(1 + j\eta) & K(1 + j\eta) \end{vmatrix} \begin{Bmatrix} x_1 \\ x_2 \end{Bmatrix},$$

where  $F_1$ ,  $x_1$ ,  $F_2$  and  $x_2$  are the force and displacement at the excitation point and at the blocked side respectively. Assuming  $K_{ij}$  are the elements of the transfer matrix such as represented in equation 1.8.

There are two main methods to measure the transfer and input dynamic stiffness: The first [108, 109] consists of measuring the transfer function between the acceleration at the excitation point and the force at the blocked displacement point. The second [108, 110, 112], consists of measuring the transfer function at the excitation point (using for example an impedance head).

The expressions relating the transfer functions to the dynamic stiffness and the damping loss factor are given in table 1.1 for the transfer and input dynamic stiffness:

Table 1.1 Transfer functions, (a) transfer and (b) input dynamic stiffness and damping loss factor calculated for a displacement  $x_2 = 0$ .

(a)	(b)
$\frac{F_2(\omega)}{x_1(\omega)} = K_{21} = -K(1 + j\eta)$	$\frac{F_1(\omega)}{x_1(\omega)} = K_{11} = K(1 + j\eta) - \omega^2 M$
$K = -Re(K_{21})$	$K = \frac{Re(R)}{ R ^2(1-r^2)}$
$\eta = -\frac{Im(K_{21})}{Re(K_{21})}$	$\eta = -\frac{Im(R)(1-r^2)}{Re(R)}$

In table 1.1,  $R = \frac{1}{K_{11}}$  is the receptance function and  $r = \frac{f}{f_n}$  is the frequency  $f$  normalized by the natural frequency  $f_n$  of the system.

The direct accelerance curve can be obtained from the manipulation of the term  $K_{11}$  and is given by:

$$\frac{a_1}{F_1} = \left| \frac{-\omega^2}{M(\omega_0^2 - \omega^2 + j\eta\omega\omega_0)} \right|, \quad (1.10)$$

with,  $\omega_0 = \sqrt{\frac{K}{M}}$ .

From the measured accelerance, it is possible to estimate the modal damping at the resonance using the half power method:

$$\eta = \frac{f_2 - f_1}{f_0}. \quad (1.11)$$

$f_0$  is the resonance frequency,  $f_1$  and  $f_2$  are the low and high frequency limits respectively, at which the amplitude of the accelerance is reduced by a factor of 2.

The damping of the system can also be calculated from the time response of the acceleration transducer. It is given by:

$$\eta = 2 \frac{\delta}{\sqrt{4\pi^2 + \delta^2}}, \quad (1.12)$$

where  $\delta = \ln \left( \frac{a(t)}{a(t+T)} \right)$  and  $a(t)$  is the acceleration signal of period  $T$ .

In order to validate the static stiffness and damping values calculated from interpolation of the dynamic curves at low frequencies, some static and quasi-static tests can be performed. The static test consists of monitoring the traction-compression forces,  $F$ , applied to the

isolator while measuring its displacement,  $x$ . The static stiffness  $k_{stat}$  is then obtained from the ratio force over displacement  $k_{stat} = \frac{F}{x}$ .

The aerospace test specification [111] states that the static stiffness should be calculated from a hysteresis curve at a low frequency (figure 1.12) using the following formulation:

$$k_{stat} = k_{16} - k_c, \quad (1.13)$$

where,  $k_{16} = \frac{k_{12} + k_{56}}{2}$ ;  $k_{12} = \frac{F_2 - F_1}{S_2 - S_1}$ ;  $k_{56} = \frac{F_5 - F_6}{S_5 - S_6}$ ;  $F_1, F_2, F_5, F_6$  are load values;  $S_1, S_2, S_5, S_6$  are displacement values and  $k_c$  is the parasitic or correction stiffness coming from the test set up and calculated analogue to  $k_{16}$  using a rigid dummy as test sample. In figure 1.12  $F_{pu}$  and  $F_{pl}$  are the maximum and minimum load respectively.

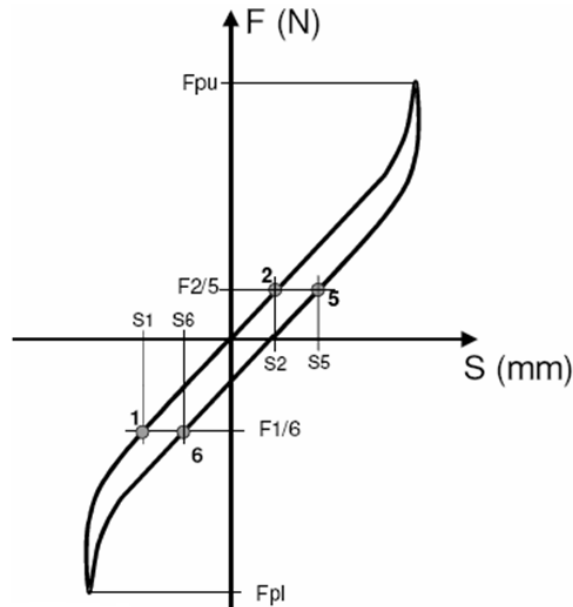


Figure 1.12 Hysteresis curve for an elastomeric isolator (from ASD-STAN prEN 4662 standard).

The damping loss factor,  $\eta$ , can be obtained using the following relation [119]:

$$\eta = \frac{\Delta E}{2\pi U_{max}}. \quad (1.14)$$

$\Delta E$  is the energy dissipated per cycle and  $U_{max}$  is the maximum of the potential energy of the system, given by  $U_{max} = \frac{k_{stat} x_{max}^2}{2}$ . Here the static stiffness is obtained from the slope of the hysteresis curve as described above and  $x_{max}$  is the maximum displacement of the mount during a cycle.

## 1.4 Summary and methodology

The industrial application of this project consists of developing a simple and accurate tool for sound transmission predictions and optimisation of aircraft double-wall at the pre-design phase of conception. Considering the state-of-the-art on the vibroacoustic modelling of double-wall structures under different excitation fields as well as the importance of structure-borne transmission through mechanical links, the choice of an energy based model has been found the most adapted for the following reasons: (1) compared to other methods, it allows for the description of a structure through its global vibroacoustic parameters rather than detailed geometry information, (2) it is well suitable for the studied random excitation fields, (3) mechanical links are integrated via an equivalent coupling between panels rather than a detailed modelling of the junction elements, (4) the identification of dominant transmission path is readily available from the input parameters and (5) the computational time is low and adapted to optimisation studies. Moreover, future improvements related to in-flight aircraft applications e.g. stiffened panels, curvature, pressurization, excitation sources and temperature can be readily integrated by modifying input parameters feeding the model.

In consequence, the research is divided into the following 3 tasks:

1. Characterise the effects of porous material compression on the sound transmission of the fuselage structure and comparison with tests,
2. Develop a model taking into account the structure-borne transmission through a representative double wall system with isolating mounts,
3. Analyse sound transmission mechanisms for a double-wall under acoustic and structural excitation fields and comparison with tests.

The first task is carried out for a thin aluminium panel lined with a fibrous material. At first, the porous material properties, such as the airflow resistivity, density and longitudinal Young's modulus and loss factor are measured under different compression rates in the direction normal to its thickness. Measurements of Transmission loss for the structure are also performed under different compression rates and results are compared to simulations using the transfer matrix method.

In the framework of the second task, a double-wall SEA model is developed for a typical lightweight aircraft double-wall under diffuse acoustic field. Transmission loss measurements are performed for this structure for validation purposes. The main input parameters feeding the model are also measured in order to compare with theoretical estimations.

They are the panels' modal density, radiation efficiency and damping loss factor and their transmission loss in single-wall configurations. In addition, the structure-borne transmission is integrated in the model via a coupling loss factor (CLF) between panels. The structural CLF integrates measured dynamic stiffness of typical aircraft vibration isolators. It is also validated experimentally.

The third task comprises the modelling and validation of a double-wall under structural excitation. For this purpose, transmission measurements are performed on a double-wall under point forces at random locations. The vibroacoustic behaviour of the structure is then compared to the acoustic excitation. In addition, a transfer path analysis is performed in order to determine the importance of airborne and structure-borne transmissions for both excitations in each studied frequency band.

The report is organized in 6 chapters. The main outcomes of the research are summarized in 4 scientific papers. Following this first introductory chapter, the influence of compression of the glass wool layer on the transmission loss of a covered panel is analysed in chapter 2. It is composed of a scientific paper published in *Applied Acoustics*. Chapter 3 is devoted to the modelling of the structural transmission via vibration isolators and subsequently integration into the double-wall SEA model. Results are presented in a scientific paper published in the *Noise Control Engineering Journal*. The transmission through uncoupled double-walls is analysed in chapter 4 using two modelling approaches for quick assessment of vibroacoustic indicators: the transfer matrix method and statistical energy analysis. Results are also compared with measurements on representative double-walls. A paper submitted to *Acta Acustica united with Acustica* presents the main findings while supplementary results are given at the end of this chapter. The assessment of the sound transmission through mechanically-coupled double-walls is discussed in chapter 5. Results under diffuse field excitation are presented in a paper that will be submitted to the *Journal of the Acoustical Society of America*. Results under spatially uncorrelated point-forces are discussed separately. Finally, chapter 6 draws general conclusions as well as perspectives for future work.



# CHAPTER 2

## INFLUENCE OF FIBROUS MATERIAL COMPRESSION ON THE SOUND TRANSMISSION OF COVERED PANELS

### 2.1 Chapter introduction

Noise inside the cockpit and cabin is mainly transmitted via two transfer paths: (1) airborne transmission through the cavity between primary (fuselage) and secondary (lining) structures and (2) structure-borne transmission via mechanical links between these structures. This chapter is composed by a paper published in *Applied Acoustics*. It is devoted to the modelling of airborne transmission through porous materials used as thermo-phonic insulation. Particularly, the effect of compressing such materials (e.g. during installation in aircraft) on their insulation performance is investigated. Information on the paper and its abstract are given hereafter in French. In parallel to this analysis, next chapter addresses the structure-borne transmission via links between panels. Outcomes of these two studies are to be integrated in the double-wall model strategy shown in Fig. 1.3 and developed in chapters 4 and 5.

Ce chapitre présente l'article intitulé "*Effect of porous material compression on the sound transmission of a covered single leaf panel*", publié dans *Applied Acoustics Journal*.

#### **Auteurs et affiliation :**

B. Campolina : Airbus Operations SAS, Acoustic and Environmental Department, Route de Bayonne, 316 F31060 Toulouse Cedex 09, France.

N. Dauchez : LISMMA, Institut Supérieur de Mécanique de Paris, 3, rue Fernand Hainaut, 93407 Saint-Ouen, France.

N. Atalla : GAUS, Department of Mechanical Engineering, Université de Sherbrooke, Sherbrooke, Quebec, Canada J1K 2R1.

O. Doutres : GAUS, Department of Mechanical Engineering, Université de Sherbrooke, Sherbrooke, Quebec, Canada J1K 2R1.

**Date d'acceptation :** 20/02/2012.

**Etat de l'acceptation :** Version finale publiée.

**Revue :** Applied Acoustics Journal.

**Référence :** B. Campolina et al. Effect of porous material compression on the sound transmission of a covered single leaf panel. Appl Acoust (2012), doi:10.1016/j.apacoust.2012.02.013.

**Titre français :** Effet de la compression d'un matériau poreux sur la perte par transmission d'une plaque recouverte.

## 2.2 Résumé de l'article publié dans le journal Applied Acoustics

Cet article a pour objectif la détermination de l'effet sur la perte par transmission (TL) de la compression d'une couche de matériau fibreux en contact avec une plaque isotrope. La configuration étudiée est constituée de deux plaques isotropes de fréquences critiques autour de 2300 Hz et 9700 Hz, et d'un matériau fibreux d'une épaisseur de 2 pouces. Un modèle utilisant la méthode des matrices de transfert est utilisé en considérant le matériau poreux à squelette indéformable (modèle de fluide équivalent), souple (modèle *limp*) ou élastique (modèle de Biot). Des mesures de résistivité au passage de l'air en fonction du taux de compression montrent que les modèles classiques de compression sont uniquement valables pour de faibles taux de compression. La perte par transmission théorique est ensuite comparée aux données expérimentales dans la gamme de fréquence de 100 Hz à 10 kHz pour trois taux de compression, 0%, 20% et 50%. Le fibreux est comprimé de façon uniforme sur la totalité de sa surface. Les résultats expérimentaux montrent que la compression réduit le TL de 5 dB maximum, pour une compression de 50% de l'épaisseur du poreux. Cet effet est visible principalement en moyennes fréquences, autour de 800 Hz. Il est dû à une résonance dans l'épaisseur du poreux, qui augmente l'efficacité de rayonnement de la structure en moyennes fréquences. Par ailleurs, la diminution de l'épaisseur du poreux et l'augmentation de sa résistivité au passage de l'air avec la compression sont les principales causes du changement de TL de la structure. Ces tendances sont aussi observées avec les modèles de fluide équivalent (*limp* et squelette indéformable) mais avec une moindre précision comparée au modèle poroélastique.

Mots clé : Matériaux poreux ; Compression ; Perte par transmission ; Propagation du son.

**Paper published on the Applied Acoustics Journal**

## Effect of porous material compression on the sound transmission of a covered single leaf panel

### Abstract

In this paper, the authors examine the effect of compressing a poroelastic fibrous layer lined with an isotropic plate on the sound transmission loss (TL). For this purpose, a 2-inch thick fibrous material and two isotropic plates with critical frequencies around 2300 Hz and 9700 Hz were used. The transfer matrix method was applied and the porous layer was assumed to have either a rigid, limp or elastic frame. Current models of compression are outlined, and measurements of the airflow resistivity as a function of compression show that these models are suitable only for low compression rates. TL predictions are compared next to experimental data in a range between 100 Hz to 10000 Hz for three compression rates, corresponding to 0%, 20% and 50%. The fibrous is uniformly compressed over 100% of its surface. Our experiments showed that compression reduces the TL by a maximum of 5 dB for a 50% compression, mainly at the mid-frequency range, around 800 Hz. This is due to a resonance in the thickness of the porous material, increasing the radiation efficiency of the structure at mid-frequencies. Moreover, reduction of the porous thickness and increase of the airflow resistivity with compression are the variations influencing the most the TL of the structure. These trends were also detected with the limp and rigid frame models but with a lower degree of accuracy compared to the elastic frame model.

**keywords:** Porous material, Compression, Transmission Loss, Sound propagation.

## 2.3 Paper published on the Applied Acoustics Journal - Introduction

Acoustic comfort has become a high priority in automotive, building and aeronautical structures subjected to noise. Passive acoustic treatments such as porous materials [5], diffusers [120, 121], acoustic and membrane resonators [122, 123] have been constantly studied and optimized in terms of acoustical properties and reduction of mass, in order to fit modern industrial constrains. This paper treats of compression effects on porous materials. During installation such materials can be subjected to a certain degree of compression, with consequent changes in their frame properties and thickness. In aeronautical applications, as the context of the present research, compression can result from the installation of equipment, cables and ventilation grids. It is thus non-uniform and changes

locally the properties of the sound package. This may impact the targeted efficiency of the treatment. Castagnède et al. [95, 102] has proposed simple formulas to modify the material properties to account for the influence of uniform compression on the absorption coefficient. Their work was limited to fibrous and felt materials. Wang et al. [103] has applied their formulation using an elastic approach for the material. However, a similar study related to the transmission loss (TL) has not been performed. This is the subject of the present work.

The studied material is a glass wool and the effect of its frame compression on the TL of a structure composed of an isotropic plate lined with a porous layer is investigated both analytically and experimentally. First, the theoretical aspects of sound propagation and compression of porous materials are introduced in section 2. Section 3 presents the test structure and describes the experimental procedure to obtain its TL. The experimental and theoretical results are compared and discussed in section 4. Finally, the effect of compression on the TL is analysed in terms of variations in porous properties, radiation efficiency and wave-number.

## 2.4 Theory

In this section, the models used for the porous layer are presented. Recent results on the effect of compression are discussed, and a summary is provided on the theory for modelling the propagation of sound through a multilayer structure composed of solid, fluid or porous material.

### 2.4.1 Modelling sound absorbing materials

Poroelastic materials may be modeled using an equivalent fluid approach under the assumption that the solid phase is either rigid [5, 96–98] or limp [99–101]. Without these assumptions, Biot’s model is required [5, 104, 105].

In Biot’s model, the poroelastic medium is described by the macroscopic displacement of solid and fluid phases represented by  $\mathbf{u}^s$  and  $\mathbf{u}^f$ , respectively. One shear and two compression waves propagate in the poroelastic medium. The expressions of the three wave numbers are given in Appendix 2.8. The two equations of movement form the following coupled system [5]:

$$\begin{aligned}
 -\omega^2 \tilde{\rho}_{11} \mathbf{u}^s - \omega^2 \tilde{\rho}_{12} \mathbf{u}^f &= N \nabla^2 \mathbf{u}^s + \\
 + (\tilde{P} - N) \nabla \nabla \cdot \mathbf{u}^s + \tilde{Q} \nabla \nabla \cdot \mathbf{u}^f, &
 \end{aligned} \tag{2.1}$$

$$-\omega^2 \tilde{\rho}_{12} \mathbf{u}^s - \omega^2 \tilde{\rho}_{22} \mathbf{u}^f = \tilde{Q} \nabla \nabla \cdot \mathbf{u}^s + \tilde{R} \nabla \nabla \cdot \mathbf{u}^f, \tag{2.2}$$

with  $\omega$ , the angular frequency;  $\tilde{P}$  and  $\tilde{R}$ , the compression modulus of the frame and fluid, respectively;  $N$ , the shear modulus of the frame;  $Q = (1 - \phi) \tilde{K}_f$ , the elastic coupling modulus between the two phases, including thermal effects, with  $\tilde{K}_f$  the effective compressibility modulus;  $\tilde{\rho}_{11}$  and  $\tilde{\rho}_{12}$ , the densities of the frame and fluid phases, respectively, including viscous effects; and  $\tilde{\rho}_{12}$  accounts for the viscous coupling between the two phases. The tilde indicates that the physical property is complex and frequency dependent.

Under the rigid frame assumption  $\mathbf{u}^s = 0$ , only one compression wave propagates with wave number:

$$\delta_f = \omega \sqrt{\frac{\tilde{\rho}_f}{\tilde{K}_f}}. \tag{2.3}$$

Equations 2.1 and 2.2 reduce to a single equation:

$$\tilde{K}_f \nabla^2 \mathbf{u}^f + \omega^2 \tilde{\rho}_f \mathbf{u}^f = 0 \tag{2.4}$$

where  $\tilde{\rho}_f$  is the effective fluid density. Expressions of  $\tilde{\rho}_f$  and  $\tilde{K}_f$  are given in Appendix 2.8. In the Johnson-Champoux-Allard model [5] they depend on five porous material properties: flow resistivity  $\sigma$ , porosity  $\phi$ , tortuosity  $\alpha_\infty$  and viscous and thermal characteristic lengths  $\Lambda$  and  $\Lambda'$ .

The limp porous theory assumes a frame with no bulk stiffness,  $\tilde{P} = 0$ . It should be noted that  $\tilde{P} = \frac{E(1+j\eta)(1-\nu)}{(1-2\nu)(1+\nu)}$  is a variable depending on the Poisson's ratio  $\nu$ , the structural loss factor  $\eta$  and the Young's modulus  $E$  of the material [101]. This leads to a relation between  $\mathbf{u}^s$  and  $\mathbf{u}^f$ , simplifying the equations 2.1 and 2.2 to a modified single equation:

$$\tilde{K}_f \nabla^2 \mathbf{u}^f + \omega^2 \tilde{\rho}_{limp} \mathbf{u}^f = 0, \tag{2.5}$$

where  $\tilde{\rho}_{limp}$  is the effective density of the equivalent fluid. Its expression is given in Appendix 2.8. The corresponding wave number is

$$\delta_{limp} = \omega \sqrt{\frac{\tilde{\rho}_{limp}}{\tilde{K}_f}}. \quad (2.6)$$

A recent criterion has been derived in [100] in order to determine if the porous layer can be modelled under the limp assumption (Frame Stiffness Influence). Its frequency independent form [101] is given by:

$$FSI_r = \frac{|\tilde{P}|}{2P_0}, \quad (2.7)$$

where  $P_0 = 101.3$  kPa is the isothermal bulk modulus of the air in the pores. Its value should be below 0.1 for the present configuration to consider that the limp model could be used [101].

### 2.4.2 Effects of compression on porous physical parameters

The theory presented in this section has been extracted from papers [95, 102, 103] treating the compression of fibrous materials. The compression rate ( $n$ ) is defined as:  $n = \frac{h_0}{h}$ , where  $h_0$  and  $h$  are the nominal and the compressed thickness, respectively. Since only the compression case is presented in this paper,  $n$  is greater than 1. The anisotropy effect during compression is not taken into account.

For a low compression rate, simple heuristic formulas have been proposed by Castagnède *et al.* [95, 102] to characterize compression of the fibrous network in terms of variations in material properties. The material is modelled as an equivalent fluid. Different equations are proposed for a uniaxial and surface-like compression. Variations in flow resistivity, porosity and characteristic lengths are calculated theoretically while variations in the tortuosity are determined from ultrasonic measurements.

The assumed hypotheses are as follows: the incident acoustical field is normal to the material surface. The material is supposed to have a fibrous network, the fibres of which are not supposed to experience any deformation during the compression of the material. Their initial radius remains unchanged and the compression rate is close to one.

Since the fibre layers are independent, illustrated by the fact that the Poisson's ratio is considered zero, the fibre radius remains unchanged during the compression process. The

fibres are then brought closer together. A compressed porous layer presents a decrease in its porosity and characteristic lengths while the tortuosity and the airflow resistivity increase.

Castagnède *et al.* [95] has presented measurements for the absorption coefficient of a standard fibrous material used in the automotive industry. The main effect caused by compression is the reduction of the absorption coefficient due mainly to the decreased thickness, which is prominent compared to variations in porous materials properties. Similar behaviour is encountered for an expansion of the porous material. An excellent agreement is found in terms of absorption coefficient between experimental and predicted data.

In a second paper, Castagnède *et al.* [102] study the influence of compression on the absorption coefficient of automotive felts applying the equations (2.8-2.12). Measurements were carried out for compression rates from 1 to 4. The main conclusions on the proposed formulas point out a fair agreement for porosity and characteristic lengths, an approximate one for the tortuosity and a poor agreement with regard to the flow resistivity.

For a 1D compression rate the porous materials properties vary according to [95]:

$$\alpha_{\infty}^{(n)} = 1 - n(1 - \alpha_{\infty}^{(1)}), \quad (2.8)$$

$$\phi^{(n)} = 1 - n(1 - \phi^{(1)}), \quad (2.9)$$

$$\sigma^{(n)} = n\sigma^{(1)}, \quad (2.10)$$

$$\Lambda^{(n)} = \frac{\Lambda^{(1)}}{\sqrt{n}} + \frac{a}{2} \left( \frac{1}{\sqrt{n}} - 1 \right), \quad (2.11)$$

$$\Lambda'^{(n)} = \frac{\Lambda'^{(1)}}{\sqrt{n}} + \frac{a}{2} \left( \frac{1}{\sqrt{n}} - 1 \right), \quad (2.12)$$

where the superscripts represent the compression rate.  $a$  is the mean fibre diameter, neglected in this work since the fibres are much thinner compared to 15  $\mu\text{m}$ , as taken in [95].

Wang *et al.* [103] provide further research on porous material compression based on previous work by Castagnède *et al.*[95, 102]. In Wang's study, Biot's theory is applied instead of the equivalent fluid model to consider the effect of the stiffness of the porous material. Equations (2.8-2.12) linking the compression rate to the porous material's properties are used, and since the elastic properties are considered, one additional equation is proposed

concerning the change in density during compression:

$$\rho^{(n)} = n\rho^{(1)}. \quad (2.13)$$

Experiments show that when fluid-structure coupling is achieved inside the porous layer, Biot's theory should be used due to mechanical resonance. For materials with high airflow resistivity values, the effect of frame elasticity should also be considered.

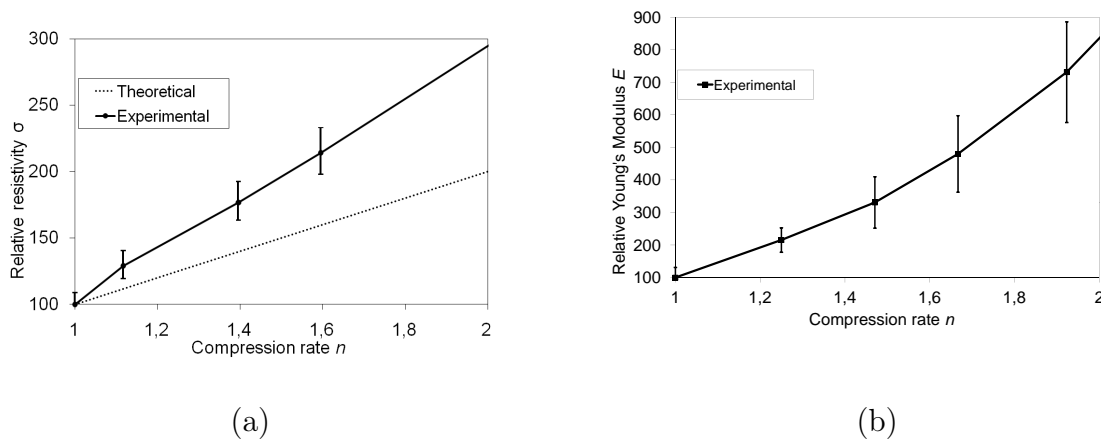


Figure 2.1 Relative variation of physical parameters as a function of uni-axial compression rate of a fibrous layer (base 100 for  $n=1$ ): a) airflow resistivity, b) Young's modulus.

Some measurements of the flow resistivity [124] of the studied sample have been performed at certain compression rates and confronted to the current analytical model (figure 2.1 a). The theory is shown to be inaccurate at high compression rates. In consequence, measured values will be used in TL predictions. In addition, since the published models [95, 102, 103] do not include the variation of the apparent Young's modulus in the compression direction, some measurements [125] have also been made since this property is needed in Biot's model. Results are shown in figure 2.1 b. Properties of the used fibrous material are presented in table 1.

### 2.4.3 Sound transmission through multilayer structures

Plane wave propagation through layers of solids, fluids and porous can be modelled by using transfer matrices [5, 126]. The system studied is composed of an isotropic plate and a layer of fibrous material immersed in air. Figure 2.2 represents the incident and reflected

waves at side (i), the solid (1) and the porous (2) layers, and the transmitted wave at side (o).

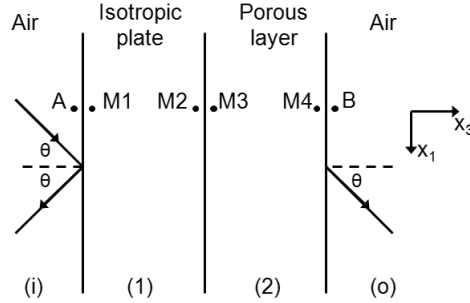


Figure 2.2 Schematical illustration of the studied structure.

Each layer is considered to be of infinite lateral dimensions but the final results are corrected to take into account the dimensions of the measurement window [127]. Inside the porous material, six waves (incident and transmitted) propagate under Biot's model assumption. They are characterized by their velocities  $v$  and stresses  $\sigma$  using the following vector :  $V_p = [v_1^s \ v_3^s \ v_3^f \ \sigma_{33}^s \ \sigma_{13}^s \ \sigma_{33}^f]^T$  where  $s$  and  $f$  stand for solid and fluid, and the subscripts are related to their principal directions. The propagation through  $M_1 - M_2$  is given by  $V_s(M_1) = [T_s] V_s(M_2)$ , where  $[T_s]$  is the transfer matrix of the solid layer. The same reasoning applies for the  $M_3 - M_4$  propagation; this is detailed in [5]. Boundary conditions at interfaces  $A - M_1$ ,  $M_2 - M_3$  and  $M_4 - B$  are the continuities of velocities and stresses.

The power transmission coefficient averaged over all possible angles of incidence  $\bar{\tau}$ , is given by the following equation:

$$\bar{\tau} = \frac{\int_0^{\theta_L} \tau(\theta) \sin(\theta) \cos(\theta) d\theta}{\int_0^{\theta_L} \sin(\theta) \cos(\theta) d\theta}, \quad (2.14)$$

with  $\tau = |T(\theta)|^2$ .  $T(\theta)$  is the ratio of the amplitudes of the incident and transmitted waves and  $\theta_L$ , the maximum incident angle, assumed  $85^\circ$ . The transmission loss is then given by  $TL = 10 \log(\frac{1}{\bar{\tau}})$ .

The transfer matrix theory is implemented in commercial software Maine 3A<sup>1</sup>, used in this work.

1. Maine 3A, Centre de Transfert de Technologie du Mans (CTTM), Le Mans - France, www.cttm-lemans.com

## 2.5 Description of the experiment

Several TL measurements are carried out in order to validate the theory concerning the compression effect on a multilayer structure. The structure is placed between two environments: a small reverberant room and an anechoic room. A front picture and a cut-view of the measured structure are shown in figure 2.3.

The structure dimensions are (904 mm x 804 mm). The plate is pinned between two wooden frames by rubber strips and the fibrous is uniformly compressed by a metallic grid sufficiently rigid to support the compression stress without deformation. It is made of vertical beams of section 2 mm x 29 mm spaced by 33 mm and horizontal beams of section 2 mm x 8 mm spaced by 43 mm. The cell size is so that the effect of the grid on the TL can be neglected for the present purpose.

The main difference between simulated configurations and experiments is that the simulated compression of the fibrous does not generate a force distribution on the plate as in the experimental case.

Two isotropic plates, presenting critical frequencies ( $f_c$ ) of 9700 Hz and 2300 Hz were tested, and are henceforth referred to respectively as thin and thick plates. They are assumed to have the following properties: Young's modulus,  $E = 72.4$  GPa; Poisson's ratio,  $n = 0.33$ ; material density,  $\rho_p = 2700$  kg.m<sup>-3</sup>. A porous material 50.8 mm thick (2 inches), used in aeronautical applications, is lined with the plate. Three configurations were tested for each plate: material with nominal thickness, 20% and 50% compressed; corresponding to the compression rates of  $n=1$ ,  $n=1.25$  and  $n=2$ , respectively. The material is uniformly compressed over 100% of its surface. Measured porous properties for each compression rate are presented in table 1. Density and speed of sound in the fluid phase are  $\rho_0 = 1.213$  kg.m<sup>-3</sup> and  $c_0 = 342.2$  m.s<sup>-1</sup>.

The transmission loss of the structure is given by:

$$TL = 10 \log \left( \frac{W_I}{W_T} \right), \quad (2.15)$$

where  $W_I$  is the incident sound power measured in the emission room and  $W_T$  is the transmitted sound power measured in the reception room.

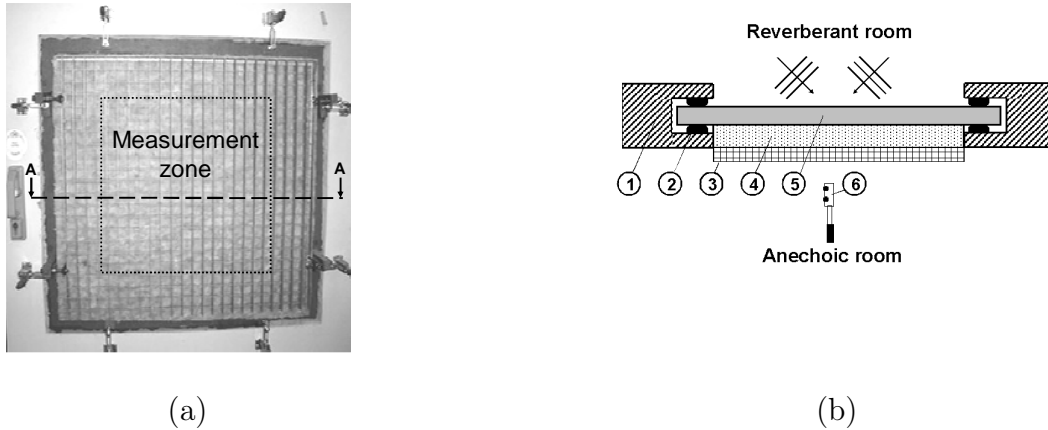


Figure 2.3 Experimental set-up: a) Tested structure, b) A-A cut view: 1- Room's wall, 2- Rubber strip, 3- Rigid metallic grid, 4- Fibrous sample, 5- Isotropic plate, 6- Intensimetry probe.

Table 2.1 Porous material properties measured for each compression rate,  $n=1$ ,  $n=1.25$  and  $n=2$ .

Property	Symbol	Unit	$n=1$	$n=1.25$	$n=2$
Density of the material	$\rho$	$\text{kg.m}^{-3}$	9.6	12	19.2
Young's modulus	$E$	Pa	2091	4501	15285
Loss factor	$\eta$	-	0.115	0.127	0.136
Flow resistivity	$\sigma$	$\text{N.s.m}^{-4}$	23735	37000	71000
Porosity	$\phi$	-	0.97	0.96	0.94
Tortuosity	$\alpha_\infty$	-	1.07	1.09	1.14
Viscous c. length	$\Lambda$	$\mu\text{m}$	64.10	57.33	45.33
Thermal c. length	$\Lambda'$	$\mu\text{m}$	98.50	88.10	69.65

A diffuse field is generated inside the reverberant room. A spatial average of the pressure level is obtained from microphones located at three different points in the emission room. From the pressure signal, the incident sound power ( $W_I$ ) can be deduced:  $W_I = S \frac{\langle p^2 \rangle}{4\rho c}$ , where  $\langle p^2 \rangle$  is the quadratic mean pressure measured by the microphones and  $S$  is the surface of the sample. The transmitted sound power ( $W_T$ ) is measured by intensimetry:  $W_T = S \cdot I_T$ , where  $I_T$  is the intensity measured by a probe composed of two 1/2 inch microphones set 12 mm apart. The measurement is done by manually scanning the surface of the sample with the intensimetry probe with the purpose of obtaining a spatial and temporal average. In addition, only the central part of the sample surface is covered by the probe (figure 2.3a) to avoid sound leaks coming from the edges. The quality of the measurement is validated by measuring the  $\delta_{pi}$  index according to [128].

All measurements are achieved in third-octave bands using broadband noise from 300 Hz to 5000 Hz. The lower limit corresponds to the minimum frequency where the field can be considered diffuse inside the reverberant room. The higher frequency limit is associated with the distance between probe microphones.

## 2.6 Results and discussion

In this section, experimental and theoretical results are compared. The influence of the variations of fibrous parameters due to compression is also discussed.

### 2.6.1 Influence of compression on the TL response

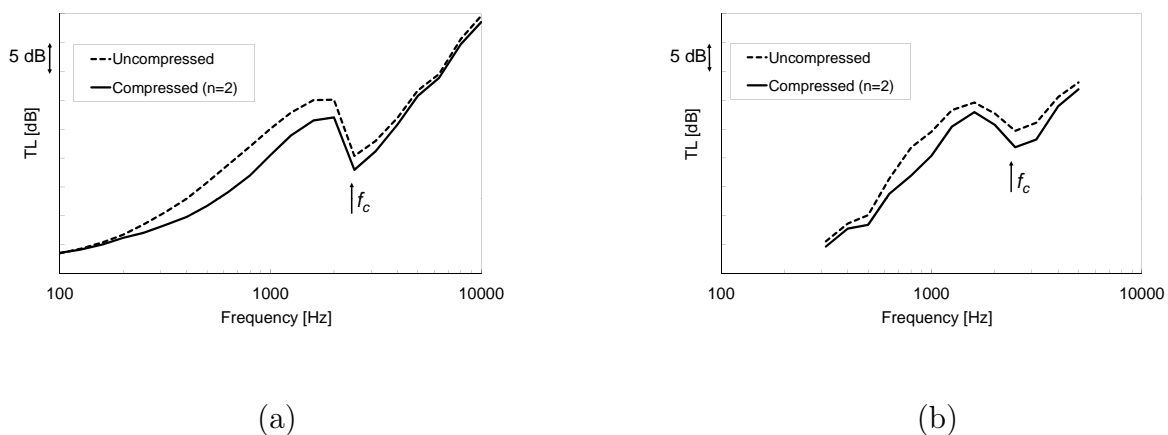


Figure 2.4 Responses of the thick plate with glass wool: a) prediction, b) measurement

TL responses are presented in figure 2.4 for the thick plate with fibrous material for uncompressed and compressed configurations. It is observed that compression reduces the TL in both theoretical and experimental cases. To compare the differences between the two cases,  $\Delta TL$  curves are plotted in figure 2.5 for the system with the thin (a), and thick (b) plates. Here,

$$\Delta TL = TL_c - TL_b \quad (2.16)$$

is the difference between the  $TL_c$  of a given configuration and the  $TL_b$  of the baseline configuration.

Measured  $\Delta TL$  results show, for the thin plate, a decrease in the TL of 1 and 3 dB for  $n$  equal to 1.25 and 2, respectively, in the mid-frequency range. For the thick plate, the

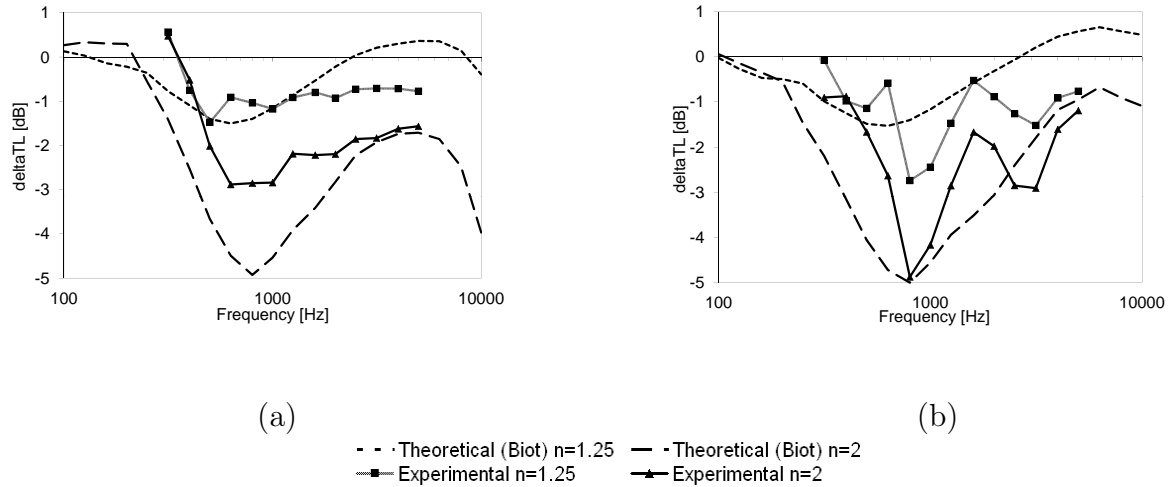


Figure 2.5 Influence of a  $n=2$  compression of the porous layer on the TL: a) thin plate, b) thick plate.

values are of the order of 3 and 5 dB around 800 Hz. Discrepancies between experiments and predictions for the thin plate at  $n=2$  may be due to the pre-stress imposed to the plate when the fibrous layer is compressed by the grid. It modifies slightly the shape of the thin plate that tends to behave as a shell. This is not accounted for in the simulation. This influence is negligible for the thick plate, which is more stiff.

## 2.6.2 Influence of fibrous properties on the TL

To determine the effect of each fibrous property on the TL, only one parameter was modified at a time using the  $n=2$  compressed configuration. Here, the baseline configuration is assumed as being the thick plate lined with the uncompressed fibrous layer. The deltaTL between the modified configuration and the baseline configuration is calculated. Of all the physical parameters, the three with the greatest influence on this configuration are the thickness, the airflow resistivity and the density of the frame.

It is observed in figure 2.6 that a reduction of the thickness of the porous deteriorates the TL of the structure. In parallel, compressing the porous material increases its resistivity. This has a double effect on the TL. It deteriorates the response at mid frequencies but improves it at high frequencies. It can be thus concluded that thickness and resistivity effects are minimal at low frequencies, while they reduce the TL at mid-frequencies and act in opposite direction at high-frequencies. In addition, density variation acts as an added-

mass effect, almost constant over the entire frequency range. Finally, Young's modulus (added stiffness) influence is found to be negligible.

The stiffness of the material is very small and its influence is found to be negligible, which is coherent with the  $FSI_r$  criterion, as given by equation 2.7. It is 0.01, 0.02 and 0.08 for the  $n=1$ ,  $n=1.25$  and  $n=2$  configurations, respectively. These values are below the threshold of approximately 0.1, given in [101] for the radiation configuration. Note however that for a compression rate of 2,  $FSI_r$  approaches the threshold.

In order to focus on the influence of the frame stiffness and inertia, deltaTL given by limp and rigid frame models are compared to poroelastic model. Figure 2.7 shows the results for the thick plate under  $n=1.25$ , and  $n=2$ . It is observed that the three models predict similar behaviour. The limp curve presents better results in comparison to the rigid one up to 2000 Hz, notably at the frequency range where the effect of compression is maximum, around 800 Hz, and for a small compression rate (Figure 2.7a). This means that the mass effect is prominent in comparison with the stiffness effect. The conclusions are similar for the thin plate configuration.

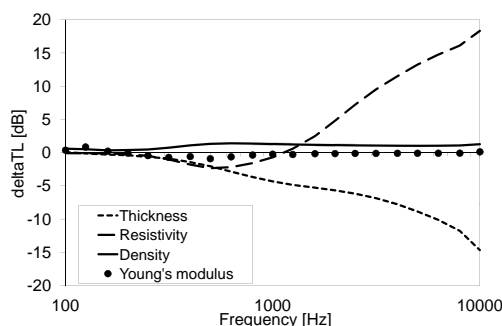


Figure 2.6 Predicted influence of variations in fibrous parameters due to a  $n=2$  compression on the TL of the system with the thick plate.

### 2.6.3 Influence of compression on the radiation efficiency

Figure 2.8 shows predicted radiation efficiency ( $\sigma_s$ ) of the system with the thin plate, mechanically excited by spatially uncorrelated point forces. It is given by:  $\sigma_s = \frac{\Pi_{rad}}{\rho_0 c_0 \langle v^2 \rangle}$ . Here,  $\Pi_{rad}$  is the power radiated by the system and  $\langle v^2 \rangle$  is the mean quadratic velocity of the plate. Another excitation field is applied in these simulations in order to verify that the changes in the transmission are intrinsic to the compression of the porous layer.

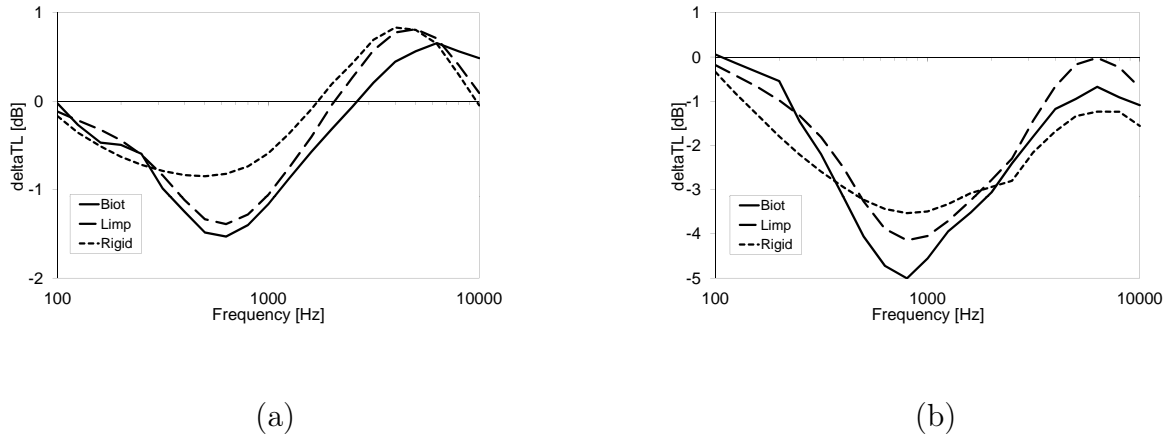


Figure 2.7 Comparison of the response of the rigid frame, limp and Biot models for the system with the thick plate: a)  $n=1.25$ , b)  $n=2$ .

The curves are obtained using a modal approach as described in [129] and a limp porous modeling.

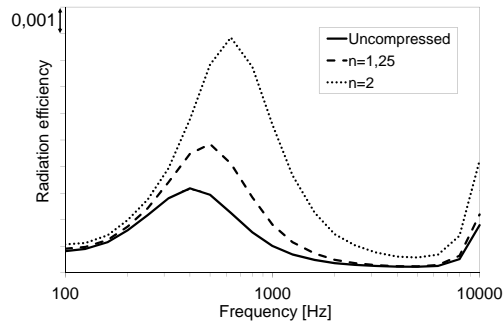


Figure 2.8 Radiation efficiency of the structure with the thin plate under mechanical excitation.

The peak observed in the curves is due to a resonance of the porous layer in its thickness,  $h$ . Moreover, an increase of the radiation efficiency is also noticed near the critical frequency of the thin plate.

For a porous layer backed by a pressure release, pressure  $p = 0$ , this resonance occurs when  $\lambda = 4h$ , where  $\lambda$  is here the wavelength of the limp wave. This resonance is called a quarter-wavelength resonance and leads to the wavenumber  $k = \frac{\pi}{2h}$  for a normal incidence plane wave excitation [130], however, this frequency is modified by the presence of the air as receiver medium.

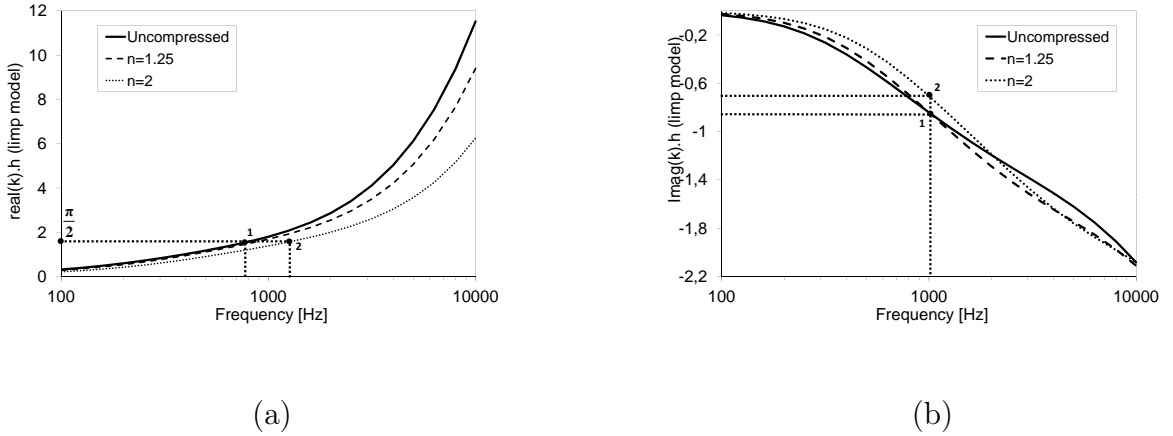


Figure 2.9 Limp porous material wavenumber multiplied by the thickness: a) real part, b) imaginary part.

Here  $k = k_R + jk_I$  and the wavenumber dependence  $e^{-jkx_3} = e^{-jk_R x_3} e^{k_I x_3}$  is assumed, for a plane wave of normal incidence, using the notation of figure 2.2. The real and imaginary parts of  $k$  multiplied by the thickness are related to the period of the wave and its attenuation, respectively.

Two effects are observed from figure 2.8: (i) compression shifts the resonance value to high frequencies and (ii) increases the radiation efficiency, mainly at mid-frequencies. The first effect happens since the couple wavenumber-thickness of the porous,  $k_R x_3$ , decreases with compression. Points 1 and 2 in figure 2.9(a) show the shift from the uncompressed to the compressed resonance frequency, occurring when  $kh = \frac{\pi}{2}$ . The second effect is due to a decrease of the couple  $|k_I x_3|$  in the mid-frequency range from the uncompressed to the compressed configuration, as shown by points 1 and 2 in figure 2.9(b).

## 2.7 Conclusion

This work addresses the influence of a fibrous material compression on the TL response of a covered panel. The compression lowers the TL at the mid-frequency range mainly. This is due to an amplification of the resonance in the thickness of the porous material, increasing the radiation efficiency of the structure at mid-frequencies. Moreover, reduction of the porous thickness and increase of the airflow resistivity with compression are the variations influencing the most the TL of the structure. They have minimal effects on the TL at low frequencies while tend to reduce the TL at mid-frequencies and act in opposite direction at high frequencies (figure 2.6). Measurements show that the TL decreases by up

to 5 dB for a uniform compression of 50% over the fibrous entire surface, in the thick plate configuration. For an aircraft cockpit, the effect is reduced since the compression rate is lower and compression occurs locally. Moreover, it is observed that the structure can be modeled under the limp frame assumption for low compression rates only. To complement the study, work on the variation of the fibrous viscoelastic parameters due to compression could be extended to the double wall case using for example the method proposed in [131], where modifications to the materials absorption and transmission play a more prominent role.

## Acknowledgments

The authors are grateful to D. Fonseca and A. Garcia, students at the Ecole Nationale Supérieure d'Ingénieurs du Mans (ENSIM) for their contribution. A. Geslain, PhD student at the Laboratoire d'Acoustique de l'Université du Maine (LAUM) and Centre de Transfert de technologie du Mans (CTTM) team are also acknowledged for the help during the experiments.

## 2.8 Appendix: Modelling sound absorbing materials (complementary theory)

Expressions of the effective fluid density,  $\tilde{\rho}_f$  and effective compressibility modulus,  $\tilde{K}_f$ :

$$\tilde{\rho}_f = \alpha_\infty \rho_0 \left[ 1 + \frac{\sigma \phi}{j \omega \rho_0 \alpha_\infty} \sqrt{1 + \frac{4j \alpha_\infty^2 \eta \rho_0 \omega}{\sigma^2 \Lambda^2 \phi^2}} \right], \quad (2.17)$$

$$\tilde{K}_f = \left[ \frac{\gamma P_0}{\gamma - (\gamma - 1)} \right] \cdot \left\{ 1 + \frac{\sigma' \phi}{j B^2 \omega \rho_0 \alpha_\infty} \sqrt{1 + \frac{4j \alpha_\infty^2 \eta \rho_0 \omega B^2}{\sigma'^2 \Lambda^2 \phi^2}} \right\}, \quad (2.18)$$

where  $P_0$  is the ambient pressure,  $\sigma' = \frac{8\alpha_\infty \eta}{\phi \Lambda^2}$ ,  $\gamma$  is the adiabaticity constant (ratio of specific heats),  $\eta$  is the air viscosity and  $B^2$  is the Prandtl number.

Expressions of the three complex wave numbers according to Biot's theory are presented next.  $\delta_{1,2}$  are related to the compression waves while  $\delta_3$  is related to the shear wave:

$$\delta_{1,2}^2 = \frac{\omega^2}{2(\tilde{P}\tilde{R} - \tilde{Q}^2)} \left[ \tilde{P}\tilde{\rho}_{22} + \tilde{R}\tilde{\rho}_{11} - 2\tilde{Q}\tilde{\rho}_{12} \pm \sqrt{\Delta} \right] \quad (2.19)$$

$$\delta_3^2 = \frac{\omega^2}{N} \left( \frac{\tilde{\rho}_{11}\tilde{\rho}_{22} - \tilde{\rho}_{12}^2}{\tilde{\rho}_{22}} \right). \quad (2.20)$$

Here,  $\Delta = \left( \tilde{P}\tilde{\rho}_{22} + \tilde{R}\tilde{\rho}_{11} - 2\tilde{Q}\tilde{\rho}_{12} \right)^2 - 4 \left( \tilde{P}\tilde{R} - \tilde{Q}^2 \right) \left( \tilde{\rho}_{11}\tilde{\rho}_{22} - \tilde{\rho}_{12}^2 \right)$ ,

$$\tilde{\rho}_{11} = \rho_1 + \rho_a - j\sigma\phi^2 \frac{G_j(\omega)}{\omega},$$

$$\tilde{\rho}_{12} = -\rho_a + j\sigma\phi^2 \frac{G_j(\omega)}{\omega},$$

$$\tilde{\rho}_{22} = \rho_0 + \rho_a - j\sigma\phi^2 \frac{G_j(\omega)}{\omega},$$

$$G_j = \sqrt{1 + \frac{4j\alpha_\infty^2 \eta \rho_0 \omega}{\sigma^2 \Lambda^2 \phi^2}},$$

where  $\rho_a = \phi\rho_0(\alpha_\infty - 1)$  is the inertial coupling term and  $\rho_1$  is the density of the solid phase.

Expression of the density of the air modified by the inertia effect of the solid phase and its interaction with the fluid phase,  $\tilde{\rho}_{limp}$ , according to the limp model

$$\tilde{\rho}_{limp} = \phi \frac{\rho_t \tilde{\rho}_f / \phi - \rho_0^2}{\rho_t + \tilde{\rho}_f / \phi - 2\rho_0}. \quad (2.21)$$

In this equation  $\rho_t = \rho_1 + \phi\rho_0$  is the total apparent mass of the fluid with  $\rho_1$  being the density of the porous material and  $\rho_f$ , the effective density of the fluid phase of the "rigid frame equivalent fluid" model, given by equation 2.17.



# CHAPTER 3

## MODELLING OF COUPLING LOSS FACTOR OF AIRCRAFT DOUBLE-WALLS COUPLED VIA VIBRATION ISOLATORS

### 3.1 Chapter introduction

Following the airborne sound transmission modelling presented in chapter 2, this chapter describes the transmission through structure-borne paths. It is composed by a paper published in the *Noise Control Engineering Journal* (NCEJ). Aircraft double-wall panels are mechanically connected via rigid links or elastomeric mounts. A four-pole approach is used to represent the structural links, based on their mass and stiffness. Then, a method is developed to include the structure-borne transmission path in the SEA model via a coupling loss factor between panels. Information on the paper and its abstract are given hereafter in French. Chapter 4 describes the structurally-decoupled double-wall model while chapter 5 addresses the sound transmission through mechanically-coupled double-walls.

Dans ce chapitre, l'article intitulé "*Four-pole modelling of vibration isolators: Application to SEA of aircraft double-wall panels subjected to mechanical excitation*" est présenté. Il a été publié dans *Journal of Noise and Control Engineering*.

#### **Auteurs et affiliation :**

B. Campolina : Airbus Operations SAS, Acoustic and Environmental Department, Route de Bayonne, 316 F31060 Toulouse Cedex 09, France.

N. Atalla : GAUS, Department of Mechanical Engineering, Université de Sherbrooke, Sherbrooke, Quebec, Canada J1K 2R1.

N. Dauchez : LISMMA, Institut Supérieur de Mécanique de Paris, 3, rue Fernand Hainaut, 93407 Saint-Ouen, France.

P. Neple : Airbus Operations SAS, Acoustic and Environmental Department, Route de Bayonne, 316 F31060 Toulouse Cedex 09, France.

**Date d'acceptation :** 01/02/12.

**Etat de l'acceptation :** Version finale publiée.

**Revue :** Journal of Noise and Control Engineering.

**Référence :** B. Campolina et al. Four-pole modelling of vibration isolators: Application to SEA of aircraft double-wall panels subjected to mechanical excitation, Noise Control Eng. J. 60 (2), Jan-Feb 2012, DOI: 10.3397/1.3688316.

**Titre français :** Modélisation de liens anti-vibratiles par l'approche quadripolaire : application à la méthode SEA pour une double-paroi d'avion sous excitation structurale.

## 3.2 Résumé de l'article publié dans le journal NCEJ

Cet article a pour objectif la détermination du facteur de perte par couplage (CLF) entre deux plaques connectées par des liens anti-vibration, en utilisant un modèle quadripolaire. Une approche de type Analyse Statique Energétique (SEA) intégrant des résultats expérimentaux a été développée pour deux configurations. La première configuration comprend deux plaques isotropes dont les fréquences critiques sont autour de 3750 Hz et 6000 Hz. La deuxième configuration, plus représentative d'un fuselage d'avion, est constituée d'un panneau isotrope raidi et d'un panneau sandwich. Les plaques sont couplées entre elles en 6 points par des liens élastomères. Elles sont excitées mécaniquement par une force ponctuelle dont la position est aléatoire. La gamme de fréquence considérée s'étend de 10 Hz à 10 kHz. La modélisation des liens intègre des valeurs de raideur mesurées fonction de la fréquence. Pour cette mesure quatre configurations sont comparées et la plus adaptée est, par la suite, utilisée. Les CLF modélisés sont comparés aux mesures effectuées en utilisant l'approche SEA expérimentale. Enfin, les vitesses quadratiques moyennes des plaques sont calculées en utilisant le modèle hybride et comparées avec les résultats expérimentaux. Les résultats montrent une bonne corrélation entre les CLF modélisés et mesurés. Cependant, un raffinement du modèle est nécessaire afin d'intégrer le couplage par rayonnement au niveau des fréquences critiques des plaques.

Mots clé : Facteur de perte par couplage ; Analyse statistique énergétique ; Liens anti-vibration ; Transmission structurale.

**Paper published on the NCEJ Journal**

## Four-pole modelling of vibration isolators: application to SEA of aircraft double-wall panels subjected to mechanical excitation

### Abstract

This paper aims at determining the structural coupling loss factor (CLF) between two plates connected via vibration isolators, using a four-pole approach. A hybrid Experimental-SEA (statistical energy analysis) model has been developed for predictions and two configurations are analysed: Configuration 1 is composed of two isotropic plates with critical frequencies around 3750 Hz and 6000 Hz. Configuration 2, more representative of an aircraft fuselage, is composed of a stiffened isotropic plate and a sandwich panel. Plates are coupled at 6 locations via elastomeric mounts. They are mechanically excited by a point force at random positions in the 100 Hz to 10000 Hz frequency range. The modelling of the isolators integrates their frequency dependent measured stiffness. Four configurations are compared for the stiffness measurement and the most adapted setup is derived. The modelled CLFs are then compared with measurements using an experimental SEA approach. Finally, the space-averaged quadratic velocities of the plates are calculated using the hybrid model and compared with experiments. Results show a good correlation between predicted and measured CLFs but further refinement is needed in order to account for radiation coupling near the critical frequencies of the plates.

**keywords:** Coupling loss factor, Statistical energy analysis, Vibration isolator, Structural transmission.

INCE subject classification numbers: 46.2 Vibration isolators, 75.2 Statistical energy Analysis (SEA)

### 3.3 Paper published on the NCEJ Journal - Introduction

Vibration isolators, such as elastomeric mounts, have been used for many years in order to reduce vibration from being transmitted from one structure to another. In many applications, unwanted noise is a direct result of structural vibration. Therefore, mounts also provide noise reduction benefits [107]. In aeronautical applications, as in the present case, they are placed between a frame stiffener of the fuselage and the commercial lining.

The context of the present study is the determination of the sound transmission through aircraft fuselage structures. The proposed modelling is used to integrate the structural transmission path through vibration isolators in a typical double-wall statistical energy analysis (SEA) model, also accounting for airborne transmission. This paper is focused on the determination of structural coupling loss factor (CLF) between two plates connected via isolators.

The modelling of structural transmission between coupled plates has been the subject of several recent work [52, 62, 132–135]. Craik [132] included in a double-wall SEA model a coupling via building wall ties by determining the mobility of the leaves and of the ties, respectively. Poblet [133] studied the influence of the shape of studs on the vibroacoustic transmission. Vigran [52] introduced structural connections in the transfer matrix method (TMM). Legault [62] integrated a four-pole modelling of isolators for periodic structures. In addition, Ewing [134] and Wang [135] studied the statistical energy analysis of plates coupled via rigid and resilient connectors.

The proposed approach uses a four-pole method [62, 135] integrating experimental axial dynamic stiffness of the isolators. For this purpose, 4 measurement setups [108–112, 116, 136] are compared and the best setup, for a typical aircraft shock mount, is identified. Next, a validation of predicted CLFs is carried out using experimental SEA [38, 53–56] for 2 double-wall configurations. Configuration 1 is composed of two thin isotropic plates and configuration 2, more representative of an aircraft fuselage, is composed of a stiffened isotropic panel and a sandwich panel. A discussion is then presented on the determination of SEA parameters needed to compute the experimental CLF, particularly damping loss factors (DLF) and modal densities of the plates [53, 60, 67, 137].

The theoretical and experimental SEA approaches, as well as the four-pole modelling of the isolators are introduced in section 2. Measurements of the dynamic stiffness of the isolators and CLF of two plates connected via shock mounts are described in section 3. Finally, section 4 is devoted to a discussion on measurement results of dynamic stiffness together with a comparison between theoretical and experimental CLF and vibration transmissibility.

## 3.4 Theory

In this section, SEA equations of the double-wall are introduced and the isolator equations of the four-pole approach [62, 135] are derived.

### 3.4.1 SEA modelling of a double-wall

Many noise and vibration problems involve very large ranges of frequencies and complex structures, which are composed of elements having different shapes. The combination of a high demand on time and computational resources, as well as uncertainties in structure properties makes conventional forms of analysis uneconomic and unattractive. The SEA models provides an alternative form to represent the vibroacoustic behaviour of a structure.

In the SEA context, a complex vibroacoustic system is represented as an assembly of coupled subsystems that can receive, store, dissipate and transmit energy. The vibrational state is expressed in terms of vibrational energies of individual components; the applied excitations are expressed in terms of input powers and the coupling between components is expressed in terms of energy flow. A detailed description of the method is given in [14-18].

The studied system is represented in Fig. 3.1. It is composed of two subsystems, plates 1 and 2 in flexural vibration, connected through isolators. One plate is excited by a point force  $F$  at random locations, with white noise as input.

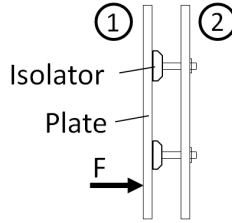


Figure 3.1 Schematic representation of the double-wall system.

The theoretical approach of the SEA consists in computing the energy level of the subsystems considering other SEA parameters are known. The SEA parameters of the system are the modal densities of the plates  $n_i$  (with  $i$  corresponding to a subsystem), the damping loss factors  $\eta_{ii}$ , the coupling loss factors  $\eta_{ij}$ , the total dynamic energy  $E_i$  and the input power  $\Pi_i$ . The SEA equations are given by the following linear system and the reciprocity relation  $n_1\eta_{12} = n_2\eta_{21}$ :

$$\begin{bmatrix} \eta_{11} + \eta_{12} & -\eta_{21} \\ -\eta_{12} & \eta_{21} + \eta_{22} \end{bmatrix} \begin{Bmatrix} E_1 \\ E_2 \end{Bmatrix} = \begin{Bmatrix} \frac{\Pi_1}{\omega} \\ 0 \end{Bmatrix}. \quad (3.1)$$

Alternatively, the experimental approach of the SEA consists in estimating damping and coupling between subsystems from their experimental energy levels. CLF between plates can be determined using the following equation [65–67, 138]:

$$\eta_{12} = \frac{\frac{\Pi_1}{\omega} - \eta_{11}E_1}{E_1 - \frac{n_1}{n_2}E_2}. \quad (3.2)$$

$E_i$  are obtained from the measurement of the space-averaged quadratic velocity of the plates using the relation  $E_i = m_i \langle v_i^2 \rangle$ , where  $m_i$  is the total mass of the plate and  $\langle \rangle$  represents an average over time, frequency and excitation positions.  $n_i$  are either obtained from theory or measurements.  $\eta_i$  are measured from the decay of the time response of the plate when excitation is turned off, using the decay rate method (DRM) or alternatively, by a power input method (PIM) [53]. Finally,  $\Pi_i$  are measured using an impedance head.

An important indicator used in this paper for comparison between theoretical and experimental approaches is the vibration transmissibility ( $VT$ ), defined as the logarithm of the ratio between the space-averaged quadratic velocities of the non-excited and excited plates:

$$VT = 10 \log_{10} \left( \frac{\langle v_2^2 \rangle}{\langle v_1^2 \rangle} \right). \quad (3.3)$$

### 3.4.2 Isolator modelling and structural coupling loss factor determination

The isolator is represented by a transfer matrix  $T$  linking the axial force  $F_i$  and displacement  $x_i$  at its left and right sides as given by the system of equations:

$$\begin{Bmatrix} F_1 \\ x_1 \end{Bmatrix} = \begin{bmatrix} T_{11} & T_{12} \\ T_{21} & T_{22} \end{bmatrix} \begin{Bmatrix} F_2 \\ x_2 \end{Bmatrix}. \quad (3.4)$$

Several approaches exist to model vibration isolators [62, 106, 114, 115]. Here, it is modelled as a lumped mass-spring-mass system [62] as shown in Fig. 3.2. Only axial loading is accounted for in the model. Non-axial contributions are particularly important for curved structures or when the spacing between links is high. The total mass of the isolator  $M_m$  is split equally between the two plates and the stiffness is given by the model of Eqn. (3.5), where  $\eta_m$  is the DLF of the isolator:

$$K^* = K(1 + j\eta_m). \quad (3.5)$$

For this case, the transfer matrix  $T$  takes the following form:

$$T = \begin{bmatrix} 1 - \frac{M_m \omega^2}{2K^*} & -M_m \omega^2 \left(1 - \frac{M_m \omega^2}{4K^*}\right) \\ \frac{1}{K^*} & 1 - \frac{M_m \omega^2}{2K^*} \end{bmatrix}. \quad (3.6)$$

The CLF via the vibration isolator  $\eta_{12}$  is obtained from the power balance equation:

$$N\Pi_{12} = \eta_{12}\omega E_1. \quad (3.7)$$

Here  $\Pi_{12}$  is the power transmitted to plate 2 via the isolator and  $N$  is the number of isolators. Independent motion at each connection point is assumed. This is valid provided that the structural wavelength is much lower than the separation between connections. This condition is satisfied for frequencies higher than 150 Hz for the 3.2 mm plate and 115 Hz for the trim panel [32, 137]. In this case, the total transmitted power is expressed as the sum of the transmitted power for each isolator. Finally,  $E_1$  is the total energy of the first plate. Expressing the power input as a function of the real part of the plate's driving point impedance  $Re(Zp_2)$  and the average of the quadratic velocity at each isolator location on plate 2  $\langle v_{2t}^2 \rangle$ ,  $\eta_{12}$  is given by Eqn. (3.8), where  $\tau = \frac{\langle v_{2t}^2 \rangle}{\langle v_1^2 \rangle}$ ,

$$\eta_{12} = \frac{N Re(Zp_2) \tau}{\omega m_1}. \quad (3.8)$$

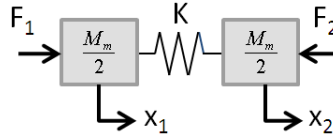


Figure 3.2 Schematic representation of the isolator.

The driving point impedance  $Zp_i$  of a flat plate is given by  $Zp_i = \frac{4m_i}{n_i}$ . The ratio  $\tau$  is given by Eqn. (3.9) and is derived from the equations of motion of the two lumped masses of the isolator, Eqn. (3.4), assuming  $F_1 = Zp_1(\langle v_1 \rangle - \langle v_{1t} \rangle)$  represents the total axial force applied by plate 1 to the left side of the isolator, where  $\langle v_{1t} \rangle$  is the average of the velocity at each isolator location on plate 1, and  $F_2 = Zp_2 \langle v_{2t} \rangle$ :

$$\tau = \left| \frac{Zp_1}{T_{22}Zp_1 + T_{11}Zp_2 + j\omega T_{21}Zp_1Zp_2 + \frac{T_{12}}{j\omega}} \right|^2. \quad (3.9)$$

## 3.5 Description of the experiments

In this section two series of measurements are described: the first one refers to the dynamic stiffness of the isolators, integrated in the transfer matrix  $T$  of the four-pole modelling, Eqn. (3.6). The second one comprises measurements of SEA parameters in order to validate theoretical CLF, given by Eqn. (3.8), with experimental CLF, given by Eqn. (3.2).

### 3.5.1 Measurement of isolator's dynamic stiffness

Several methods exist to measure isolator's dynamic stiffness. They are described in details in the following references [108–112, 116, 136]. Reference [10] treats specifically of isolators for the aerospace industry application. Elastomeric isolators typically show a non-linear elastic and dissipative behaviour with respect to frequency when excited with periodic forces. Moreover, the static preload applied to the elastomer has an influence on the dynamics of the system. Other parameters influencing the stiffness measurement are the temperature and the relaxation phenomenon [106, 139]. The measurement method presented in this paper assumes a linear vibration behaviour of the isolator for a given preload and temperature, and a point connection to the source and receiving structures.

The following system of equations is a rearrangement of Eqn. (3.4).

$$\begin{Bmatrix} F_1 \\ F_2 \end{Bmatrix} = \begin{vmatrix} k_{11} & k_{12} \\ k_{21} & k_{22} \end{vmatrix} \begin{Bmatrix} x_1 \\ x_2 \end{Bmatrix}. \quad (3.10)$$

Here,  $k_{11}$  and  $k_{22}$  are the input stiffness (when the opposing side  $x_2$  or  $x_1$  is blocked respectively).  $k_{12}$  and  $k_{21}$  are the blocked transfer stiffness, i.e. the ratio between the force at the blocked side and the displacement of the opposing side.

Noting  $k_r = -\frac{F_2}{x_2}$ , the dynamic stiffness of the structure at the connection point, the following relation is obtained:

$$F_2 = \frac{k_{21}}{1 + \frac{k_{22}}{k_r}} x_1. \quad (3.11)$$

If  $|k_{22}| \ll 0.1 |k_r|$ ,  $F_2$  tends to the blocked force and Eqn. (3.11) simplifies to:

$$F_{2 \text{ blocked}} = k_{21} x_1. \quad (3.12)$$

Since isolators are efficient only when placed between structures having a high dynamic stiffness, this expression is a good approximation in most cases. If the condition  $|k_{22}| \ll 0.1 |k_r|$  is not satisfied, the term  $\frac{k_{22}}{k_r}$  should be taken into account. In Eqn. (3.12)  $k_{21} = K^*$ , the DLF of the isolator is thus:

$$\eta_m = \frac{Im(k_{21})}{Re(k_{21})}. \quad (3.13)$$

Four setups for the dynamic stiffness measurements are examined in this paper. They are presented in Fig. 3.3. Setups (a), (b) and (c) are used to measure the blocked transfer dynamic stiffness  $k_{21}$ . Setups (a) and (b) can also be used to measure the input dynamic stiffness  $k_{11}$ . The differences between (a) and (c) are related to the rigid backing, the loads applied to the isolator and the input acceleration which is measured in (a) using an impedance head and in (c) using 2 accelerometers. Setup (b) makes use of an impact hammer instead of a shaker.

Setup (d) corresponds to static and hysteresis tests, performed for validation of dynamic measurements at low frequencies. The static test consists of monitoring the traction-compression force,  $F$ , applied to the isolator while measuring its displacement,  $x$ . The static stiffness  $k_0$  is then derived from the ratio of force over displacement  $k_0 = \frac{F}{x}$ . Hysteresis tests consist of determining isolator's stiffness from the slope of the hysteresis curve at a given low frequency [111]. The DLF,  $\eta_m$ , can be obtained using the relation [119]:

$$\eta_m = \frac{\Delta E}{2\pi U_{max}}. \quad (3.14)$$

$\Delta E$  is the energy dissipated per cycle and  $U_{max}$  is the maximum of the potential energy of the system, given by  $U_{max} = \frac{k_0 X^2}{2}$ . In this equation  $k_0$  is calculated from the slope of the hysteresis curve and  $X$  is the maximum displacement of the isolator during a cycle.

The test bench used for static and hysteresis tests is the MTS 858 Mini Bionix II.

### 3.5.2 SEA measurements on a double-wall

Experimental SEA tests are also performed in order to determine CLF between the two plates using Eqn. (3.2). The tested configurations 1 and 2 are shown in Fig. 3.4a and 3.5a, respectively. The first one is composed of two aluminium plates,  $h_1 = 2$  mm and  $h_2 = 3.2$  mm thick respectively, suspended at the edges and having a surface area of 1.5 m<sup>2</sup>. The Young's modulus of the plates is  $E = 69$  GPa and their poisson ratio is  $\nu = 0.33$ .

The two plates are connected at 6 locations via rigid studs. Two connection configurations are tested: (1) soft coupling using vibration isolators between the stud and the plate (Fig. 3.4b) and (2) rigid coupling. In the latter, only the stud is used to connect the plates. One plate is excited by an electro-mechanic shaker with white noise input.

Panels in configuration 2 have the same surface area as on configuration 1. They are composed of a 2 mm thick aluminium plate with 6 horizontal stiffeners and 3 vertical stiffeners, regularly spaced, and a 12.7 mm thick sandwich-honeycomb panel. The two panels are also connected at 6 points but, instead of using rigid studs, they are connected through the vertical stiffeners (frames) of the aluminium panel. The vibration isolator or an equivalent rigid element is placed between the stiffener and the sandwich panel to obtain the two coupling configurations. Fig. 3.5b and Fig. 3.6 show the detail of the stiffeners and connections.

Input power and quadratic velocities of the plates are averaged over 3 shaker positions to simulate a rain-on-the-roof excitation (uncorrelated point forces at random positions). Quadratic velocities are also space-averaged over 4 measurement locations. A prior averaging is performed for configuration 1 over 30 locations and differences are within 1 dB. The location of the isolators, accelerometers and excitation points are shown in Fig. 3.7.

Damping tests are performed separately for each plate without connections. Two experimental approaches are compared: the decay rate method (DRM) and the power input method (PIM) [53, 63]. The comparison is performed considering that measurements of damping are approximate and often subjected to large errors. The main sources of damping are: (i) internal friction and viscous losses, (2) radiation, (3) boundaries and (4) coupling. Since plates are suspended and tested separately without connections, the last two components are neglected. Results are averaged in one-third octave bands over different excitation and response locations.

DRM is based on the transient decay response of accelerometers placed on the plates surface when the source is turned off. Two assumptions are made: damping follows an exponential decay and all modes in a third-octave band present the same DLF [53].

For a given third-octave band of centre frequency  $f$  and slope of the decay  $DR$  in units of dB/second, the DLF is found to be [53]:

$$\eta_{ii} = \frac{DR}{27.3f}. \quad (3.15)$$

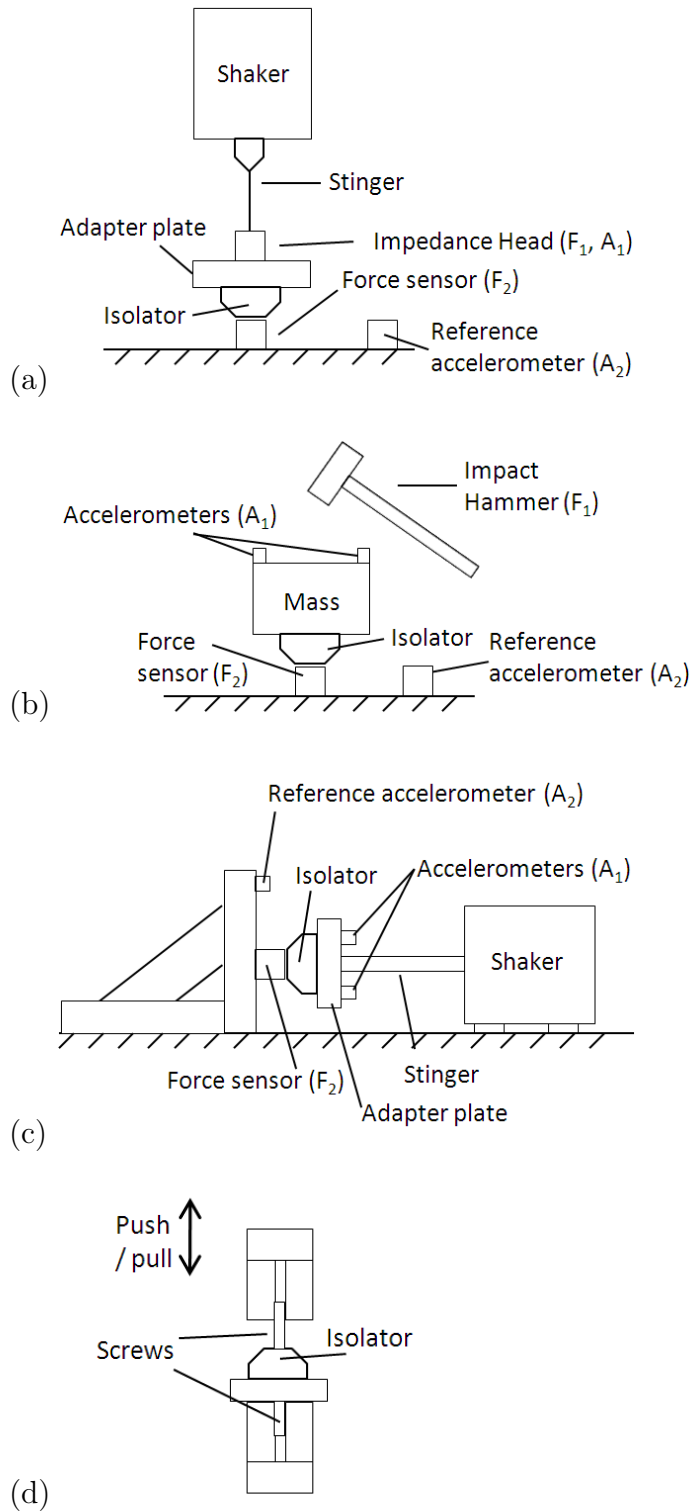


Figure 3.3 Measurement setups: (a) Vertical, (b) Impact hammer, (c) Horizontal, (d) Static.

On the other hand, PIM is based on the steady-state response of the system. It makes use of the SEA power balance equation:

$$\eta_{ii} = \frac{\Pi_i}{\omega m_i \langle v_i^2 \rangle}, \quad (3.16)$$

where  $\Pi_i$  is the input power in the absence of coupling.

Modal density is also estimated for each plate without connections, using the following formulation [60, 67]:

$$n_i = 4m_i \langle \text{Re}(Y_p) \rangle. \quad (3.17)$$

Here,  $Y_p = \frac{1}{Z_{p_i}}$  is the driving point mobility of the plate.

$Y_p$  is measured from the ratio of the cross-spectral density between the force and the velocity ( $\phi_{fv}$ ) and the auto-spectral density of the force ( $\phi_{ff}$ ) at the input location:  $Y_p = \frac{\phi_{fv}}{\phi_{ff}}$ . The mobility is averaged over three locations on the skin of the plate. For the stiffened plate these locations are near a vertical stiffener, on the intersection between a vertical and a horizontal stiffener and on the skin (away from the stiffeners).

The presence of the impedance head and its attachment elements can introduce a measurement error when the impedance of the plate is not sufficiently high compared to the impedance of the impedance head [67]. A corrected admittance  $Y_c$  is obtained using the admittance of the impedance head  $Y_M$ , which is measured by exciting the impedance head without the driven plate:

$$Y_c = \frac{Y_p}{1 - \frac{Y_p}{Y_M}}. \quad (3.18)$$

In addition, errors associated with shaker-structure interaction and external noise can be minimized by introducing the signal which drives the power amplifier  $s$ , in the computation of  $Y_p$  [67].

$$Y_p = \frac{\phi_{sv}}{\phi_{sf}}. \quad (3.19)$$

Experimental results are then compared, in sections 3.6.2 and 3.6.3, with analytical formulation for simply supported thin flat plates and sandwich panels. The first is given

by  $n_i = \frac{A_i}{2} \sqrt{\frac{\rho_i h_i}{D_i}}$ , where  $A_i$  is the surface of the plate and  $D_i = \frac{E h_i^3}{12(1-\nu^2)}$  is its bending stiffness. The second is given by a general sandwich model [32, 137].

Finally, the power injected in the plate by the excitation force can be expressed in terms of the real part of the plate's driving point impedance  $Re(Z_{p_i})$  and the quadratic velocity at the excitation location  $\langle v_{1e}^2 \rangle$  using:

$$\Pi_i = Re(Z_{p_i}) \langle v_{1e}^2 \rangle. \quad (3.20)$$

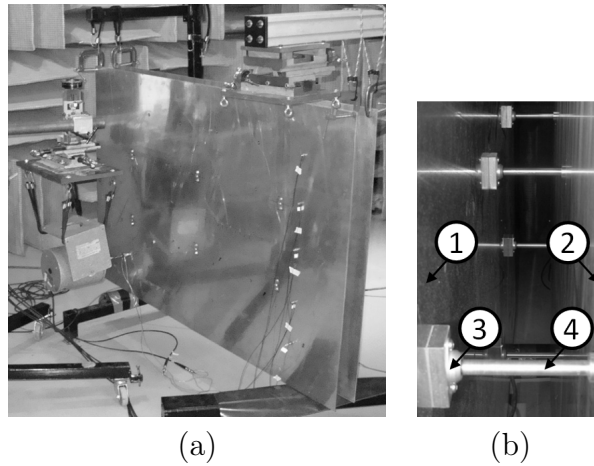


Figure 3.4 Experimental SEA measurements - configuration 1: (a) setup and (b) detail of the connections. 1- plate 1, 2- plate 2, 3- isolator, 4- stud.

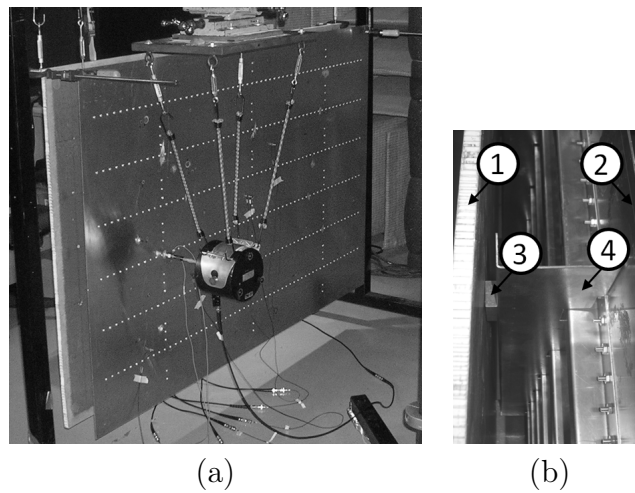


Figure 3.5 Experimental SEA measurements - configuration 2: (a) setup and (b) detail of the connections. 1- trim panel, 2- stiffened panel, 3- rigid connection element, 4- vertical stiffener.

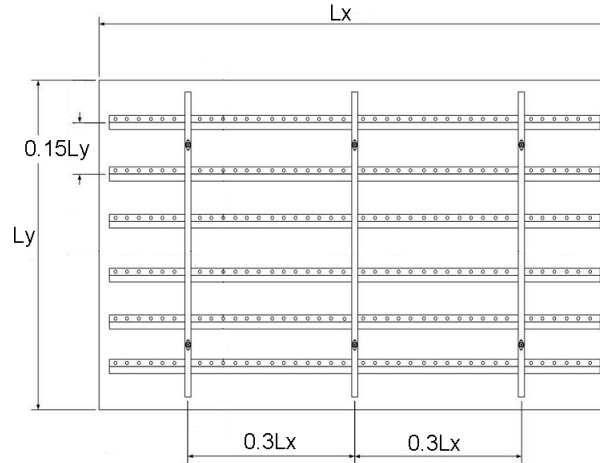


Figure 3.6 Orthogonally stiffened panel: geometrical characteristics and links location.

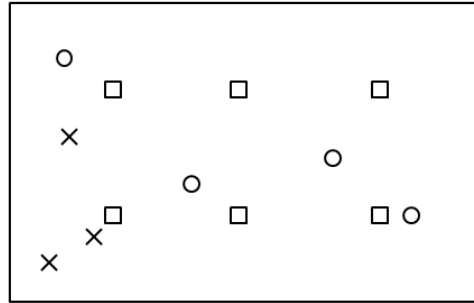


Figure 3.7 Location of isolators ( $\square$ ), accelerometers ( $\circ$ ) and excitation points ( $\times$ ).

## 3.6 Results and discussion

The main experimental results needed to validate the CLF modelling are discussed in this section. First results concern measured static and dynamic stiffness of the isolator. The two double-wall configurations are next analysed. Parameters needed to compute the structural CLF via experimental SEA are then presented. Finally, theoretical and measured CLF are compared and used to predict vibration transmissibility of the systems.

### 3.6.1 Isolator dynamic stiffness

The dynamic stiffness  $k_{21}$  of three samples of the same isolator was measured. Fig. 3.8 shows results for one isolator, tested using the three setups described in section 3.5.1. For the horizontal and impact hammer setups, positioning of the accelerometers  $A_1$ , which are  $180^\circ$  apart, should be verified in order to minimize phase and magnitude difference between the transducers. Impact hammer setup makes use of a 290 g mass and results are averaged

over 5 impacts. The frequency limit of the measurements is linked to the properties of the test bench. Results are shown up to 2000 Hz since a resonance of the horizontal and vertical setups affects the measurement at higher frequencies. For the impact hammer setup, impact force spectrum begins to decrease at frequencies higher than 1000 Hz.

Internal damping of the isolator is also obtained from dynamic tests using Eqn. (3.13). Results are shown in Fig. 3.9. The vertical setup curve shows a low decreasing behaviour in the frequency range from 10 Hz to 2000 Hz. Horizontal setup curve presents a relatively constant value for frequencies higher than 100 Hz. Finally, impact hammer setup curve presents some oscillations and the accuracy of the measurement decreases with frequency.

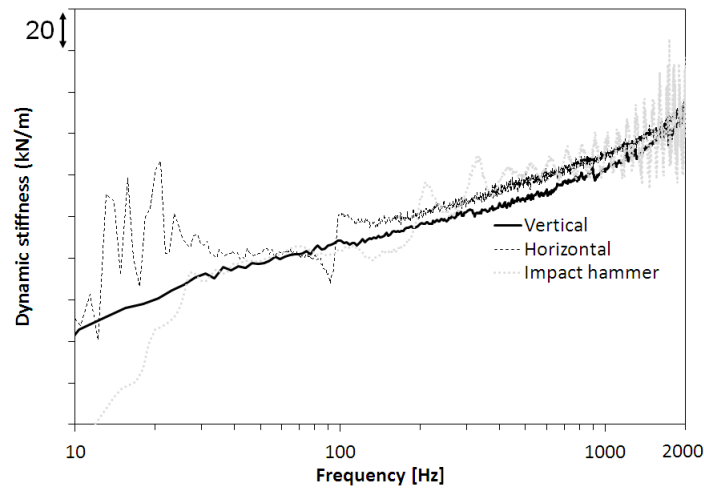


Figure 3.8 Dynamic stiffness of the isolator.

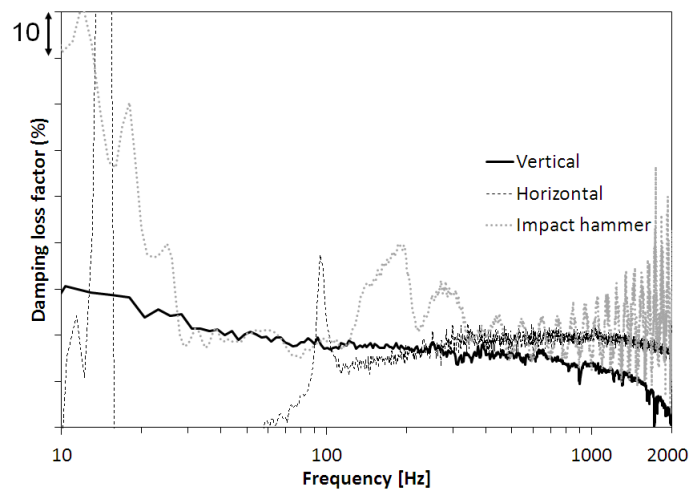


Figure 3.9 Internal damping of the isolator.

Vertical setup is the most adapted for this measurement since it presents less influence of system resonances and better repeatability between samples compared to the two other setups. Moreover, no phase and magnitude adjustments are necessary.

A minor difference in stiffness levels is noticed in Fig. 3.8 between setups. It is mainly related to changes in: (1) the excitation level between measurements and (2) the preload applied to the isolator by the setup, modifying its static stiffness value. The loading of the isolators in the following vibration transmissibility tests (section 3.6.2) are the same as in the vertical setup, with a suspended shaker and no added mass.

Results of the horizontal setup are affected up to 100 Hz by resonances of the L-shaped structure used as rigid backing. Impact hammer tests present, as stated previously, a high frequency limit concerning the impact force spectrum level. In addition, for this last setup, good repeatability between samples is only verified from 40 Hz to 800 Hz. Moreover, for these two setups, adjustments in order to change samples and to achieve good magnitude and phase coherence between accelerometers are time-consuming.

A hysteresis test of the isolator, using setup (d) of Fig. 3.3 is also performed. Results are averaged over 10 cycles at 2 Hz. The stiffness is obtained from the slope of the curve, which is the average of the upper and bottom half cycles [111]. This value is compared with a linear extrapolation at low frequencies of the dynamic stiffness using the vertical setup curve. For this purpose, a linear trend equation in function of the frequency  $f$  is derived from values of the dynamic stiffness averaged between samples, in the frequency range from 200 Hz to 800 Hz. It is then extrapolated from 100 Hz to 10 kHz. The form of the equation is given by:

$$K = a \log_{10}(f) + k_0. \quad (3.21)$$

Here,  $a$  is a constant and  $K$  tends to the static value  $k_0$  when  $\log_{10}(f) \rightarrow 0$ .

In addition, a traction-compression test is performed using the same setup. For this test, the displacement is increased with time at a slow rate and the force applied to the sample is monitored.

Static stiffness resulting from extrapolation of dynamic tests and static tests are in good agreement with hysteresis tests, with differences of 9% and 6% respectively. Moreover, it is observed during static tests that the force applied to the sample decreases as a consequence of rearrangements of the elastomer chains, resulting in a decrease of the stiffness with time. This phenomenon is known as relaxation and it is typical of elastomers.

Finally, the DLF of the isolator is determined from the hysteresis curve using Eqn. (3.14). Moreover, an estimation of the DLF from the decay of the time-response of the accelerometers in the impact hammer setup is also calculated. It is given by Eqn. (3.22) assuming an exponential decay with time:

$$\eta_m = 2 \frac{\delta}{\sqrt{4\pi^2 + \delta^2}}, \quad (3.22)$$

where  $\delta = \ln \left( \frac{a(t)}{a(t+T)} \right)$  and  $a(t)$  is the acceleration signal of period  $T$ .

In order to compare dynamic and hysteresis DLF results, the value at 2 Hz is estimated from the dynamic results. A trend equation is computed between 100 Hz and 1000 Hz and a value is extrapolated at 2 Hz. Differences are of the order of 15%. Moreover, DLF obtained from decay of the time-response are in agreement with hysteresis results, with differences of 5%.

For SEA simulations, Eqn. (3.5) represents the stiffness of the isolator, with  $K$  given by the dynamic stiffness trend equation, Eqn. (3.21) and  $\eta_m$  given by hysteresis results. The latter is assumed constant since the low decreasing behaviour observed in the DLF dynamic curve leads to negligible variation in the computed CLF.

It is important to note that values of  $K^*$  at frequencies higher than 2000 Hz could not be measured due to limits of the test bench. However, the linear trend in function of the logarithm of the frequency is assumed in 100 Hz to 10 kHz frequency range. The validity of this assumption and the CLF obtained from the mass-spring-mass modelling of the isolators will be verified by experimental SEA tests.

### 3.6.2 Results in configuration 1

In this section, CLF of two plates connected via vibration isolators are estimated using experimental SEA, Eqn. (3.2). Results are compared with theoretical CLF using the four-pole approach, Eqn. (3.8). The tested system is represented in Fig. 3.4a. The theoretical CLF are then used to calculate the vibration transmissibility of the system and compared with measurements in the 100 Hz to 10 kHz frequency range. All results are averaged in one-third octave bands.

In order to obtain the experimental CLF, all parameters of Eqn. (3.2) should be determined. The DLF of the plates are measured using DRM and PIM methods and results are shown in Fig. 3.10. The same trend is obtained with the two methods, with PIM results a little higher than DRM ones, except at low frequencies and in the critical frequency region of the plates, where radiation damping dominates (around 3750 Hz for plate 1 and 6000 Hz for plate 2). DRM results are more sensitive to radiation damping, considering it gives a higher peak at the critical frequency region compared to PIM results. The choice

between methods is still an open issue, but in order to minimize interference of the radiation coupling, which is not modelled, results from the PIM are used in experimental CLF computation.

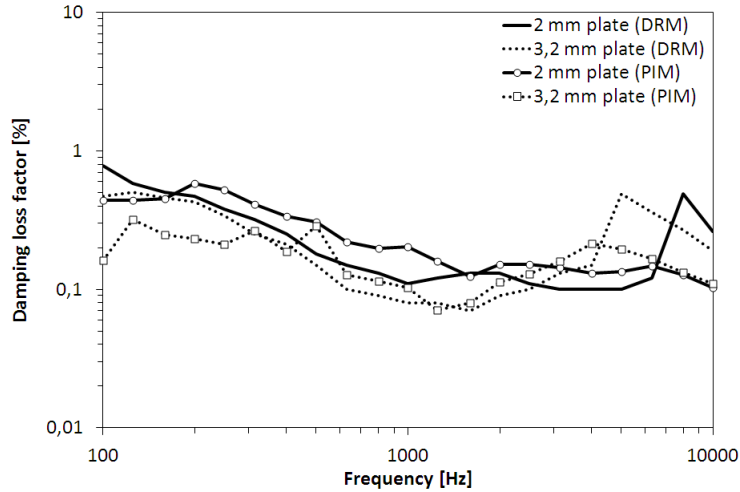


Figure 3.10 Damping loss factor of the plates (configuration 1).

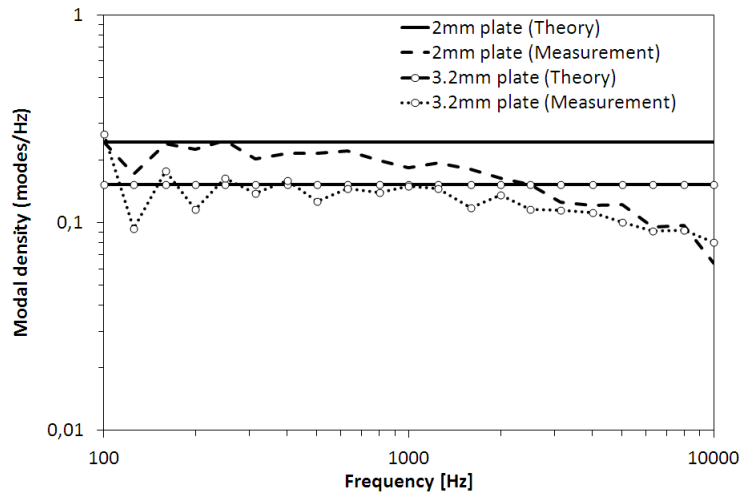


Figure 3.11 Modal densities of the plates.

The modal densities of the plates are estimated using drive point mobility measurements [60, 67] and compared with theoretical values according to section 3.5.2. Results are plotted in Fig. 3.11. Good agreement is observed in the low and mid frequency ranges. At high frequencies, the power injected to the structure is low, and fewer modes are excited. Theoretical values of modal densities are used in CLF computation since measurement errors are higher at high frequencies. Moreover, the number of modes of the 3.2 mm plate for frequencies lower than 150 Hz is less than 5, which is the minimum commonly considered for the application of SEA.

Finally, when the system is assembled, the energy of each plate is derived from measured space-averaged quadratic velocities, as explained in section 3.4.1 and the input power is obtained from Eqn. (3.20).

### Coupling loss factor in configuration 1

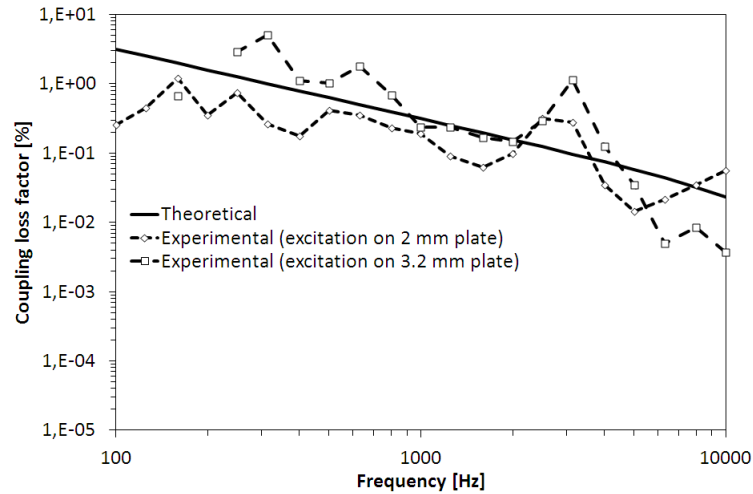


Figure 3.12 Coupling loss factors - rigid coupling (configuration 1).

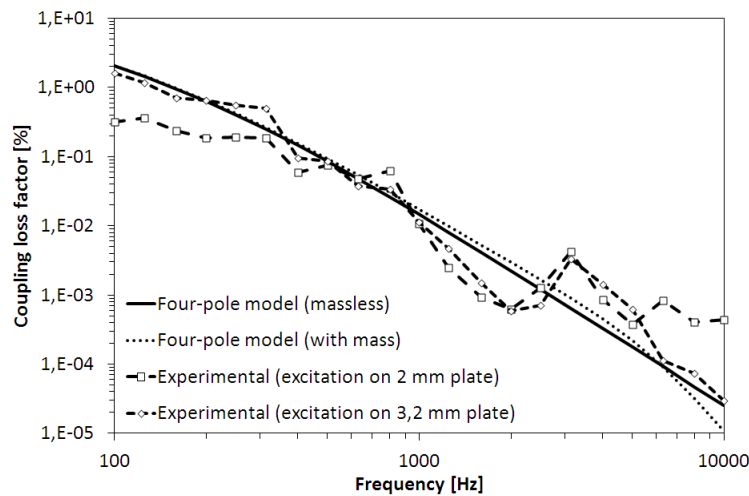


Figure 3.13 Coupling loss factors - soft coupling (configuration 1).

The theoretical CLF for the rigid coupling case is given by Eqn. (3.8), assuming  $K^* = \infty$  in Eqn. (3.6). The experimental CLF values are given by Eqn. (3.2). In order to evaluate system reciprocity, the CLF are measured considering the excitation located on each plate. Results are shown in Fig. 3.12. It is observed that the simple theoretical model captures the trend of the coupling between plates. In addition, reciprocity is moderately verified. Moreover, at low frequencies some values are missing for the case where excitation is

located on the 3.2 mm plate. This happens since coupling is high and energy levels of the plates are very similar, resulting in negative CLF.

Results for the soft coupling case are shown in Fig. 3.13. Here, two theoretical cases are considered: isolators with a total mass of 5.6 g and massless isolators. Since the mass element has an influence mainly at high frequencies and the two cases give very similar results, only the stiffness element (massless isolators) will be considered in the modelling.

Reciprocity is well verified experimentally, but higher variations are observed around the critical frequencies of the plates (3750 Hz and 6000 Hz). This is due to the influence of radiation damping, which is not accounted for in the modelling. Additionally, when excitation is located on the 2 mm plate, a peak at the critical frequency region of the 3.2 mm plate is also observed. Indeed, due to its lighter weight and lower stiffness, the thinner plate is more subjected to radiation coupling from the thicker plate.

The four-pole approach with a linear assumption for the dynamic stiffness well predicts the CLF through isolators. A better agreement around their critical frequencies can be obtained by considering the radiation coupling between plates and by separating the radiation component from the internal loss factors.

It is interesting to evaluate the sensitivity of the theoretical CLF to errors on stiffness measurements. These errors are linked to the static stiffness value, resulting in a vertical shift of the dynamic stiffness curve, Eqn. (3.21). A 10% variation of the static stiffness leads to a maximum deviation of 5% in the theoretical CLF. Moreover, it should be noted that damping measurements are often subjected to an accuracy of 20% or higher [53], which is directly propagated to the experimental CLF.

### **Vibration transmissibility in configuration 1**

Theoretical and measured vibration transmissibilities are compared in Fig. 3.14 and 3.15 for rigid and soft couplings, respectively. The first is calculated from SEA Eqn. (3.1), using the CLF obtained with the four-pole approach. The latter is obtained from acceleration measurements averaged over the plates surface. The associated 95% confidence interval (CI) is also shown in grey. It is calculated using  $CI = 1.96 * SEM$ , where 1.96 is the coefficient for a 95% probability assuming a normal distribution of the measured vibration transmissibility, and  $SEM = \frac{\sigma}{\sqrt{n}}$  is the standard error of the mean, obtained from the ratio between the standard deviation ( $\sigma$ ) and the square root of the number of samples ( $n$ ).

Results for the rigid and soft cases show that the four-pole approach captures well the physical phenomena of structural transmission between the plates, except around their critical frequencies where radiation transmission dominates. SEA predictions are good even for a high coupling condition, as in the rigid case. For this coupling configuration, CLF values are higher than DLF values.

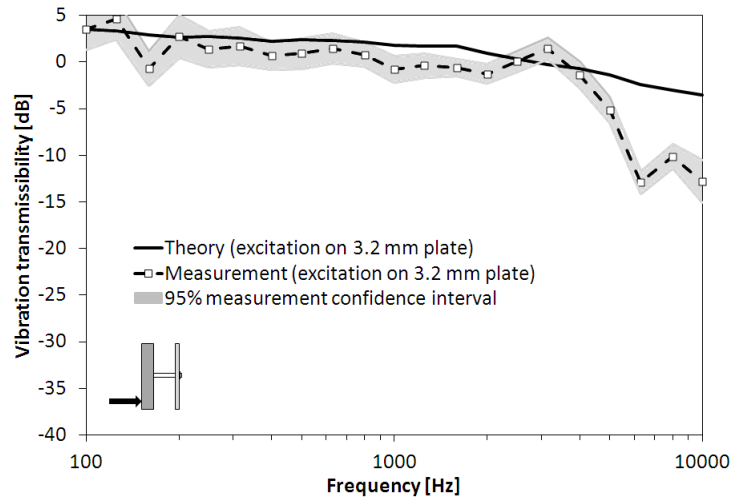


Figure 3.14 Vibration transmissibility - rigid configuration, excitation on 3.2 mm plate.

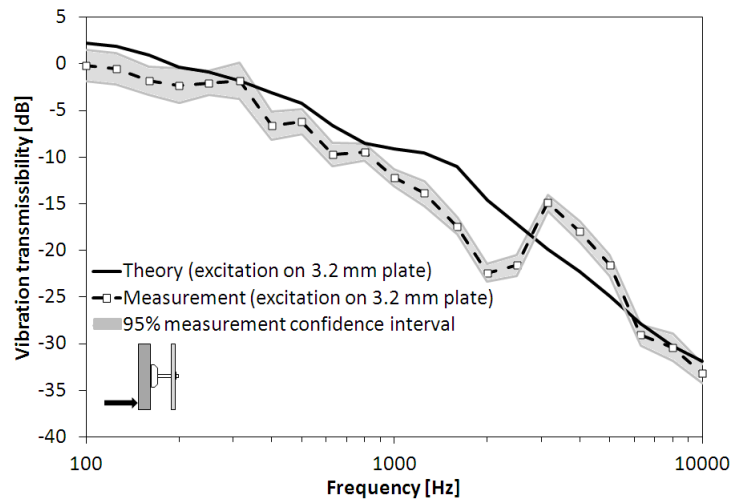


Figure 3.15 Vibration transmissibility - Soft configuration, excitation on 3.2 mm plate.

### 3.6.3 Results in configuration 2

In this section, configuration 2 is considered. It is composed of a stiffened and a sandwich panel, a typical skin and trim panels of an aircraft, respectively (the two are however flat).

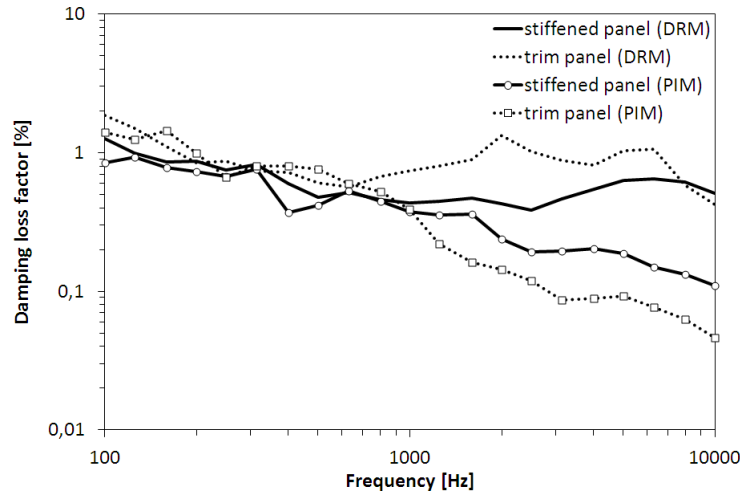


Figure 3.16 Damping loss factor of the panels (configuration 2).

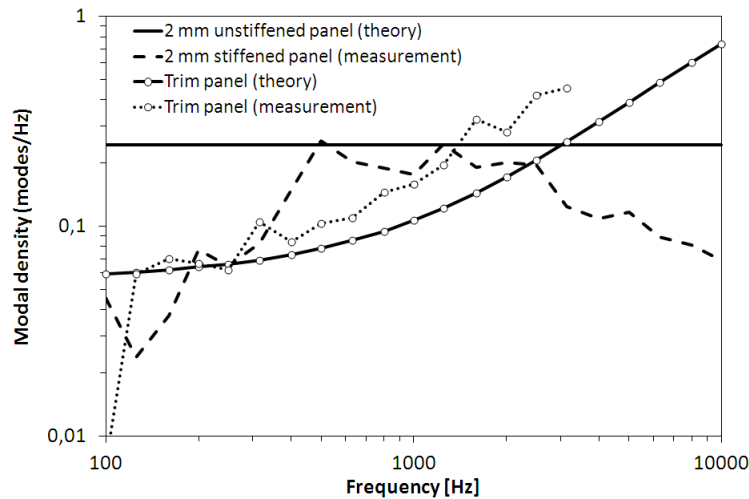


Figure 3.17 Modal density of the panels.

DLF results using the decay rate and the power input methods are shown in Fig. 3.16. Contrary to the aluminium plates case, the two methods only agree well at low frequencies, notably for the trim panel. In mid and high frequencies, since the damping of the panels are relatively higher than those of configuration 1, the averaged steady-state velocity response is dominated by the accelerometers close to the the excitation point, mainly, the accelerometer of the impedance head. This affects the accuracy of the PIM. However, excluding the input point results in a poorer averaging due to a small number of remaining acceleration points. For this reason, DRM results are considered in the analysis. Moreover, as observed in the case of configuration 1, the DLF of the panels are affected by radiation damping at their critical frequency regions, around 6000 Hz and 2500 Hz for the stiffened and trim panels, respectively.

Fig. 3.17 shows the modal densities of the panels studied. Theoretical values correspond to an unstiffened plate of same thickness of the stiffened one. For the stiffened panel, an influence of the stiffeners is observed, reducing the modal density at low frequency. For frequencies higher than 400 Hz the half wavelength of the bending waves are less than the horizontal stiffeners spacing and the modal density reaches that of an unstiffened plate. For the trim panel, a general sandwich theory is used as described in section 3.5.2. Compared with measurements, prediction gives lower values in the mid-frequency range. This is traced to the assumption of an equivalent bending stiffness for the trim panel in the estimation of the theoretical modal density. Differences at high frequencies are observed as for configuration 1. They are traced to a difficulty in injecting power to the system in this frequency region, notably for the trim panel (results are shown up to 3150 Hz). Indeed, due to its high damping and low stiffness, less modes are excited. Moreover, the number of modes in a frequency band is at least 5 for frequencies higher than 200 Hz for the stiffened panel and 315 Hz for the trim panel.

### **Coupling loss factor in configuration 2**

Fig. 3.18 and 3.19 show the CLF of the plates for rigid and soft couplings, respectively. It should be reminded that isolators are connected to the vertical stiffeners of the panel instead of using studs as in configuration 1. Therefore, the influence of the stiffener's dynamic stiffness should be evaluated. An equivalent rigid connector is used in the rigid coupling case (Fig. 3.5b). As a first approximation, stiffeners are assumed rigid for both coupling cases. An addition curve is also shown for the rigid coupling when stiffeners are modelled having a finite constant dynamic stiffness of  $K^* = 500$  kN/m (this value is obtained from static FEM modelling of the stiffener). For the soft coupling, stiffeners and isolators are connected in series, however since the dynamic stiffness of the isolator is much lower than the assumed finite stiffness of the stiffeners, the latter can be considered rigid.

The rigid coupling configuration is in the limit of validity of SEA equations for the following reasons: (1) the reciprocity of coupling is not verified considering that different results are obtained when the excitation is located in each panel (mainly due to the cited difficulties in exciting the trim panel) and (2) negative CLF is obtained at low frequencies when the excitation is located on the stiffened panel (from 100 Hz to 400 Hz). In addition, results for the excitation located on the trim panel at frequencies higher than 3000 Hz are omitted since they are not accurate, as observed in Fig. 3.17. On the other hand, experimental CLF agree well with theory at mid frequencies, when the excitation is located on the stiffened panel, for stiffeners modelled as rigid elements. At high frequencies, good agreement is

obtained for stiffeners modelled as having a finite dynamic stiffness. These results show that the dynamic behaviour of stiffeners should also be included in the modelling.

Contrary to the rigid coupling, the soft coupling configuration (Fig. 3.19) shows good reciprocity at low and mid frequencies. Moreover, at high frequencies, theoretical and experimental values show similar trends when the excitation is located on the stiffened panel. It should be reminded that experimental results for the excitation located on the trim panel are not shown above 3000 Hz. Therefore, for high frequencies analysis, only the excitation on the stiffened panel will be considered. Experimental CLF is higher than the theoretical one at the critical region of the panels due to the acoustic radiation contribution. Massless model gives a better prediction and the mass of isolator has a higher influence at high frequencies compared to configuration 1.

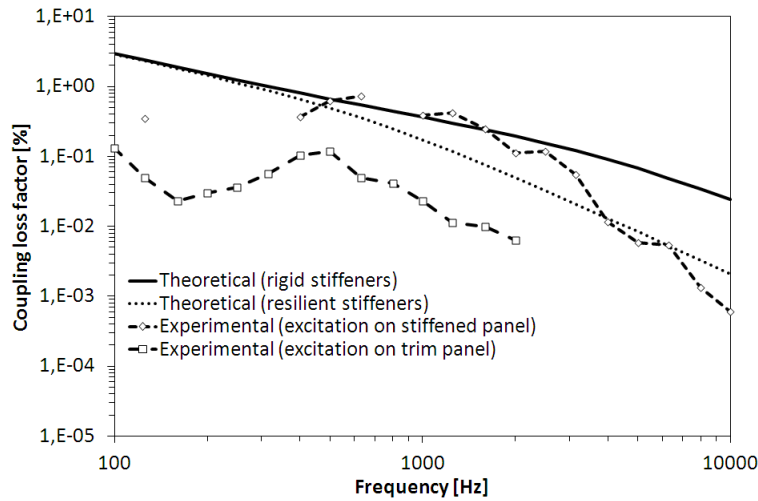


Figure 3.18 Coupling loss factors - rigid coupling (configuration 2).

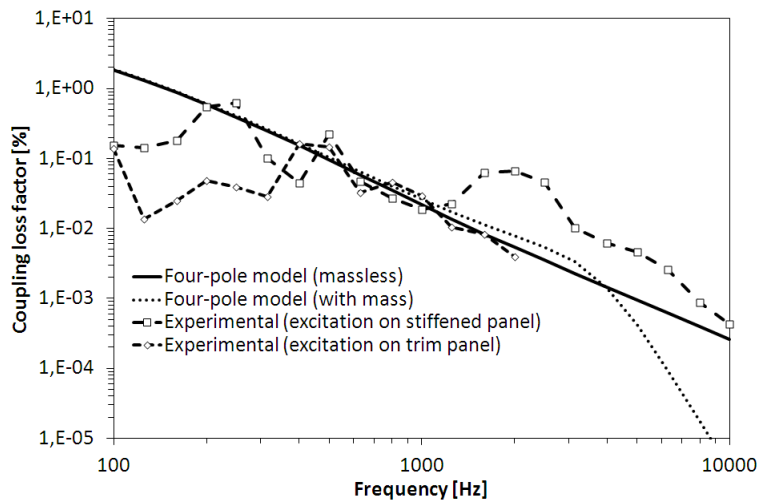


Figure 3.19 Coupling loss factors - soft coupling (configuration 2).

### Vibration transmissibility in configuration 2

Vibration transmissibilities for the rigid and soft couplings are shown in Fig. 3.20 and Fig. 3.21, respectively. The excitation is located on the stiffened panel. The associated 95% confidence interval, as defined in section 3.6.2 is also shown in grey. A high uncertainty level is obtained for the rigid coupling and for the soft coupling at low frequencies since SEA assumption of low coupling is not satisfied. In addition, at low frequencies the average response is not representative since vibration is governed by only a few modes of the panels. This interval can be improved if a higher number of measurements ( $n$ ) is performed.

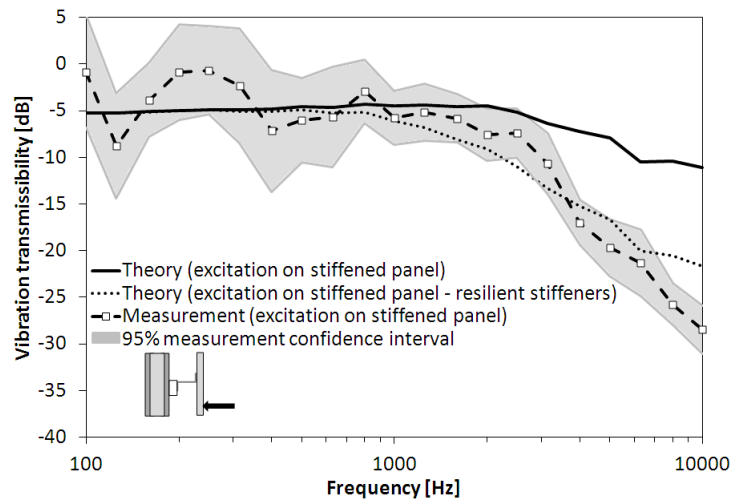


Figure 3.20 Vibration transmissibility - rigid configuration, excitation on stiffened panel.

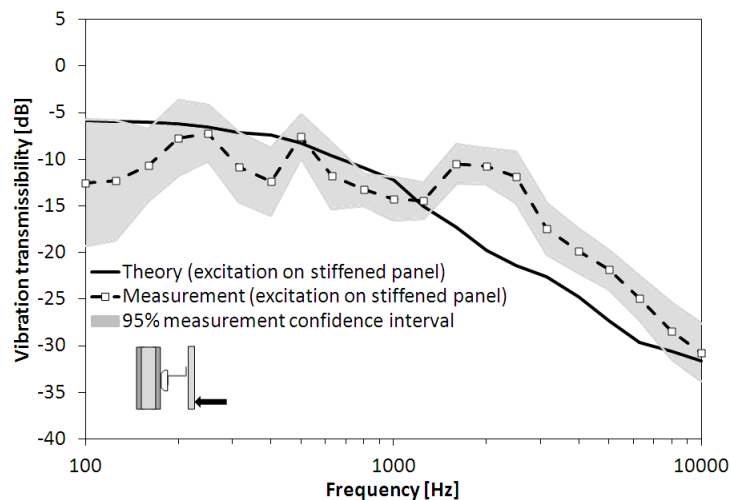


Figure 3.21 Vibration transmissibility - Soft configuration, excitation on stiffened panel.

Good agreement is obtained for the rigid coupling configuration at low and mid frequencies when stiffeners are modelled as rigid. At high frequencies a better agreement is obtained

considering stiffeners of finite stiffness, such as discussed in section 3.6.3. This latter result reinforces the need for modelling the dynamic behaviour of stiffeners.

The model predicts well the vibration transmissibility of soft coupling, with differences observed at the critical region of the panels as in configuration 1.

## 3.7 Conclusion

The main contributions of this paper are: (1) the determination of the most adapted setup for the measurement of dynamic stiffness and damping of typical aircraft shock mounts (vibration isolators) as well as its associated frequency limits, (2) the validation of the coupling loss factor between two plates connected via vibration isolators by modelling the coupling element using a four-pole approach.

Comparison of measured and SEA predicted coupling loss factor and vibration transmissibility shows good agreement for the system composed of two isotropic plates rigidly coupled. For the system composed of a stiffened isotropic panel and a sandwich panel, the agreement is good considering the stiffeners as rigid at mid frequencies and as resilient at high frequencies. This latter results shows the importance of correctly modelling the dynamic behaviour of stiffeners. The soft coupling modelling shows a better agreement with experiments when massless connections are assumed. For this type of coupling, theory agrees well with measurements, except at the critical region of the plates, where acoustic radiation dominates. This happens since only structural transmission is considered in the model. A better agreement can be obtained by considering the radiation coupling between panels and by separating the radiation component from the internal loss factors. Moreover, measured modal densities are lower than theoretical ones at high frequencies due to an experimental limitation in injecting sufficient power in this frequency region, notably for the sandwich panel.

This work demonstrates the robustness of the simple four-pole modelling even for the complex configuration of isolators attached to stiffeners. However, it clearly shows the importance of (1) correctly determining the dynamic stiffness, (2) the damping loss factor of the plates, since uncertainties are directly propagated to the coupling loss factor and notably (3) the effect of radiation damping. Future work will in particular concentrate on the latter.

## **Acknowledgements**

Rémi Oddo, Maxime Bolduc and Patrick Levesque, from University of Sherbrooke, are acknowledged for their technical assistance. Lord Corporation is also acknowledged for contributing materials for experiments.



# CHAPTER 4

## SOUND TRANSMISSION THROUGH UNCOU- PLED AIRCRAFT DOUBLE-WALLS

### 4.1 Chapter introduction

A description of the airborne sound transmission through structurally-decoupled double-walls under acoustic excitation is described in this chapter. The assessment of the sound transmission loss using fast modelling approaches as the Transfer Matrix Method (TMM) and Statistical Energy Analysis (SEA) is discussed. Theory is then compared to measurements on double-walls with two degrees of complexity: (1) aircraft double-walls composed of aluminium or laminate composite stiffened skin panels and a sandwich composite trim panel and (2) academic double-walls composed of unstiffened aluminium panels. Description of the models and analysis on double-walls of the first type are developed in the paper submitted to *Acta Acustica united with Acustica*. Results for double-walls of the second type are presented at the end of the chapter in order to identify discrepancies due to complex elements of double-walls of the first type (stiffeners and sandwich trim panel). Information on the paper and its abstract are given hereafter in French. The SEA model is further developed in chapter 5 in order to include structure-borne transmission via links. In addition, this model is modified to account for random structural excitation (uncorrelated point forces).

Dans ce chapitre, l'article intitulé "*On the prediction of sound transmission through aircraft double-walls using statistical energy analysis and transfer matrix method*" est présenté. Il a été soumis au journal *Acta Acustica united with Acustica*. Une extension de l'analyse développée dans cet article est présentée en complément de ce chapitre pour des structures du type double-parois académiques.

#### **Auteurs et affiliation :**

B. Campolina : Airbus Operations SAS, Acoustic and Environmental Department, Route de Bayonne, 316 F31060 Toulouse Cedex 09, France.

N. Atalla : GAUS, Department of Mechanical Engineering, Université de Sherbrooke, Sherbrooke, Quebec, Canada J1K 2R1.

N. Dauchez : LISMMA, Institut Supérieur de Mécanique de Paris, 3, rue Fernand Hainaut, 93407 Saint-Ouen, France.

**Date de soumission :** 03/04/12.

**Revue :** Acta Acustica united with Acustica.

**Titre français :** Prédiction de la transmission sonore de double-parois d'avion par l'analyse statistique énergétique et par la méthode des matrices de transfert.

## 4.2 Résumé de l'article soumis au journal Acta Acustica united with Acustica

Cette étude compare deux méthodes de prédiction de la perte par transmission (TL) de double-parois aéronautiques. Ce sont la méthode de matrices de transfert (TMM) et l'analyse statistique énergétique (SEA). La double-paroi étudiée est composée de : (1) une plaque métallique ou composite dont la zone de coïncidence est autour de 6 kHz et 4 kHz respectivement ; (2) une cavité interne partiellement remplie avec un matériau fibreux et (3) un panneau d'habillage de type sandwich dont la zone de coïncidence est autour de 2500 Hz. La structure est excitée par un champ diffus dans la gamme de fréquence entre 100 Hz et 10 kHz. Des mesures de facteur de perte par amortissement, de densité modale et d'efficacité de rayonnement sont effectuées pour tous les panneaux afin de valider les paramètres d'entrée des modèles. Les deux approches théoriques donnent des résultats similaires de TL, cependant les résultats théoriques surestiment la mesure d'environ 7 dB. Les limites des modèles sont reliées à la complexité de la structure, en particulier à l'influence des raidisseurs (qui ne sont pas modélisés), à la détermination du facteur de perte par amortissement des panneaux et à la prédiction du rayonnement du panneau sandwich (trim).

Mots clé : Méthode des matrices de transfert, Analyse statistique énergétique, efficacité de rayonnement.

**Paper submitted to the Acta Acustica united with Acustica journal**

## On the prediction of sound transmission through aircraft double-walls using statistical energy analysis and transfer matrix method

### Abstract

This paper compares two methods for quick assessment of the transmission loss (TL) of double-walls in aircraft applications: the Transfer Matrix Method (TMM) and Statistical Energy Analysis (SEA). The studied system is composed of: (1) a metallic or a composite stiffened skin panel, with critical frequencies around 6 kHz and 4 kHz, respectively; (2) an air gap partially filled with a fibrous layer and (3) a sandwich trim panel with critical frequency around 2500 Hz. The structure is subjected to a diffuse acoustic field in the frequency range from 100 Hz to 10 kHz. In order to validate input parameters of the models, measurements of damping loss factor, modal density and radiation efficiency are performed for all the panels. Both approaches show similar transmission loss results, however an overestimation of about 7 dB in the frequency range from 400 Hz up to 5 kHz is observed when compared to tests. Modelling limitations are traced to the complexity of the structure, particularly the influence of stiffeners, which are not modelled, the assessment of panels' damping loss factors and the prediction of the sandwich trim panel's radiation.

**keywords:** Transfer matrix method, Statistical energy analysis, Transmission loss, Radiation efficiency.

### 4.3 Paper submitted to Acta Acustica United with Acustica Journal - Introduction

Lightweight double-wall structures filled with air and absorbent materials have been extensively studied considering their wide range of industrial applications, such as building, automotive, railway and aircraft. A summary of the methods used to predict sound transmission through these structures is given in [140]. In mid to high frequencies, these methods are an alternative to finite element modelling, which is time-consuming and therefore not suitable for optimisation studies. This paper focuses on the transmission loss of lightweight structures representative of an aircraft fuselage, as shown in Fig. 4.1. The first panel (skin panel) is composed of an isotropic (aluminium) or a laminate composite (fibre reinforced plastic) material. The second one (receiver panel) is a honeycomb sandwich composite. A layer of sound absorbing material (glasswool) is lined with the skin panel.

Finally, the analysis is performed considering a diffuse acoustic field (DAF) excitation in the frequency range from 100 Hz to 10 kHz.

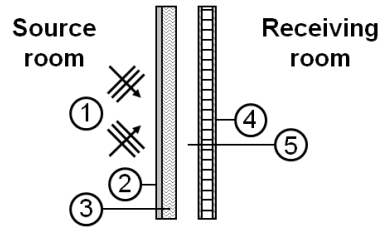


Figure 4.1 Double-wall structure: 1-diffuse field excitation, 2-source panel, 3-porous layer, 4-receiving sandwich panel, 5-air gap.

This paper aims at validating experimentally two approaches for predicting the sound transmission that are suitable to the pre-design phase of conception: Transfer Matrix Method (TMM) and Statistical Energy Analysis (SEA). The first one is based on the plane wave propagation through layers of materials represented by a transfer matrix linking velocities and stresses at their boundaries [5, 47]. The second method represents the structure through its damping and coupling loss factors, modal density and energy level [3, 38, 53, 141]. Experimental and theoretical methods for the determination of panel's properties serving as input to the models are also discussed.

This paper is organised in four sections, following the introduction. Section 2 describes theoretical concepts of the transfer matrix method and the statistical energy analysis applied to the sound transmission of single and double panels. Section 3 presents experimental determination of panel's properties used in the models and the transmission loss indicator. Section 4 analyses SEA parameters and TL results. In addition, experimental and theoretical limits are highlighted.

## 4.4 Theory

In this section, a brief description of the transfer matrix method and of statistical energy analysis applied to the sound transmission of single and double-walls is given. Stiffeners are not accounted for in the modelling. The response of the structure is studied under a diffuse acoustic field excitation.

### 4.4.1 Transfer matrix method (TMM)

The sound transmission through layers of solids, porous and fluids can be modelled using the transfer matrix method [5, 47]. The layers are considered flat and of infinite extent

but corrections of the acoustic radiation can be applied to account for the finite size of the panels, [48, 49]. Fig. 4.2 represents the layers of the double-wall studied structure, immersed in air. Incident and reflected waves, with amplitudes I and R, are represented at excitation side (i). Transmitted wave, with amplitude T, is represented at receiver side (o).

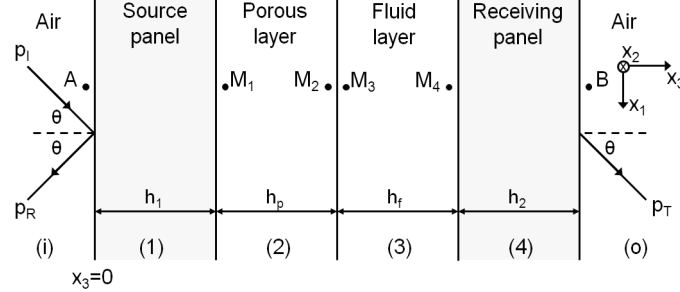


Figure 4.2 Transfer matrix representation of the transmission through the studied double-wall system.

The transmission within a layer is given by the following equation:

$$V^L(M_i) = [T^L] V^L(M_{i+1}), \quad (4.1)$$

where  $V^L$  is the vector of stresses and velocities and  $[T^L]$  the transfer matrix of layer  $L$ .

For the fluid layer,  $V^f = [p, v_3^f]^t$  is the transpose vector of the acoustical pressure  $p$  and the  $x_3$  component of the fluid velocity,  $v_3^f$ . These variables are function of  $k_3$ , the  $x_3$  component of the wavenumber in the fluid medium. It is defined as  $k_3 = \sqrt{k_0^2 - k_1^2}$ . Defining  $c_0$  and  $\eta_0$  the speed of sound and the loss factor of the fluid medium, the acoustic wavenumber is given by:  $k_0 = \frac{\omega}{c_0} (1 + j\eta_0)$ .  $k_1$  is the  $x_1$  component of the wavenumber in the fluid medium. In the presented results,  $\rho_0 = 1.213 \text{ kg.m}^{-3}$  and  $c_0 = 342.2 \text{ m.s}^{-1}$  are the density and the speed of sound in the fluid, respectively.

The tested porous layer, being a fibrous material of low elastic modulus (below 5 kPa) and low density, is modelled using the limp approach [5, 99–101]. Therefore, the same relations derived for the fluid are valid for the porous when  $\rho_0$  and  $k_0$  are modified to effective values  $\rho_l$  and  $k_l = \omega \sqrt{\frac{\rho_l}{K_l}}$ , with  $\rho_l$  representing the limp porous effective density and  $K_l$  the equivalent compressibility modulus [5]. The expression for  $\rho_l$  is given by:

$$\rho_l = \phi \frac{\rho_t \rho_f / \phi - \rho_0^2}{\rho_t + \rho_f / \phi - 2\rho_0}. \quad (4.2)$$

In this equation  $\phi$  is the porosity of the medium,  $\rho_t = \rho_1 + \phi\rho_0$  is the total apparent mass of the fluid with  $\rho_1$  being the density of the porous material.  $\rho_f$ , the effective density of the fluid phase of the “rigid frame equivalent fluid” model.

For a thin elastic layer,  $V^s = [p \ v_3^s]^t$  and  $Z_s(\omega) v_3^s = p(i) - p(M_1)$ . Here,  $Z_s$  is the panel’s impedance. In the case of a thin plate in bending, it is given by:

$$Z_s(\omega) = j\omega\rho_i h_i \left( 1 - \frac{k_0^4}{k_b^4} \sin^4(\theta) \right), \quad (4.3)$$

where  $\rho_i$  and  $h_i$  are the density and thickness of the panel and  $k_b = \sqrt{\omega} \sqrt[4]{\frac{\rho_i h_i}{D_i}}$ , its bending wave number.  $D_i$  is the panel’s bending stiffness, given by:  $D_i = \frac{Eh_i^3}{12(1-\nu^2)}$ , where  $E$  and  $\nu$  are the panel’s Young’s modulus and Poisson’s ratio.

For a laminate or a sandwich composite material, a general laminate model (GLM) is used [30, 32, 33]. It uses a hybrid displacement interface forces vector to define the dispersion equation. The obtained wavenumber is then inserted into Eq. (4.3) in order to compute the panel’s impedance and resulting transfer matrix. The displacement in each layer uses five variables accounting for in-plane, bending and shear deformations. This model has been shown to be valid for both composite panels (thin laminates) and sandwich panels (shear core panels) with thin or thick skins (including non-symmetric and composite skins) [32, 33]. Its main limitation, as the majority of classical sandwich models, is its inability of representing symmetric motions of the sandwich panels. However, this state of deformation is not important in the studied panels (mainly important for thick and flexible cores).

The transmission loss is then given by  $TL = -10 \log(\bar{\tau})$ , where  $\bar{\tau}$  is the power transmission coefficient averaged over all possible angles of incidence. It is given by the following equation:

$$\bar{\tau} = \frac{\int_0^{\theta_L} \tau(\theta) \sin(\theta) \cos(\theta) d\theta}{\int_0^{\theta_L} \sin(\theta) \cos(\theta) d\theta}, \quad (4.4)$$

where  $\theta_L$  is the maximum incident angle, assumed  $78^\circ$  (field incidence) and  $\tau(\theta)$  is obtained from the ratio of the amplitudes of the incident and transmitted waves, from each side of the multilayer.

#### 4.4.2 Statistical energy analysis (SEA)

Another method for modelling the sound transmission through a multilayer structure is Statistical Energy Analysis [3, 38, 53, 141]. In this approach, the whole system is divided

into subsystems, which are groups of similar resonant modes. They can receive, store, dissipate and transmit energy. The vibroacoustic state is expressed in terms of vibrational energies of individual subsystems, the applied excitations are expressed in terms of input powers and the coupling between subsystems is expressed in terms of energy flow.

In SEA, sound transmission through a single-wall system is classically modelled using 3 subsystems [3, 38, 53]. A source and a receiver cavity, separated by a panel. Each subsystem  $i$  is represented by a damping loss factor (DLF)  $\eta_{ii}$ , a modal density  $n_i$ , an energy level  $E_i$  and an input power  $\Pi_i$ . In addition, coupling between subsystems  $i$  and  $j$  is represented by a coupling loss factor (CLF)  $\eta_{ij}$ . It is linked to  $\eta_{ji}$  by the following reciprocity relation:

$$\eta_{ij}n_i = \eta_{ji}n_j. \quad (4.5)$$

For a double-wall system, the sound transmission is modelled using 5 interconnected subsystems [141], as is shown in Fig. 4.3. A source, an inner and a receiver cavity are modelled. They are represented by subsystems 1, 3 and 5. The skin and trim panels, regrouping bending modes, are represented by subsystems 2 and 4. The resulting system of equations is:

$$\begin{bmatrix} \eta_{11} + \sum_{i \neq 1} \eta_{1i} & -\eta_{21} & -\eta_{31} & -\eta_{41} & -\eta_{51} \\ -\eta_{12} & \eta_{22} + \sum_{i \neq 2} \eta_{2i} & -\eta_{32} & -\eta_{42} & -\eta_{52} \\ -\eta_{13} & -\eta_{23} & \eta_{33} + \sum_{i \neq 3} \eta_{3i} & -\eta_{43} & -\eta_{53} \\ -\eta_{14} & -\eta_{24} & -\eta_{34} & \eta_{44} + \sum_{i \neq 4} \eta_{4i} & -\eta_{54} \\ -\eta_{15} & -\eta_{25} & -\eta_{35} & -\eta_{45} & \eta_{55} + \sum_{i \neq 5} \eta_{5i} \end{bmatrix} \begin{bmatrix} E_1 \\ E_2 \\ E_3 \\ E_4 \\ E_5 \end{bmatrix} = \begin{bmatrix} \frac{\Pi_1}{\omega} \\ 0 \\ 0 \\ 0 \\ 0 \end{bmatrix}. \quad (4.6)$$

The modal densities of the cavities ( $n_1$ ,  $n_3$  and  $n_5$ ) are calculated using the high frequency approximation of room acoustics [142], where  $V_i$  is the volume of the cavity:

$$n_i(\omega) = \frac{V_i \omega^2}{2\pi^2 c_0^3}. \quad (4.7)$$

The damping loss factor of the cavities ( $\eta_{11}$ ,  $\eta_{33}$  and  $\eta_{55}$ ) are given by [141]:

$$\eta_{ii} = \frac{\alpha A_i c_0}{4\omega V_i}. \quad (4.8)$$

Here,  $\alpha$  and  $A_i$  are the absorption coefficient of the cavity, assumed 0.01, and its total surface, respectively. The properties and dimensions of the source and receiving rooms are arbitrary, however, they are chosen so that  $n_{cav}$  and  $\eta_{ii,cav}$  are within the SEA limits of application.

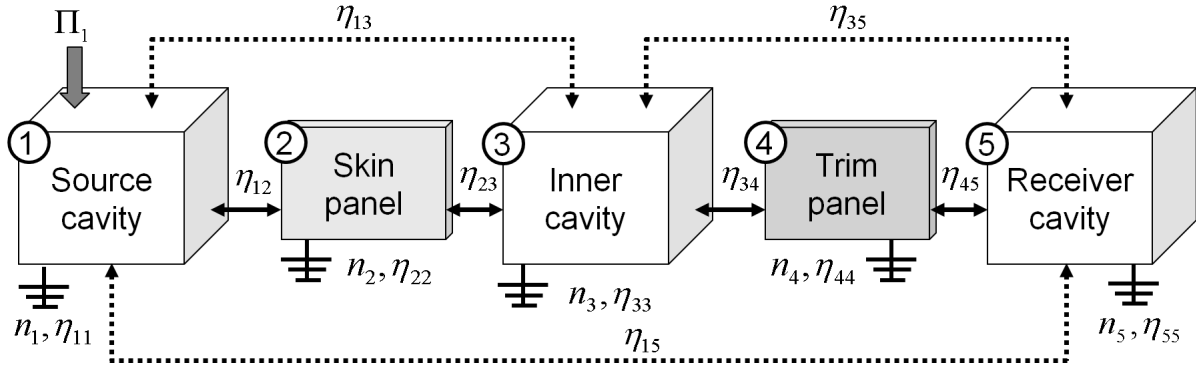


Figure 4.3 SEA representation of the double wall system.

The coupling loss factor between cavities ( $\eta_{13}$  and  $\eta_{35}$ ) are calculated by using the mass-law transmission coefficient  $\tau$  of the panel between cavities [38]:

$$\eta_{ij,cav} = \frac{\tau A_i c_0}{4\omega V_i}. \quad (4.9)$$

The damping loss factor of the panels are obtained experimentally for the panels installed in the measurement window, in order to account for damping added by the boundaries. The decay rate method (DRM) is used. It is described in section 4.5.2.

The modal density of the panels ( $n_2$  and  $n_4$ ) are obtained by integrating Eq. (4.10) over all heading directions,  $n(\omega) = \int_0^\pi n(\varphi, \omega) d\varphi$  [38]:

$$n(\varphi, \omega) = \frac{A_p k(\varphi, \omega)}{\pi^2 |c_g(\varphi, \omega)|}, \quad (4.10)$$

where  $\varphi$ ,  $A_p$ ,  $k$  and  $c_g$  are the heading angle, the area of the panel, the wavenumber and the group velocity of the panel. The latter two are determined from the solution of the panel's dispersion relation.

For an infinite unstiffened isotropic plate, Eq. (4.10) simplifies to:

$$n_i = \frac{A_i}{4\pi} \sqrt{\frac{\rho_i h_i}{D_i}}. \quad (4.11)$$

Here,  $D_i$  is the bending stiffness of the panel.

For the composite and sandwich panels, the general laminate model is used to compute the panel's wavenumber, which is directly used in Eq. (4.10). Details of the modelling are given in [32].

The radiation coupling loss factor between the panel and the cavities,  $\eta_{21}$ ,  $\eta_{23}$ ,  $\eta_{43}$  and  $\eta_{45}$ , are computed using the following equation [38]:

$$\eta_{ij,rad} = \frac{\rho_0 c_0 \sigma_{rad}}{\omega \rho_i h_i}. \quad (4.12)$$

Here,  $\rho_i$ ,  $h_i$  and  $\sigma_{rad}$  are the density, thickness and radiation efficiency of the panel. The latter is given by Eq. (4.13) integrating  $\sigma(k(\varphi, \omega))$  over all heading directions.  $\sigma(k(\varphi, \omega))$  is calculated using Leppington's approach [143].

$$\sigma(\omega) = \frac{1}{n(\omega)} \int_0^\pi \sigma(k(\varphi, \omega)) n(\varphi, \omega) d\varphi \quad (4.13)$$

In the present modelling, a layer of porous is not treated as an individual subsystem but its influence is taken into account. For the configuration in which the skin panel is lined with a porous layer, the porous material has four main effects: (1) it increases the mass-law of the panel, (2) it acts as an added-damping, increasing the damping loss factor of the panel, (3) it attenuates the panel's radiation so that Eq. (4.12) is multiplied by the additional term  $10^{-\frac{IL}{10}}$  in order to account for the Insertion loss (IL) of the porous material; (4) it increases the absorption of the cavity so that  $\alpha$  in Eq. (4.8) becomes an average between the absorption of the cavity walls and the absorption of the porous layer.

The low frequency non-resonant coupling linking the source and receiving cavities is given by  $\eta_{15}$ . It represents the system, which behaves as an equivalent non-resonant single wall moving in phase, for frequencies lower than the double wall resonance of the system, approximated by [35]:

$$f_D = \frac{1}{2\pi \cos(\theta)} \sqrt{\frac{\rho_0 c_0^2 (m_1 + m_2)}{(h_p + h_f) m_1 m_2}}. \quad (4.14)$$

Here  $m_1$ ,  $m_2$ ,  $h_p$  and  $h_f$  denote the mass of plates 1 and 2, the thickness of porous and the fluid layers, respectively. When a layer of porous material is present in the cavity, the terms  $\rho_0$  and  $c_0$  are modified by the properties of the porous. It is then averaged over the incidence angles.

Finally, no coupling exists between the source cavity and the trim panel  $\eta_{14} = 0$ , and between the skin panel and the receiver cavity  $\eta_{25} = 0$ . In addition, since the panels are not structurally connected, the coupling between panels is also neglected ( $\eta_{24} = 0$ ).

Once Eq. (4.6) is solved for an arbitrarily selected unit input power in the source room (diffuse acoustic field), the transmission loss is computed using the following equation [38]:

$$TL = NR + 10 \log_{10} \left( \frac{A_4}{\alpha A_5} \right) \quad (4.15)$$

Here,  $NR$  is the noise reduction given by:

$$NR = 10 \log_{10} \left( \frac{E_1}{E_5} \right) - 10 \log_{10} \left( \frac{V_1}{V_5} \right). \quad (4.16)$$

The term  $\frac{E_1}{E_5}$  is the energy ratio between source and receiving cavities and  $\frac{V_1}{V_5}$  is the ratio between the volumes of the source and receiving cavities.

## 4.5 Description of the measurements

This section describes the measurement of the SEA parameters of the studied panels. They are the damping loss factor, the modal density and the radiation efficiency. The transmission loss tests are also described. A comparison between the measured parameters and the presented models are given in section 4.6.

### 4.5.1 Description of the systems

The systems are composed of single or double-wall panels, made of aluminium, composite or sandwich composite. Their properties are given in tables 4.1 and 4.2. The panels are placed between a reverberant source room and a semi-anechoic receiver room. All panels have a surface area equal to 1.5 m<sup>2</sup>. The aluminium panel is orthogonally stiffened while the laminate composite is unidirectionally stiffened. Details on the location of the stiffeners are given in figure 4.4. For the double-wall configuration, a 4-in cavity separates

the two panels. It is filled with a 2-in aerospace grade fiberglass attached (but not bonded) to the source panel. Its properties are given in table 4.3. The tested configurations are summarized in table 4.4.

Table 4.1 Source panels properties

	Aluminium	Laminate
Thickness $h_i$ [m]	0.002	0.00275
Material density $\rho_i$ [kg.m <sup>-3</sup> ]	2742	1600
Young's modulus $E_i$ [GPa]	69	135, 8.5
Poisson ratio $\nu$	0.33	0.35

Table 4.2 Receiving sandwich panel properties

	Sandwich	
	Skin	Core
Thickness $h_i$ [m]	0.0005	0.0117
Material density $\rho_i$ [kg.m <sup>-3</sup> ]	2838	48
Young's modulus $E_i$ [MPa]	21180	0.1
Shear modulus $G_{12}$ [Mpa]	4000	-
Shear modulus $G_{13}$ [Mpa]	-	44
Shear modulus $G_{23}$ [Mpa]	-	25
Poisson ratio $\nu_{12}$	0.0667	0.01

Table 4.3 Porous material properties

	Porous
Thickness $h_p$ [m]	0.0508
Material density $\rho_t$ [kg.m <sup>-3</sup> ]	9.61
Porosity $\phi$	0.97
Airflow resistivity $\sigma$ [N.s.m <sup>-4</sup> ]	26557
Tortuosity $\alpha_\infty$	1.07
Viscous charac. length $\Lambda$ [m]	6.41x10 <sup>-5</sup>
Thermal charac. length $\Lambda'$ [m]	9.85x10 <sup>-5</sup>

Table 4.4 Single and double-walls tested configurations

Number	Layer 1	Layer 2	Layer 3	Layer 4
1	Aluminium			
2	Laminate			
3	Sandwich			
4	Aluminium	Porous		
5	Laminate	Porous		
6	Aluminium	Porous	Air	Sandwich
7	Laminate	Porous	Air	Sandwich

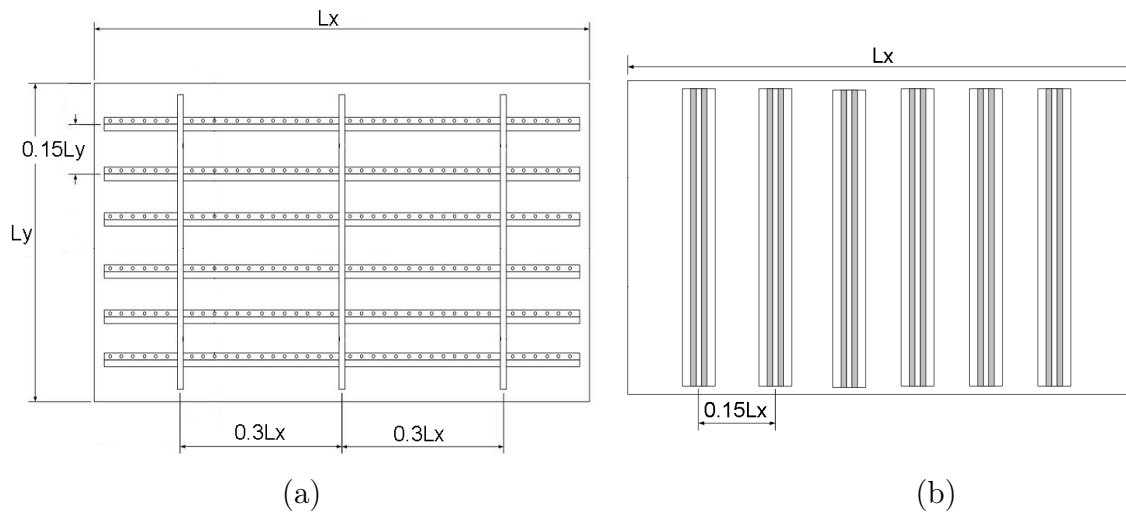


Figure 4.4 Dimension and spacing of the stiffeners: a) aluminium panel, b) composite panel

### 4.5.2 Damping loss factor

The damping loss factor of the panels placed on the measurement window are measured using the decay rate method (DRM). Tests were conducted with the panels mounted in the TL window. In consequence edge damping is accounted for. The excitation is performed using an electro-mechanical shaker and results are averaged over 3 random excitation locations and 15 randomly located points over the panel surface. A picture of the measurement setup is shown in Fig. 4.5a.

DRM is based on the decay of accelerometer signals, placed on the surface of the panel, when the excitation is turned off. Two assumptions are made: damping follows an exponential decay and all modes in a third-octave band present the same damping loss factor.

The damping loss factor equation is given below [53]:

$$\eta_{DRM} = \frac{DR}{27.3f}. \quad (4.17)$$

Here,  $DR$  is the slope of the decay in units of dB/second,  $f$  is the central frequency of a given one-third octave band.

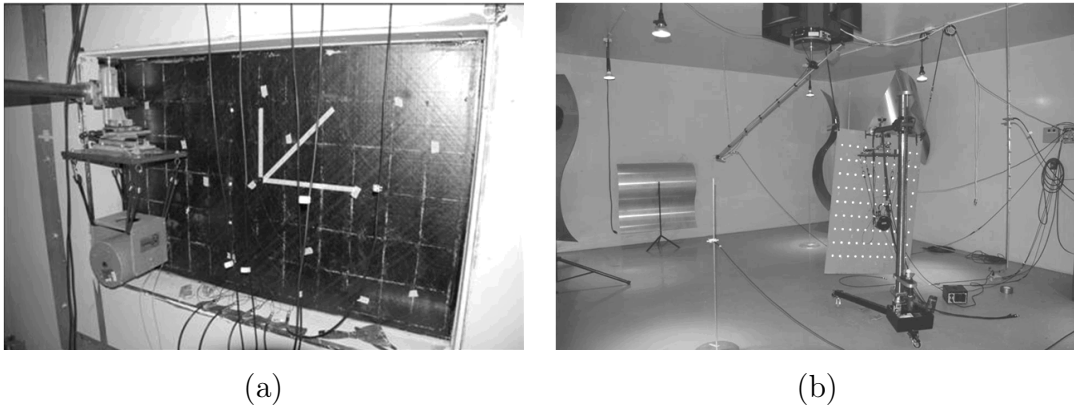


Figure 4.5 Picture of the measurement setups: (a) damping loss factor, (b) radiation efficiency.

### 4.5.3 Modal density

The modal density of the panels is measured with the panel suspended inside the anechoic room, in order to minimize radiation coupling between the panel and the room. It is obtained using the following formulation [67]:

$$n_i = 4m_i \langle Re(Y_p) \rangle, \quad (4.18)$$

where  $m_i$  is the mass of the panel,  $Re(Y_p)$  denotes the real part of the panel's input mobility  $Y_p = \frac{\phi_{fv}}{\phi_{ff}}$ .  $\phi_{fv}$  is the cross-spectrum between the force and the velocity signals at the excitation location and  $\phi_{ff}$  is the autospectrum of the force signal.

The presence of the impedance head and its attachment elements introduce a measurement error. A corrected admittance  $Y_c$  is obtained using the admittance of the impedance head  $Y_M$ , which is measured by exciting the impedance head without the driven plate:

$$Y_c = \frac{Y_p}{1 - \frac{Y_p}{Y_M}}. \quad (4.19)$$

In addition, errors associated with shaker-structure interaction and external noise are minimized by introducing the signal which drives the power amplifier  $s$  in the computation of  $Y_p$  [67]:

$$Y_p = \frac{\phi_{sv}}{\phi_{sf}}. \quad (4.20)$$

#### 4.5.4 Radiation efficiency

The radiation efficiency of the panels is measured with the panel freely suspended in the reverberant room. It is based on solving a two subsystems SEA equation wherein subsystem 1 and 2 denote the tested panel and the reverberant room, respectively.

$$\begin{bmatrix} \eta_{11} + \eta_{12} & -\eta_{21} \\ -\eta_{12} & \eta_{21} + \eta_{22} \end{bmatrix} \begin{Bmatrix} E_1 \\ E_2 \end{Bmatrix} = \begin{Bmatrix} \frac{\Pi_1}{\omega} \\ 0 \end{Bmatrix}. \quad (4.21)$$

Solving for  $\eta_{12}$  and using the reciprocity relation one obtains:

$$\eta_{12} = \frac{\eta_2 E_2}{E_1 - \frac{n_1}{n_2} E_2}. \quad (4.22)$$

Assuming both faces of the panel to radiate equally,  $\eta_{12} = 2\eta_{ij,rad}$  is thus twice the radiation coupling, given by Eq. (4.12).

The radiation efficiency is thus:

$$\sigma = \frac{1}{2} \left( \frac{n_2 \eta_2 E_2}{n_2 E_1 - n_1 E_2} \right) \frac{\omega m_1}{\rho_0 c_0 A_1}. \quad (4.23)$$

An electro-mechanical shaker with white-noise input is used to excite the panel. A picture of the measurement is shown in Fig. 4.5b. The modal density of the test panel  $n_1$  and the DLF of the cavity  $\eta_2$  are measured using the techniques described in the previous

sub-sections. The energy of the plate is computed from its mean quadratic velocity  $\langle v_1^2 \rangle$ , using the relation  $E_1 = m_1 \langle v_1^2 \rangle$ ; 15 velocity measurement locations were used in this equation. The energy of the room is obtained from its mean quadratic pressure  $\langle p_2 \rangle$ , using  $E_2 = \frac{\langle p_2^2 \rangle V_2}{\rho_0 c_0^2}$ , the latter is measured using a rotating microphone.

### 4.5.5 Transmission loss

The TL measurement follows ISO 15186-1:2000 standard [144]. The structure is fixed between a reverberant and an anechoic room using a mounting frame. Joints between the panels and the frame are sealed using silicon and aluminium tapes. The edges of the panels are sandwiched between two flat bars with a neoprene decoupler. A white-noise in the frequency range of 100 Hz to 10 kHz is generated in the reverberant room. The transmission loss of the structure is given by:

$$TL = (L_p - L_I - 6). \quad (4.24)$$

$L_p$  is the average sound pressure level in the source room, measured by a rotating microphone.  $L_I$  is the averaged intensity level over the measurement surface in the receiving room. The measurement is done by manually scanning the surface of the sample,  $A_i$ , with the intensimetry probe in order to obtain a spatial and temporal average. In the following discussion, the results are presented in one third-octave bands.

## 4.6 Results and discussion

The accuracy of the transmission loss predictions depends on the hypotheses of each modelling approach as well as on the accuracy of the input parameters. The input parameters needed for the transmission loss computation using the TMM method are mainly the damping loss factor and the mechanical properties of the panels, the acoustical properties of the fluid and porous material, and the thickness of each layer. The damping loss factor of the panels are obtained experimentally as described in section 4.5.2. The other above parameters are used in the computation of the modal density, the damping and the coupling loss factors of each subsystem of the SEA model. In this section a comparison between analytical and experimental estimation of panel's modal density and radiation efficiency is presented. Next, transmission loss results using the TMM and the SEA approaches are compared with measurements for both single and double-wall configurations.

### 4.6.1 Modal density

Modal density results for the aluminium, the laminate composite and the sandwich panel are shown in Fig. 4.6, 4.7 and 4.8, respectively. It should be recalled that present theoretical results neglect stiffeners effect.

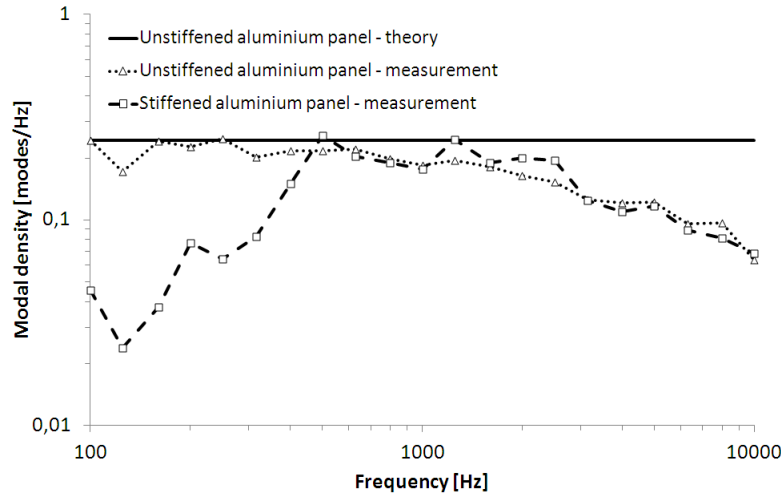


Figure 4.6 Modal density of the aluminium panel: comparisons between theory and measurement.

As shown in Fig. 4.6, a good agreement is observed at low and mid frequencies between the model and the unstiffened aluminium panel tested (solid and dotted curves, respectively). The main influence of stiffeners is observed in the low frequency range, due to an added stiffness effect. In this range, the panel behaves as an equivalent orthotropic stiff panel. The modal density of the stiffened panel reaches that of an unstiffened one when the panel's bending wavelength becomes lower than the spacing between horizontal stiffeners: for frequencies higher than 500 Hz. At frequencies higher than 3 kHz, the measured modal density decreases, in contradiction with the theoretical trend. This is traced to a limitation in injecting power via the electro-mechanical shaker. A similar behaviour is observed in the case of the composite laminate panel, as seen in Fig. 4.7. For this panel, due to the above mentioned limitation, experimental results are shown up to 5 kHz.

Measured results for the sandwich trim panel (Fig. 4.8) agree well with theory in the low frequency range and follows the theoretical increase with frequency given by the used general laminate model; however, experimental values are higher than theoretical ones. This difference may be due to an uncertainty in the determination of the shear modulus of the core and in to a lesser degree, the Young's modulus of the skins (the properties of table 4.2 were given by the supplier). Moreover, the low bending stiffness and the high damping

loss factor of the sandwich panel at high frequencies makes experimental modal density results valid only up to 3150 Hz, again a consequence of the difficulty in exciting the panel using a shaker. Better results may be obtained using a different excitation system such as a polyvinylidene fluoride (PVDF) exciter.

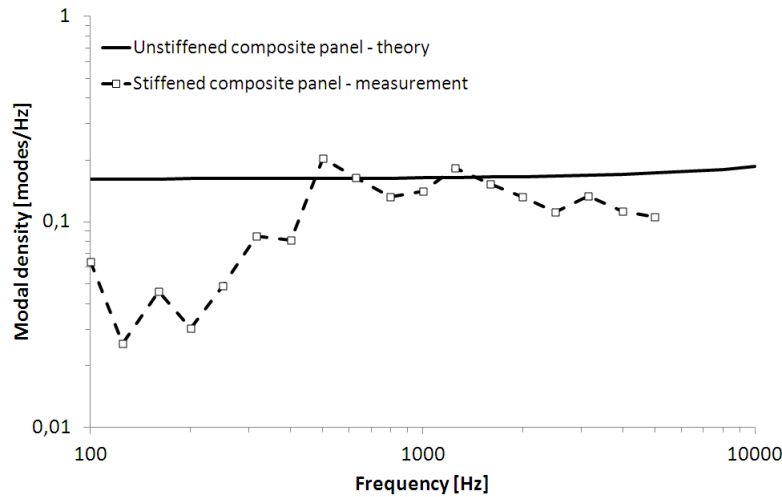


Figure 4.7 Modal density of the composite panel: comparison between theory and measurement.

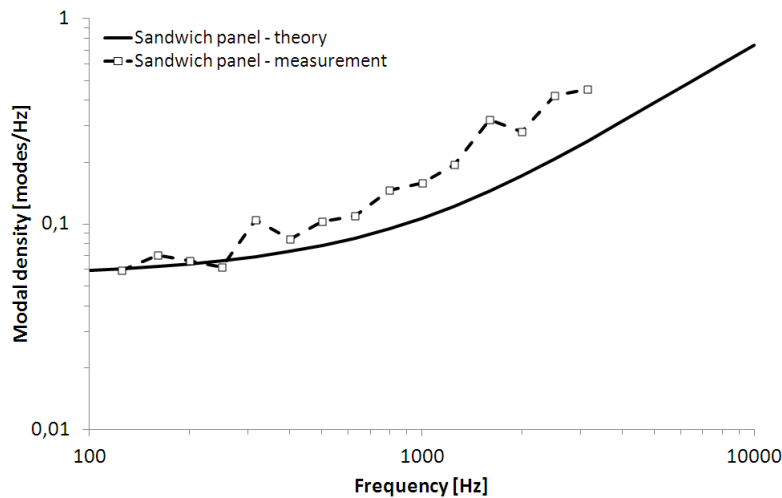


Figure 4.8 Modal density of the sandwich panel: comparison between theory and measurement.

## 4.6.2 Radiation efficiency

Fig. 4.9 and Fig. 4.10 show theoretical and experimental radiation efficiency for an unstiffened 3-mm thick aluminium panel and the sandwich panel, respectively. Theoretical results for the unstiffened panel show a good correlation with measurements in the critical

frequency region while experimental values are higher than theoretical ones in lower frequency regions. This is explained by the fact that theoretical radiation efficiency assumes a simply-supported boundary condition in a rigid baffle [143] while tests are performed with the panel suspended inside a reverberant room (free boundary conditions), as explained in section 4.5.4 and shown in Fig. 4.5b. In addition, the SEA based methodology to derive the radiation efficiency is submitted to limitations at low-frequencies.

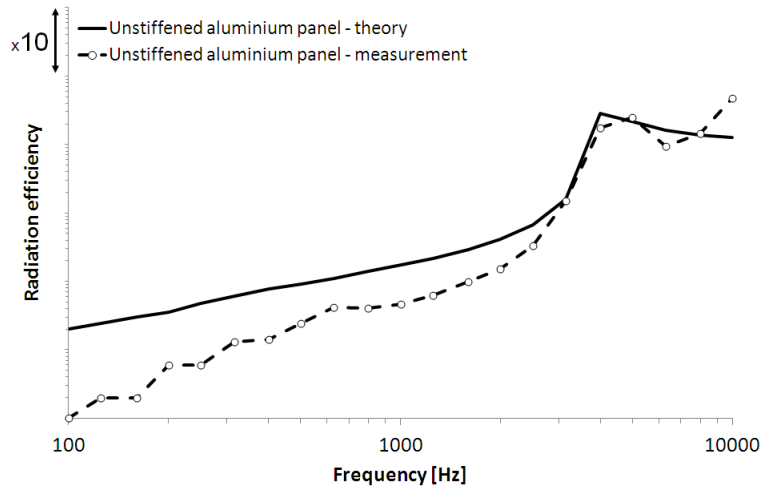


Figure 4.9 Radiation efficiency of a 3 mm unstiffened aluminium panel: comparison between theory and measurement.

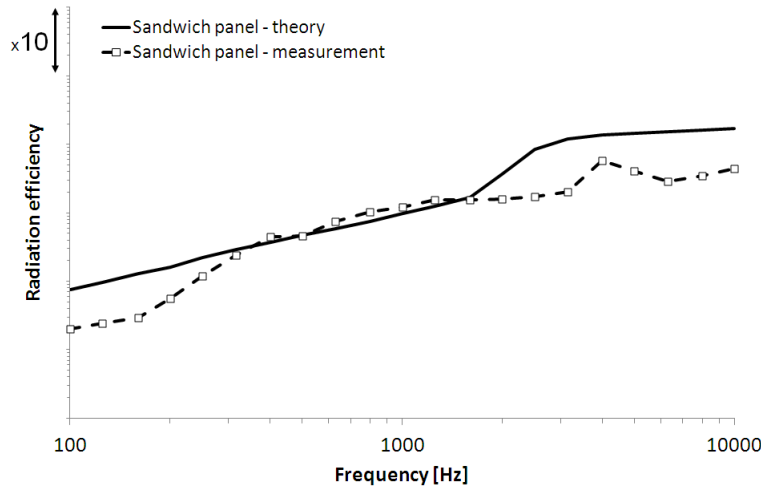


Figure 4.10 Radiation efficiency of the sandwich panel: comparison between theory and measurement.

Experimental results for the sandwich panel agree well with the general laminate model in the frequency range from 300 Hz to 1600 Hz, as seen in Fig. 4.10. At high frequencies, the radiation efficiency is not correctly measured due to the previously mentioned limitation

in exciting the panel. Between 100 Hz and 250 Hz the difference is due to the SEA limitations (less than 3 modes per frequency band) and boundary conditions as explained for the aluminium panel.

### 4.6.3 Transmission loss comparisons between TMM, SEA and measurements

This section compares TMM, SEA and measured transmission loss for the aluminium, laminate composite and sandwich panels. All parameters needed for the computation of the TL are obtained theoretically using formulations of section 4.4.2, except the damping loss factor of the panels, which are measured using the decay-rate method described in section 4.5.2. The influence of stiffeners and of a porous layer are also analysed. Predictions are next compared with experiments, in a double-wall configuration, considering an aluminium or a laminate composite skin.

#### Single-wall configurations

Fig. 4.11 shows theoretical and experimental transmission loss for an orthogonally stiffened aluminium panel. Experimental TL is also shown for an unstiffened aluminium panel (it corresponds to the skin of the stiffened panel, tested before stiffeners were added). Theoretical and experimental TL of the unstiffened panel are in good agreement. The critical frequency value is also well predicted. The SEA model presents higher differences compared to measurements than TMM in the critical frequency region. This happens because the SEA response is more sensitive to the panel's damping loss factor in this frequency region.

From the measured TL of the stiffened panel it is observed that stiffeners have an influence at low frequencies, increasing the TL of the panel. This is coherent with the low values of modal density, shown in Fig. 4.6 and analysed in section 4.6.1. In this frequency range the stiffness and mass of the panel are increased by the presence of stiffeners. When the bending wavelength of the panel is smaller than the distance between horizontal stiffeners (for frequencies higher than 500 Hz), the TL is dominated by the response of panel sections delimited by the stiffeners [23]. Since the radiation of the smaller sub-panels is higher than that of larger panels, the TL decreases. In addition, radiation from stiffeners further reduce the TL in the mass-law frequency region. At and above the critical frequency region the theoretical TL is lower than measurements, indicating an underestimation of the panel's damping loss factor. Indeed, the measurement of the panel's DLF is subjected to higher uncertainties in this frequency region. It should also be noted that a simple unstiffened

modelling is not adapted to predict the transmission behaviour of a bare stiffened panel. Indeed, an overestimation of about 8 dB is observed at 4 kHz in Fig. 4.11 between the model and the stiffened panel tested. However an unstiffened model is still acceptable when the fiberglass is added to the panel as shown below for the laminate composite panel. Description of analytical models for stiffened panels and comparison with testing can be found in [27, 28].

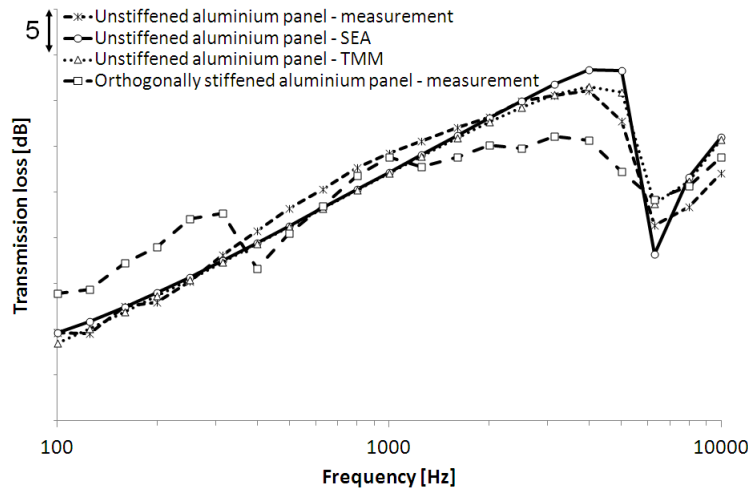


Figure 4.11 Transmission Loss of the aluminium panel: comparison between transfer matrix method (TMM), statistical energy analysis (SEA) and measurements for a bare panel and a panel with porous layer.

Fig. 4.12 shows results for the laminate composite panel. The models agree well with measurements up to 1 kHz. At higher frequencies the differences are due to the presence of stiffeners, which are not accounted for in the modelling. At low frequencies it is observed that the stiffeners have less influence on the TL when compared to the aluminium panel. Indeed, the aluminium panel is orthogonally stiffened while the composite panel has only vertical stiffeners. The measured TL of the composite panel lined with a porous material is also compared with the transfer matrix method (represented by the two curves with highest transmission loss). Theoretical SEA results are not included for this last configuration since they integrate the porous layer's insertion loss either experimentally or theoretically using the transfer matrix method, as explained in section 4.4.2. Similar conclusions are observed as in the case of the bare panel, except that the damping loss factor of the panel lined with the porous is well estimated, leading to a good agreement between theoretical and measured TL at and above its critical frequency. It should be noted that part of the radiation from stiffeners is attenuated by the porous layer, however the modelling of stiffened panels is still required to improve agreement with measurements. Similar results are observed for the aluminium panel (not shown for conciseness reasons).

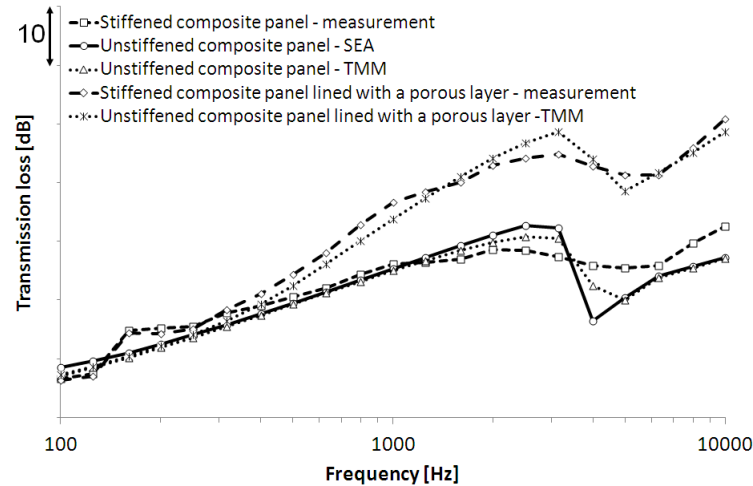


Figure 4.12 Transmission Loss of the composite panel: comparison between transfer matrix method (TMM), statistical energy analysis (SEA) and measurements for a bare panel and a panel with porous layer.

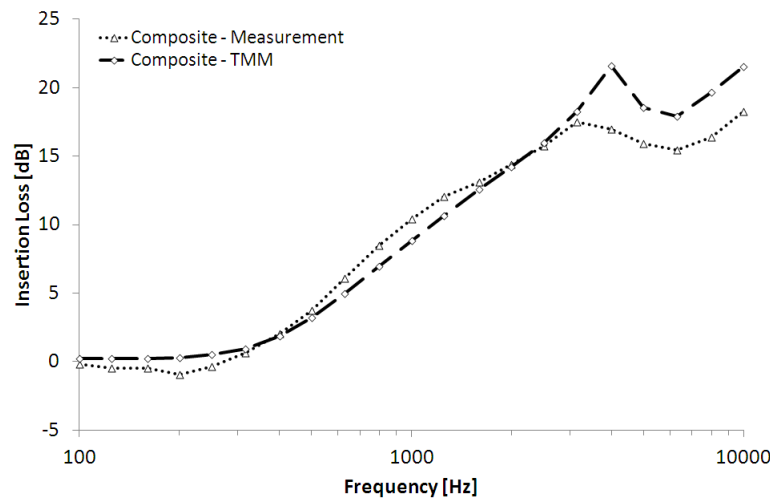


Figure 4.13 Difference between the Transmission Loss with and without the porous layer: comparison between transfer matrix method (TMM) and measurement for the composite skin panel.

An important information for practical insulation applications is the influence of porous layers on a panel's transmission loss. Therefore, it is interesting to determine if models can predict this influence, as an alternative to measurements. Fig. 4.13 shows theoretical and experimental difference between the TL of the composite skin panel with and without the porous layer. Results show that the efficiency of the porous layer increases with frequency up to the critical frequency of the panels (in this single wall configuration, the frequency range at which the porous layer masking effect becomes important is directly related to its absorption coefficient). Small differences between experimental and theoretical curves are

observed in the mass-law region since in the experimental case the porous layer reduces both the panel's and the stiffener's radiation while in the theoretical case the stiffeners are not modelled. Results for the aluminium panel are similar but this effect is higher compared to the composite case. At higher frequencies the added-damping effect of the porous layer is well captured by the model while differences in levels between theory and tests are linked to errors on the determination of panel's damping loss factor when it is lined or not with the porous layer.

Theoretical and experimental transmission loss for the sandwich panel are shown in Fig. 4.14. Both models are in good agreement with measurements in the mass-law region. In the critical frequency region (around 2500 Hz), differences are due to uncertainties in the measurement of the panel's damping loss factor, particularly for SEA computations. This difference can be also caused by uncertainties in the properties of the panel, notably the shear moduli of the core, resulting in a shift of its critical frequency. Prediction using a Finite element/Boundary element model leads to similar results thus corroborating this assumption.

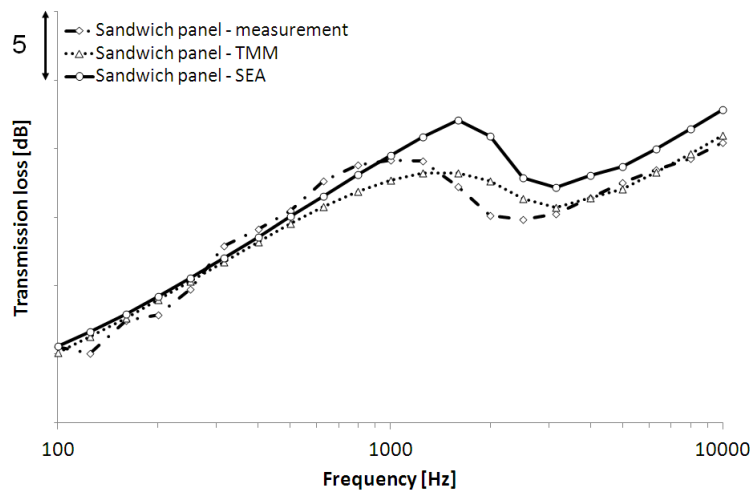


Figure 4.14 Transmission Loss of the sandwich panel: comparison between transfer matrix method (TMM), statistical energy analysis (SEA) and measurement.

### Double-wall configurations

The panels response in the double-wall configuration, as illustrated in Fig. 4.1, is analysed in this section. Transmission loss results for the aluminium skin configuration are shown in Fig. 4.15. Overall, SEA and TMM responses are equivalent for frequencies below the critical frequency of the skin panel. Minor differences between models are observed for frequencies below 1 kHz and are traced to the contribution of cavities modes parallel to

the panels' surface. These modes are not accounted for in the TMM formulation, which only assumes 1D propagation (infinite lateral dimensions). Both models overestimate the experimental transmission loss of about 7 dB up to the coincidence frequency region. Differences at frequencies lower than 500 Hz are due to the stiffeners, which are not accounted for in the modelling. The decoupling frequency, given by eq. (4.14), is around 125 Hz as observed in predicted curves. It is not observed in the experimental curve due to the high damping and limitations of the used test facility (cutoff frequency of 200 Hz for the reverberation room as well as niche effects). Differences in the coincidence region are related to the attenuation of the radiation by the porous layer, which is overestimated in this frequency range, as shown in Fig. 4.13. Similar results are observed for the composite skin case, shown in Fig. 4.16. Tests done on a simpler double wall systems made up from two aluminum panels show very good agreement ( a different mounting setup was used for these test compared to the tests presented in this paper). In consequence, the observed discrepancies are certainly related to the complexity of the used structures (effect of stiffeners) and/or uncertainty on the sandwich (trim) panel.

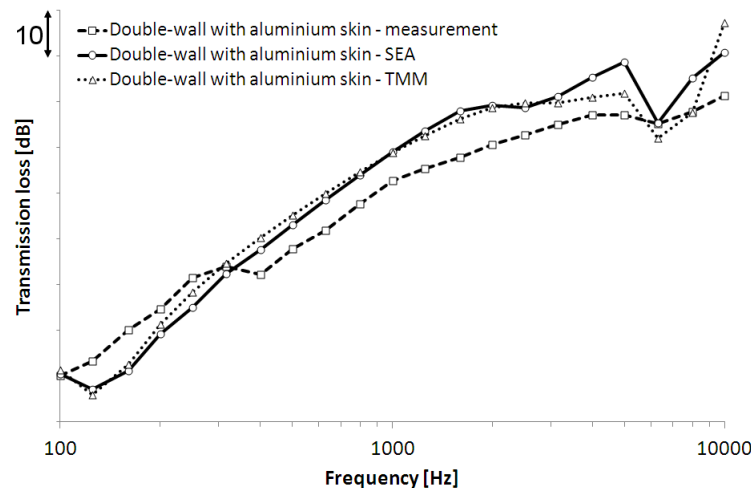


Figure 4.15 Transmission Loss of the double wall with the orthogonally-stiffened aluminium skin panel: comparison between transfer matrix method (TMM), statistical energy analysis (SEA) and measurement.

Another comparison of practical importance for aircraft applications is the impact on the double-wall transmission loss of the main structure; aluminum vs. composite skin. The accuracy of theoretical models in predicting this impact is analysed in Fig. 4.17 as a difference between the double-wall transmission loss with the composite skin and with the aluminium skin. Between 400 Hz and 3 kHz, TMM is in better agreement with measurements than SEA. At lower frequencies both models give the same trends but since stiffeners are not modelled, results do not agree with measurements. Between 3 kHz and 6

kHz, in the coincidence frequency region of the panels, the models predict the dip found in the experimental curve but it is highly overestimated due to uncertainties in the damping loss factor of the panels. At higher frequencies, better agreement with measurements is observed with the SEA approach.

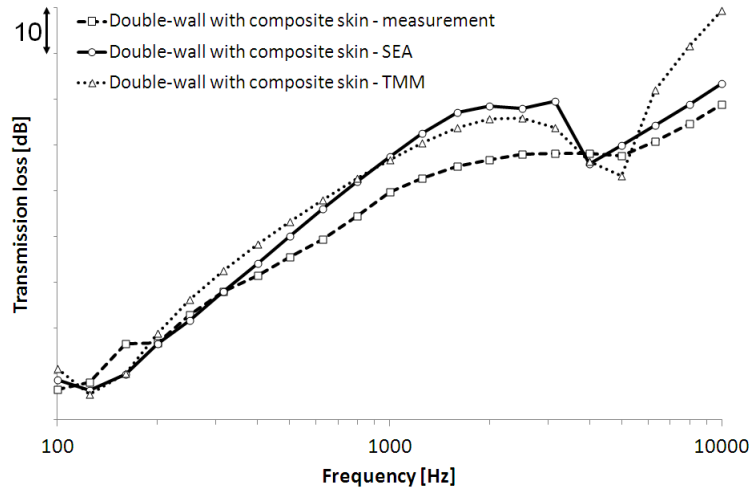


Figure 4.16 Transmission Loss of the double wall with the vertically-stiffened composite skin panel: comparison between transfer matrix method (TMM), statistical energy analysis (SEA) and measurement.

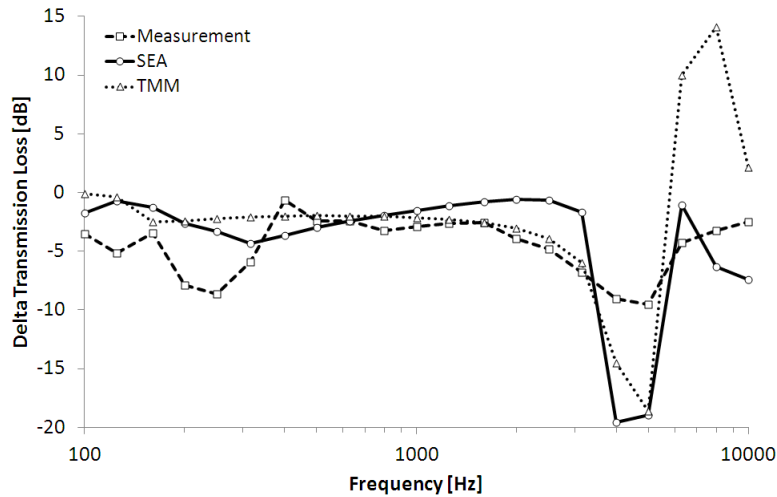


Figure 4.17 Difference between the DWL Transmission Loss with the composite skin panel and the DWL Transmission Loss with the aluminium skin panel: comparison between transfer matrix method (TMM), statistical energy analysis (SEA) and measurement.

## 4.7 Conclusion

This paper investigated the accuracy of two approaches to predict the sound transmission loss through aircraft double-wall partitions. They are the transfer matrix method (TMM) and statistical energy analysis (SEA). Similar trends are observed for the two models. However, an overestimation of about 7 dB in the frequency range from 400 Hz up to 5 kHz is observed when compared to measurement results. It is traced to the complexity of the structure, composed of stiffened isotropic and laminate composite skin panels and a sandwich trim panel. Other comparisons done for double-wall systems composed of thin metallic panels have shown that both methods predict well the measured transmission loss. In addition, it is observed that TMM model predicts well the porous layer effect on the transmission loss in the mass-law region. Moreover, the two methods allow for the prediction of the difference between aluminium and composite panel on the transmission loss in the mass-law region.

The main discrepancies between theory and experiments are linked to three factors: (1) the influence of stiffeners, which are not modelled, mainly decreasing the transmission loss at low and mid frequencies; (2) the overestimation of the sandwich panel experimental transmission loss, increasing thus the transmission loss of the double-partition between 1 kHz and 3 kHz; (3) a difficulty in accurately determining the damping loss factor of the panels in their critical frequency region. Improvements in the models to represent a more realistic aircraft configuration should include stiffeners on the skin panel and account for structural transmission via vibration isolators connecting the inner and outer panels of an aircraft sidewall structure. On-going research on this latter point [145] will be integrated in the double-wall SEA prediction model. Moreover, an important extension to the validation performed in this paper is to consider excitation fields more representative of in-flight conditions such as turbulent boundary layer excitation.

## Acknowledgements

The authors would like to acknowledge Maxime Bolduc and Patrick Levesque, from University of Sherbrooke, for their technical assistance and help with experiments.

## 4.8 Supplementary analysis on academic double-walls

In this section, the prediction of the double-wall transmission loss under diffuse acoustic field using TMM and SEA is compared with experimental results conducted at the University of Sherbrooke<sup>a</sup>. The double-wall studied is composed of two unstiffened aluminium panels of surface (1.5 m × 1 m), having a thickness of 2 mm and 1 mm and a cavity of 3.5 inches. The system is analysed in three configurations: (1) empty cavity, (2) cavity partially filled with 2 in. of melamine foam and (3) cavity almost filled with a 3 in. of glass-wool. The porous materials are lined but not bonded to the panel. These configurations are represented in Fig. 4.18. The properties of the aluminium panels as well as of the glass wool are given in the paper presented in this chapter. The properties of the melamine foam are given in table 4.5. The damping loss factor of the panels are assumed to be 0.003. When the cavity between panels is empty the transmission is mainly driven by the damping inside the cavity. For this reason, its damping loss factor in the empty configuration is assessed experimentally from reverberation time measurements using a microphone inside the cavity.

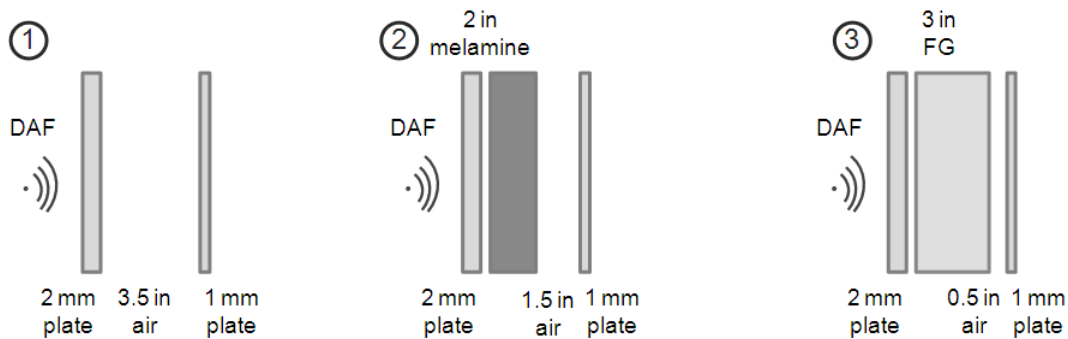


Figure 4.18 Representation of the three studied configurations.

The experimental setup is shown in Fig. 4.19. The 2 mm panel is flush-mounted to the wall of the source side. In consequence, the 1 mm panel is mounted inside a niche on the receiver side. In order to avoid experimental leaks and niche walls radiation, heavy bags were added to the boundaries of the measurement window on the source and receiver sides. In addition, extra isolation is provided in the source side construction (mounting frame) made up from by plywood, gypsum and glass-wool blankets.

<sup>a</sup>. Maxime Bolduc and Vincent Pointel are acknowledged for providing experimental results presented in this section.

Table 4.5 Melamine foam properties

	Porous
Young's modulus $E$ [ $\text{N}\cdot\text{m}^{-2}$ ]	80000
Damping loss factor $\eta$	0.17
Poisson's ration $\eta$	0.4
Material density $\rho_t$ [ $\text{kg}\cdot\text{m}^{-3}$ ]	8.8
Porosity $\phi$	0.99
Airflow resistivity $\sigma$ [ $\text{N}\cdot\text{s}\cdot\text{m}^{-4}$ ]	10900
Tortuosity $\alpha_\infty$	1.02
Viscous charac. length $\Lambda$ [m]	$100 \times 10^{-6}$
Thermal charac. length $\Lambda'$ [m]	$130 \times 10^{-6}$

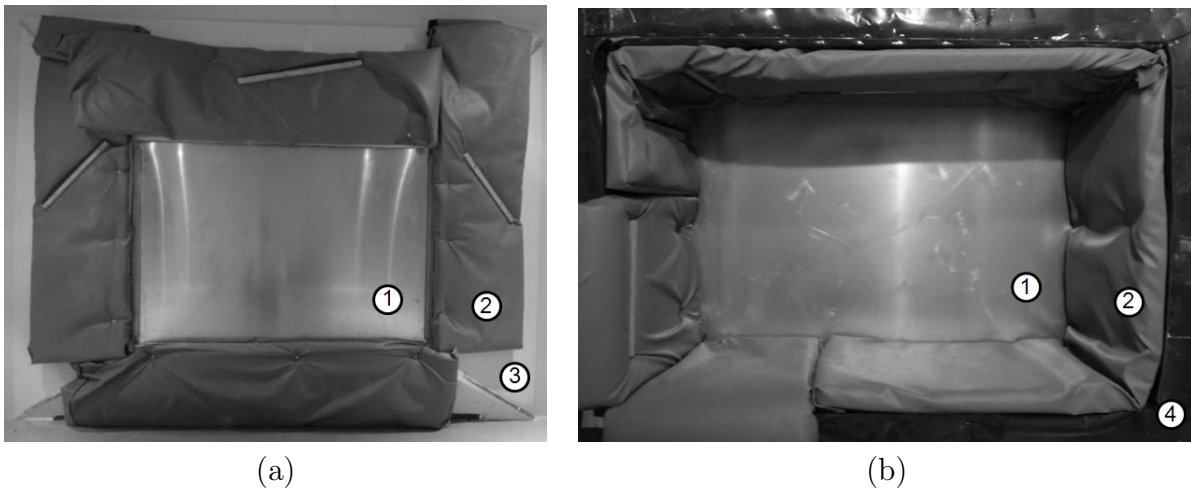


Figure 4.19 Experimental setup for the transmission loss measurement of the double-wall: (a) source side and (b) receiver side. 1-Aluminium panels, 2-heavy bags, 3-plywood, gypsum and glass wool, 4-measurement niche.

The transmission loss of the double-wall in the three configurations are shown in Fig. 4.20 to Fig. 4.22. For the configuration including an empty cavity (Fig. 4.20), the TMM and SEA models give similar results in low frequencies and differences are observed mainly in the mid-frequency range due to different assumptions of each approach for the modelling of the inner cavity. The agreement with tests is better from the first cavity mode in the thickness direction (2 kHz), at which the radiation of the panels inside the cavity becomes important. The main limitations of the models in predicting the experimental TL are due to uncertainties in the determination of the damping loss factor inside the cavity.

For the configuration including the melamine foam (Fig. 4.21), both models show good agreement with tests. As explained for the empty cavity configuration, the differences between theoretical approaches are mainly related to the modelling of the inner cavity. Here the damping in the 1.5in air gap is set to 0.7% since the damping is controlled by

the melamine. Finally, for the configuration including the glass-wool (Fig. 4.22), while the agreement between models is excellent, the agreement with tests is not good at high frequencies (above 1000 Hz). Both models overestimate the measurement. Testing using this limp glasswool is more challenging due to installation effects. Moreover, it is observed that the limit of the used experimental setup is reached at high frequencies (the measured TL is already higher than 80 dB around 3 kHz). Finally, this configuration could be considered challenging for the SEA approach since the cavity is almost filled with glass-wool, reducing thus its resonant behaviour. However, the representation of the inner cavity as a subsystem in the SEA approach is still found acceptable.

The presented results demonstrate the validity of both methods for double wall systems and confirm the source of discrepancies for the more representative sidewall structures (stiffeners effects, modelling the trim panels and uncertainties on its proprieties). They also show the challenge of conducting transmission loss measurements for such highly insulating constructions.

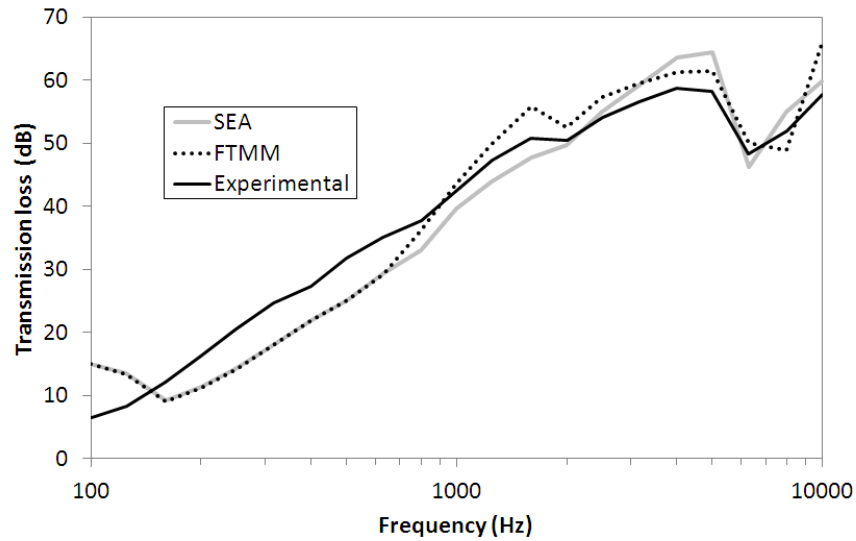


Figure 4.20 Transmission loss of the double-wall composed of a 2 mm aluminium panel, 3.5 in. of air gap and 1 mm aluminium panel.

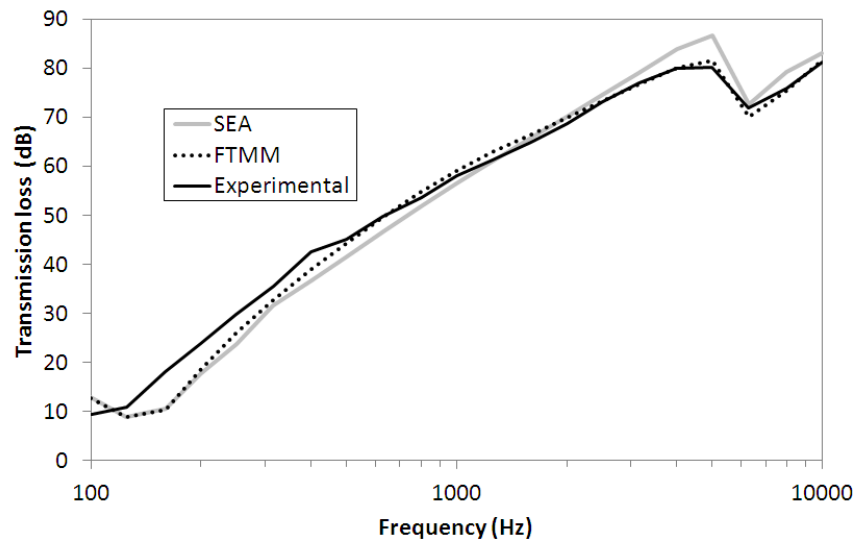


Figure 4.21 Transmission loss of the double-wall composed of a 2 mm aluminium panel, 2 in. of melamine foam, 1.5 in. of air gap and 1 mm aluminium panel.

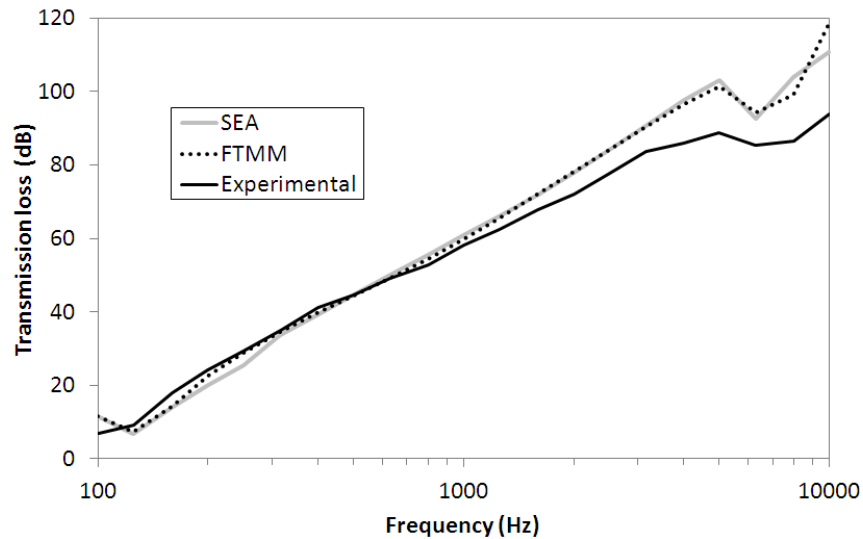


Figure 4.22 Transmission loss of the double-wall composed of a 2 mm aluminium panel, 3 in. of glass wool (0.6 pcf), 0.5 in. air gap and 1 mm aluminium panel.



# CHAPTER 5

## SOUND TRANSMISSION THROUGH MECHANICALLY COUPLED AIRCRAFT DOUBLE-WALLS

### 5.1 Chapter introduction

This chapter analyses the sound transmission through aircraft double-walls under acoustic excitation using the model developed in chapter 4 and integrating structural links between panels, using the approach presented in chapter 3. Particularly, the influence of mechanical links on the total transmission loss of the double-wall is investigated. In addition, the contributions of airborne and structure-borne transmission paths are identified using a transfer path analysis. Results are presented in the paper that will be submitted to the *Journal of the Acoustical Society of America*. Next, the model is modified to account for structural excitation. Comparisons with tests and FEM results are then analysed and the transmission paths are identified. Information on the paper and its abstract are given hereafter in French. As a complement, principles of the modelling of double-walls under turbulent boundary layer excitation are briefly discussed in Appendix A.

### 5.2 Double-wall SEA modelling under acoustic excitation (diffuse field)

Dans cette section, l'article intitulé "*Effects of structural links on the Transmission loss of aircraft double-walls under diffuse acoustic field: Measurements and SEA*" est présenté. Il sera soumis au *Journal of the Acoustical Society of America*.

#### **Auteurs et affiliation :**

B. Campolina : Airbus Operations SAS, Acoustic and Environmental Department, Route de Bayonne, 316 F31060 Toulouse Cedex 09, France.

N. Atalla : GAUS, Department of Mechanical Engineering, Université de Sherbrooke, Sherbrooke, Quebec, Canada J1K 2R1.

N. Dauchez : LISMMA, Institut Supérieur de Mécanique de Paris, 3, rue Fernand Hainaut, 93407 Saint-Ouen, France.

**Revue :** Journal of the Acoustical Society of America.

**Titre français :** Effet de liens mécaniques sur la perte par transmission de double-parois d'avion sous champ acoustique diffus : résultats expérimentaux et analyse statistique énergétique.

### **5.2.1 Résumé de l'article à être soumis au Journal of the Acoustic society of America**

Cet article présente l'effet des liens mécaniques sur la perte par transmission de double-parois d'avion. La structure est modélisée par la méthode de l'analyse statistique énergétique (SEA). Les composants de la double-paroi sont : (1) un panneau source raidi; (2) une cavité interne partiellement remplie avec un matériau fibreux et (3) un panneau d'habillage de type sandwich dont la zone de coïncidence est autour de 2500 Hz. Ces panneaux sont connectés mécaniquement par des liens rigides ou des liens anti-vibratiles. Deux panneaux sources sont considérés : (1) métallique et (2) composite. Dans le premier cas, les liens mécaniques sont placés sur le raidisseur. Dans le deuxième cas, les liens sont placés sur la peau du panneau source. Un modèle simple basé sur la SEA est présenté et comparé aux essais. Cette structure est excitée par un champ diffus dans la gamme de fréquence entre 100 Hz et 10 kHz. Une analyse des différents chemins de transmission montre que : (1) la transmission aérienne non-résonante domine en basses fréquences, (2) la transmission due au rayonnement des plaques est importante dans la zone de coïncidence des panneaux et (3) la transmission solidienne par les liens mécaniques augmente le bruit transmis en moyennes et hautes fréquences. Par ailleurs, il est montré que l'amélioration de la perte par transmission via le découplage par liens anti-vibratiles, en comparaison à des liens rigides, est moins importante dans le cas où les liens sont placés sur les raidisseurs du panneau source.

**Paper to be submitted to the Journal of the Acoustical society of America**

## Effects of structural links on the Transmission loss of aircraft double-walls under diffuse acoustic field: Measurements and SEA

### Abstract

The effect of structural links on the transmission loss of double-walls representative of an aircraft fuselage is studied in this paper. The system, analysed using statistical energy analysis (SEA), is composed of: (1) a stiffened skin panel, (2) an air gap partially filled with a fibrous layer and (3) a sandwich trim panel. The panels are structurally connected via either rigid elements or vibration isolators. Two configurations are considered: (1) a metallic or (2) a laminate composite skin panel, with critical frequencies around 6 kHz and 4 kHz, respectively. For the first one, stiffeners are part of the structural connection. For the second one, links connect directly the skins of the panels. A simple model based on SEA is presented and compared with tests. The structure is excited by a diffuse acoustic field in the frequency range from 100 Hz to 10 kHz. A transfer path analysis shows that (1) non-resonant airborne transmission dominates in low frequencies, (2) airborne radiation is significant in the critical frequency region of the panels while (3) structure-borne radiation increases the noise transmitted in the mid and high frequency ranges. In addition, comparisons between coupling via rigid elements or via vibration isolators show that the acoustic benefit provided by the isolators is lower when the trim is linked via frame stiffeners of the skin panel.

**keywords:** Transfer path analysis, Statistical energy analysis, Structure-borne transmission, Vibration isolator.

### 5.2.2 Paper to be submitted to the Journal of the Acoustical Society of America - Introduction

This study is included in the context of noise control treatments to decrease noise transmitted through a lightweight double-wall structure with mechanical links. Different methods exist to account for the modelling of the transmission loss of such structures. Craik [3, 141] improved the non-resonant transmission through double-walls for building applications using Statistical Energy Analysis (SEA) [53] as well as the integration of the structural transmission via wall ties. Legault & Atalla [62] treated the influence of mechanical links on the transmission through double panels typical of aircraft structures using a periodic approach and a four-pole modelling of the links. They also compare their model to various

simple (decoupled) methods and tests. Vigran [50] integrates the contribution of the structural connections in the transfer matrix method [5] using a technique derived from the semi-empirical model put forward by Sharp [51]. The links are modelled as rigid mass-less connections.

This paper focuses on the modelling of the sound transmission loss (TL) through structurally-linked aircraft double-walls. The modelling is based on the SEA approach. Contrary to the other approaches, a complex system (heterogeneous and non-periodic) is represented by global averaged parameters and the contribution of each transmission path to the system's total response is readily available. It integrates structural coupling loss factors via isolators using a four-pole modelling [145]. The system is composed of: (1) a stiffened skin panel, (2) an air gap partially filled with a fibrous layer and (3) a sandwich trim panel. The panels are structurally connected via either rigid elements or vibration isolators. Two configurations are analysed: (1) a metallic and (2) a laminate composite skin panel, with critical frequencies around 6 kHz and 4 kHz, respectively. A representation of the configurations is shown in Fig. 5.1. The structure is subjected to a diffuse acoustic field in the frequency range from 100 Hz to 10 kHz. Finally, a transfer path analysis is performed in order to identify the contribution of each transmission path in the entire frequency range of interest.

A description of the SEA modelling as well as of the transfer path analysis is given in section 5.2.3. Details of the measured structures and a description of the transmission loss tests are outlined in section 5.2.4. Finally, section 5.2.5 is devoted to the comparison between theoretical and experimental results as well as to a discussion on the different transmission paths.

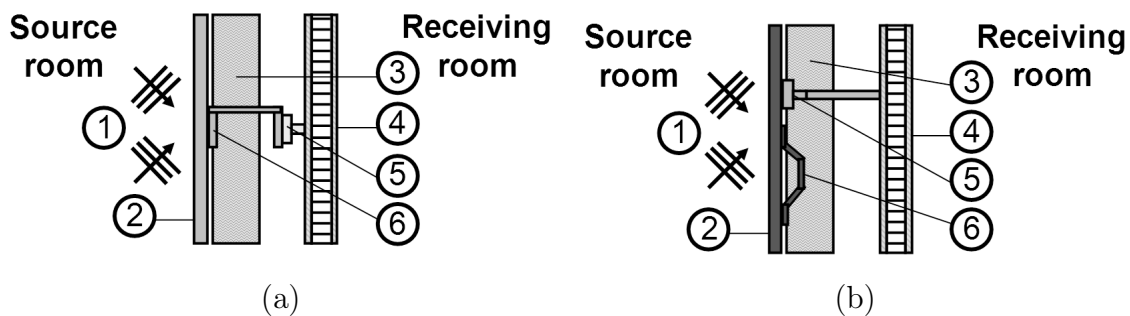


Figure 5.1 Representation of the double-wall structure: a) aluminium skin panel, b) composite skin panel. 1-diffuse field excitation, 2-skin panel, 3-porous layer, 4-trim panel, 5-vibration isolator, 6-stiffener.

### 5.2.3 Theory

The SEA model to predict the transmission loss of double-wall structures including isolators is presented here. A transfer path analysis, allowing for the separation of airborne and structure-borne contributions to the total TL, is also described.

#### Double-wall SEA model

A SEA model [3, 38, 53, 141] for the prediction of the TL of double-wall structures, shown in Fig. 5.1, is explained here. In this approach, the whole structure is divided into 5 subsystems such as shown in Fig. 5.2. A source, an inner and a receiver cavity are modelled. They are represented by subsystems 1, 3 and 5. The skin and trim panels, regrouping bending modes, are represented by subsystems 2 and 4. The resulting linear system is given by Eq. (5.1). Each subsystem  $i$  is represented by an energy value  $E_i$ , a modal density  $n_i$ , a damping loss factor (DLF)  $\eta_{ii}$  and an input power  $\Pi_i$ . In addition, coupling between subsystems  $i$  and  $j$  are represented by a coupling loss factor (CLF)  $\eta_{ij}$ . It is linked to  $\eta_{ji}$  by the reciprocity relation given by Eq. (5.2).

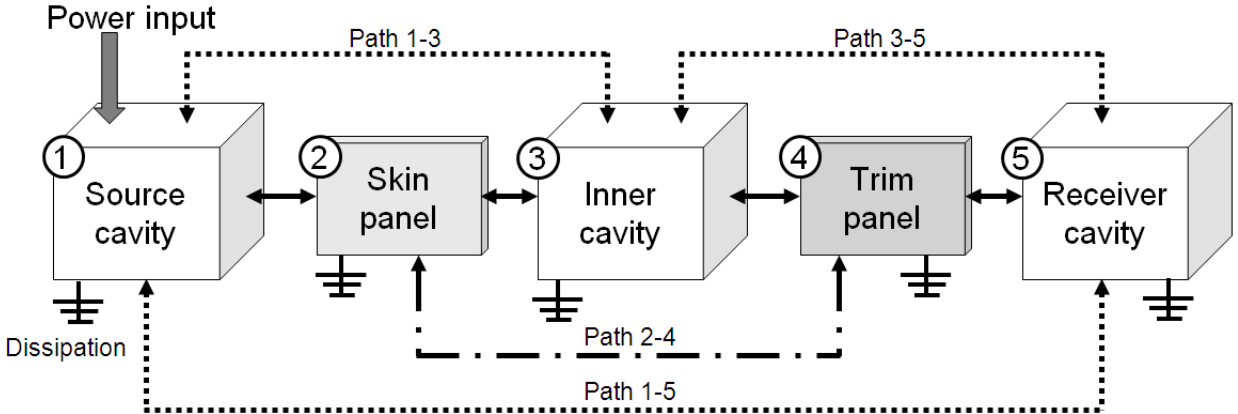


Figure 5.2 SEA representation of the double-wall system.

$$\begin{bmatrix}
 \eta_{11} + \sum_{i \neq 1} \eta_{1i} & -\eta_{21} & -\eta_{31} & -\eta_{41} & -\eta_{51} \\
 -\eta_{12} & \eta_{22} + \sum_{i \neq 2} \eta_{2i} & -\eta_{32} & -\eta_{42} & -\eta_{52} \\
 -\eta_{13} & -\eta_{23} & \eta_{33} + \sum_{i \neq 3} \eta_{3i} & -\eta_{43} & -\eta_{53} \\
 -\eta_{14} & -\eta_{24} & -\eta_{34} & \eta_{44} + \sum_{i \neq 4} \eta_{4i} & -\eta_{54} \\
 -\eta_{15} & -\eta_{25} & -\eta_{35} & -\eta_{45} & \eta_{55} + \sum_{i \neq 5} \eta_{5i}
 \end{bmatrix}
 \begin{bmatrix}
 E_1 \\
 E_2 \\
 E_3 \\
 E_4 \\
 E_5
 \end{bmatrix}
 =
 \begin{bmatrix}
 \frac{\Pi_1}{\omega} \\
 0 \\
 0 \\
 0 \\
 0
 \end{bmatrix}.
 \quad (5.1)$$

$$\eta_{ij}n_i = \eta_{ji}n_j. \quad (5.2)$$

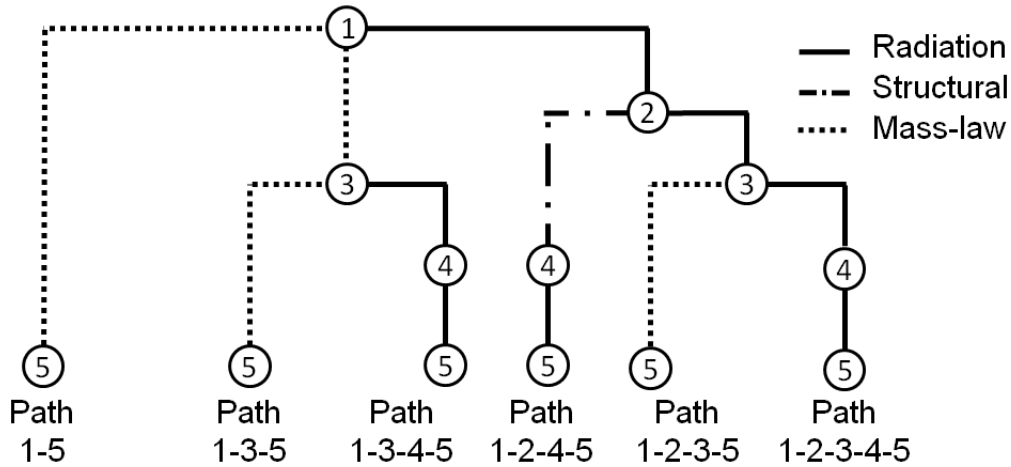


Figure 5.3 Sound transmission paths of the double-wall SEA system. 1-Source cavity, 2- skin panel, 3-inner cavity, 4-trim panel, 5-receiver cavity.

### Transmission loss computation

The transmission loss (TL) of the double-wall structure is computed using the following equation [38]:

$$TL = NR + 10 \log_{10} \left( \frac{A_4}{\alpha_5 A_5} \right), \quad (5.3)$$

where  $A_4$  is the area of the trim panel.  $A_5$  the total area of the receiver cavity and  $\alpha_5$  its average absorption coefficient (assumed 0.01 for the cavities 1 and 5).  $NR$  is the noise reduction, defined below:

$$NR = 10 \log_{10} \left( \frac{E_1}{E_5} \right) - 10 \log_{10} \left( \frac{V_1}{V_5} \right), \quad (5.4)$$

where  $V_i$  is the volume of subsystem  $i$  and the term  $\frac{E_1}{E_5}$  is the energy ratio between source and receiver cavities, which is obtained directly from the SEA Eq. (5.1). It should be noted that the the properties and dimensions of the source and receiver cavities are arbitrary, however, they are chosen so that the modal density and damping loss factor of the cavities are within the SEA limits of application ( $V_1 = V_5 = 10 \text{ m} \times 10 \text{ m} \times 10 \text{ m}$ ). Moreover, the

input power  $\Pi_i$ , is arbitrarily fixed since only the ratio between the source and receiver energies is needed in Eq. (5.4).

### SEA parameters determination

The modal densities of the cavities ( $n_1$ ,  $n_3$  and  $n_5$ ) are calculated using the high frequency approximation of room acoustics [142]:

$$n_i = \frac{V_i \omega^2}{2\pi^2 c_0^3}. \quad (5.5)$$

The damping loss factor of the cavities ( $\eta_{11}$ ,  $\eta_{33}$  and  $\eta_{55}$ ) are given by [141]:

$$\eta_{ii} = \frac{\alpha_i A_i c_0}{4\omega V_i}. \quad (5.6)$$

Here,  $\alpha_i$  and  $A_i$  are the absorption coefficient of the cavity, assumed 0.01, and its total surface. For the inner cavity the average absorption coefficient accounts for the absorption added by the glasswool.

The coupling loss factor between cavities ( $\eta_{13}$  and  $\eta_{35}$ ) are calculated using the mass-law transmission coefficient  $\tau$  of the panel between cavities [38]:

$$\eta_{ij, cav} = \frac{\tau A_i c_0}{4\omega V_i}. \quad (5.7)$$

The damping loss factor of the panels are obtained experimentally for the panels installed in the measurement window, in order to account for damping added by the boundaries. The decay rate method is used [53].

The modal density of the panels ( $n_2$  and  $n_4$ ) are obtained by integrating Eq. (5.8) over all heading directions,  $n(\omega) = \int_0^\pi n(\varphi, \omega) d\varphi$  [38]:

$$n(\varphi, \omega) = \frac{A_p k(\varphi, \omega)}{\pi^2 |c_g(\varphi, \omega)|}, \quad (5.8)$$

where  $\varphi$ ,  $A_p$ ,  $k$  and  $c_g$  are the heading angle, the area of the panel, the wavenumber and the group velocity of the panel. The latter two are determined from the solution of the panel's dispersion relation.

For an unstiffened isotropic plate, Eq. (5.8) simplifies to:

$$n_i = \frac{A_i}{4\pi} \sqrt{\frac{\rho_i h_i}{D_i}}. \quad (5.9)$$

Here,  $D_i$  is the bending stiffness of the panel.

For the composite and sandwich panels, the general laminate model is used to compute the panel's wavenumber, which is directly used in Eq. (5.8). Details of the modelling are given in [32].

The radiation coupling loss factor between the panel and the cavities,  $\eta_{21}$ ,  $\eta_{23}$ ,  $\eta_{43}$  and  $\eta_{45}$ , are computed using the following equation [38]:

$$\eta_{ij,rad} = \frac{\rho_0 c_0 \sigma_{rad}}{\omega m_i}. \quad (5.10)$$

Here,  $\sigma_{rad}$  is the radiation efficiency of the panel. It is obtained using the Leppington approach [143] and integrated over all heading directions:

$$\sigma(\omega) = \frac{1}{n(\omega)} \int_0^\pi \sigma(k(\varphi, \omega)) n(\varphi, \omega) d\varphi \quad (5.11)$$

In the present modelling, a layer of porous is not treated as an individual subsystem but its influence is taken into account. For the configuration in which the skin panel is lined with a porous layer, the porous material has four main effects: (1) it increases the mass-law of the panel, (2) it acts as an added-damping, increasing the damping loss factor of the panel, (3) it attenuates the panel's radiation so that Eq. (5.10) is multiplied by the additional term  $10^{-\frac{IL}{10}}$  in order to account for the Insertion loss ( $IL$ ) of the porous material; (4) it increases the absorption of the cavity so that  $\alpha$  in Eq. (5.6) becomes an average between the absorption of the cavity walls and the absorption of the porous layer.

The coupling loss factor between panels via the structural links,  $\eta_{24}$ , is given by [145]:

$$\eta_{24} = \frac{N Re(Zp_4) \vartheta}{\omega m_2}. \quad (5.12)$$

In this equation,  $\vartheta = \frac{\langle v_{4t}^2 \rangle}{\langle v_2^2 \rangle}$ , is the ratio between the point velocity of the trim panel at the isolator location  $\langle v_{4t}^2 \rangle$  and the mean square velocity of the skin panel  $\langle v_2^2 \rangle$ .  $Zp_i$  is the plate's driving point impedance, given by  $Zp_i = \frac{2m_i}{\pi n_i}$  for a flat plate.

The ratio  $\vartheta$  is derived from a four-pole modelling of the structural connection [62, 145] and is given by:

$$\vartheta = \left| \frac{Z_{p2}}{T_{22}Z_{p2} + T_{11}Z_{p4} + j\omega T_{21}Z_{p2}Z_{p4} + \frac{T_{12}}{j\omega}} \right|^2. \quad (5.13)$$

$T_{ii}$  are the terms of the four-pole transfer matrix of the isolator, which is given by Eq. (5.14) in the case of an isolator of mass  $M_m$  modelled as an axial mass-spring-mass system with the total mass divided by two at each side of the spring of complex stiffness  $K^* = K(1 + j\eta_m)$ , where  $\eta_m$  is the damping loss factor of the isolator:

$$T = \begin{bmatrix} 1 - \frac{M_m\omega^2}{2K^*} & -M_m\omega^2 \left(1 - \frac{M_m\omega^2}{4K^*}\right) \\ \frac{1}{K^*} & 1 - \frac{M_m\omega^2}{2K^*} \end{bmatrix}. \quad (5.14)$$

The ratio  $\vartheta$  is simplified to  $\vartheta = \left| \frac{Z_{p2}}{Z_{p2} + Z_{p4}} \right|^2$  when a massless rigid link (having  $K^* = \infty$ ) is placed between panels.

$\eta_{15}$  represents the low frequency non-resonant coupling linking the source and receiver cavities. It represents the system, which behaves as an equivalent non-resonant single wall moving in phase, for frequencies lower than the double-wall decoupling frequency [35], given by:

$$f_D = \frac{1}{2\pi} \sqrt{\frac{\rho_0 c_0^2 (m_1 + m_2)}{(h_p + h_f) m_1 m_2}}. \quad (5.15)$$

In this equation  $m_1$ ,  $m_2$ ,  $h_p$  and  $h_f$  denote the mass of panels 1 and 2 and the thickness of porous and the fluid layers, respectively. When a layer of porous material is present in the cavity, the terms  $\rho_0$  and  $c_0$  are modified by the properties of the porous material [5].

Finally, a further assumption is made that no coupling exists between the source cavity and the trim panel  $\eta_{14} = 0$ , and between the skin panel and the receiver cavity  $\eta_{25} = 0$ .

### Transfer path analysis

The transfer path analysis is a powerful tool to determine dominant transmission paths and consequent noise control treatment solutions. In this paper, it is performed based on the approach developed by Craik [68]. It consists of defining all possible one-way transmission paths from the source cavity to the receiver cavity, shown in Fig. 5.2. The

total transmission loss of the double-wall under diffuse field excitation is then assumed to be the sum of the contribution of a combination of 6 independent paths, represented in Fig. 5.3.

The Transmission loss of each transmission path is calculated, using Eq. (5.3) and Eq. (5.4), where the ratio between the energy of two subsystems is given by [68]:

$$\frac{E_z}{E_a} = \frac{\eta_{ab}\eta_{bc}\eta_{cd}\dots\eta_{yz}}{\bar{\eta}_b\bar{\eta}_c\bar{\eta}_d\dots\bar{\eta}_z}. \quad (5.16)$$

Here,  $\eta_{ab}$  is the coupling loss factor between subsystems  $a$  and  $b$  and  $\bar{\eta}_b = \eta_{bb} + \sum_{i \neq b} \eta_{bi}$  is the total loss factor of subsystem  $b$ .  $\eta_{bb}$  is the internal loss factor of subsystem  $b$ .

The energy ratio between the source and receiver cavities is given in table 5.1 for each transmission path.

Table 5.1 Energy ratio between source and receiver cavity for each transmission path.

$\frac{E_5}{E_1} = \frac{\eta_{15}}{\bar{\eta}_5}$ path 1-5	$\frac{E_5}{E_1} = \frac{\eta_{13}\eta_{35}}{\bar{\eta}_3\bar{\eta}_5}$ path 1-3-5	$\frac{E_5}{E_1} = \frac{\eta_{12}\eta_{34}\eta_{45}}{\bar{\eta}_2\bar{\eta}_4\bar{\eta}_5}$ path 1-2-4-5
$\frac{E_5}{E_1} = \frac{\eta_{12}\eta_{23}\eta_{34}\eta_{45}}{\bar{\eta}_2\bar{\eta}_3\bar{\eta}_4\bar{\eta}_5}$ path 1-2-3-4-5	$\frac{E_5}{E_1} = \frac{\eta_{12}\eta_{23}\eta_{35}}{\bar{\eta}_2\bar{\eta}_3\bar{\eta}_5}$ path 1-2-3-5	$\frac{E_5}{E_1} = \frac{\eta_{13}\eta_{34}\eta_{45}}{\bar{\eta}_3\bar{\eta}_4\bar{\eta}_5}$ path 1-3-4-5

The 6 possible transmission paths are regrouped into 4 different physical contributions to the total transmission through the double-wall:

- **Double-wall non-resonant transmission:** the non-resonant transmission of the panels in a double-wall configuration (double-wall mass law) , directly linking the source and receiver cavities. It is represented by path 1-5. The non-resonant transmission coefficient is computed using the transfer matrix method for a multilayer composed of the skin panel’s mass, the porous layer, the air gap and the trim’s mass. It is included in the double-wall modelling in order to capture the transmission near the double-wall decoupling frequency. Since the method used to compute this path also contains contributions of the path 1-3-5, it is arbitrarily set to zero for frequencies higher than  $2f_D$ , where this later path is believed to be dominant.
- **Trim non-resonant transmission:** the non-resonant transmission through the trim panel (single-wall mass law) due to excitation via the inner cavity. It corresponds to

the sum of paths 1-3-5 and 1-2-3-5, including the mass-law and the radiating response of the skin panel, respectively.

- **Trim airborne radiation:** trim panel’s radiation due to airborne excitation of the inner cavity. It is given by the sum of paths 1-3-4-5 and 1-2-3-4-5, including the mass-law and the radiating response of the skin panel, respectively.
- **Trim structure-borne radiation:** trim panel’s radiation due to structure-borne excitation via mechanical links between panels, represented by path 1-2-4-5.

## 5.2.4 Description of the experiments

In this section, the dimensions and properties of the tested structures are presented. In addition, the transmission loss measurement procedure is outlined.

### Dimension and properties of the structures

Two double-wall structures are analysed in this paper. They are composed of an aluminium or composite (carbon fibre reinforced plastic) skin panel, a glass wool blanket, an air gap and a sandwich honeycomb trim panel. The panels are attached either by rigid elements or vibration isolators. They are separated by an anechoic and a reverberant cavity and have a surface area equal to 1.5 m<sup>2</sup>.

The aluminium panel is orthogonally stiffened and the composite panel is vertically stiffened. Their properties are given in table 5.2. Details on the location of the stiffeners are given in Fig. 5.4 for the aluminium case and in Fig. 5.5 for the composite case.

The panels are coupled via 6 structural links, as shown in Fig. 5.4 and Fig. 5.5 for the composite and aluminium skin panel, respectively. The rigid coupling configuration considers aluminium beams with a circular cross section having a 1 cm diameter in the composite panel case. For the aluminium skin, coupling is done via vertical stiffeners of the aluminium panel, representing the frames of an aircraft structure. The soft coupling configuration considers vibration isolators (trim mounts supplied by LORD Corporation) placed between the rigid links and the composite skin panel or placed on stiffeners of the aluminium panel. Their dynamic stiffness is measured up to 2 kHz and interpolated up to 10 kHz [145].

A 4-inches thick inner cavity separates the two panels. It is filled with a 2-inches thick porous material lined with the skin panel. Its properties are given in table 5.3. The properties of the sandwich honeycomb trim panel are given in table 5.4.

The damping loss factor of the panels are estimated using the decay rate method [53]. Tests were conducted with the panels placed on the measurement window. In consequence edge damping is accounted for. The excitation is performed using an electro-mechanical shaker and results are averaged over 3 random excitation locations and 15 randomly located points over the panel surface.

The modal densities are computed theoretically using the formulation presented in section 5.2.3. Their radiation efficiency are either obtained using the Leppington approach [143] or determined experimentally using a SEA-based technique in which the panel is freely hanged in a reverberant room:

$$\sigma = \frac{1}{2} \left( \frac{n_2 \eta_2 E_2}{n_2 E_1 - n_1 E_2} \right) \frac{\omega m_1}{\rho_0 c_0 A_1}. \quad (5.17)$$

Here, indexes 1 and 2 refer to the panel and to the reverberant room respectively. The energy of the panel is computed from its mean quadratic velocity  $\langle v_1^2 \rangle$ , using the relation  $E_1 = m_1 A_1 \langle v_1^2 \rangle$ . The energy of the room is obtained from its mean quadratic pressure  $\langle p_2^2 \rangle$ , using  $E_2 = \frac{\langle p_2^2 \rangle V_2}{\rho_0 c_0^2}$ . The room damping loss factor  $\eta_2$  is calculated from the measurement of the room reverberation time.

Table 5.2 Skin panels properties.

	Aluminium	Laminate
Thickness $h$ [m]	0.002	0.00275
Material density $\rho$ [kg.m <sup>-3</sup> ]	2742	1600
Young's modulus [GPa]	$E = 69$	$E_1 = 135, E_2 = 8.5$
Poisson ratio $\nu$	0.33	0.35

Table 5.3 Porous material properties.

	Porous
Thickness $h_p$ [m]	0.0508
Material density $\rho_t$ [kg.m <sup>-3</sup> ]	9.61
Porosity $\phi$	0.97
Airflow resistivity $\sigma$ [N.s.m <sup>-4</sup> ]	26557
Tortuosity $\alpha_\infty$	1.07
Viscous charac. length $\Lambda$ [m]	6.41x10 <sup>-5</sup>
Thermal charac. length $\Lambda'$ [m]	9.85x10 <sup>-5</sup>

Table 5.4 Receiving sandwich panel properties.

	Sandwich	
	Skin	Core
Thickness $h_i$ [m]	0.0005	0.0117
Material density $\rho_i$ [kg.m <sup>-3</sup> ]	2838	48
Young's modulus $E_i$ [MPa]	21180	0.1
Shear modulus $G_{12}$ [Mpa]	4000	-
Shear modulus $G_{13}$ [Mpa]	-	44
Shear modulus $G_{23}$ [Mpa]	-	25
Poisson ratio $\nu_{12}$	0.0667	0.01

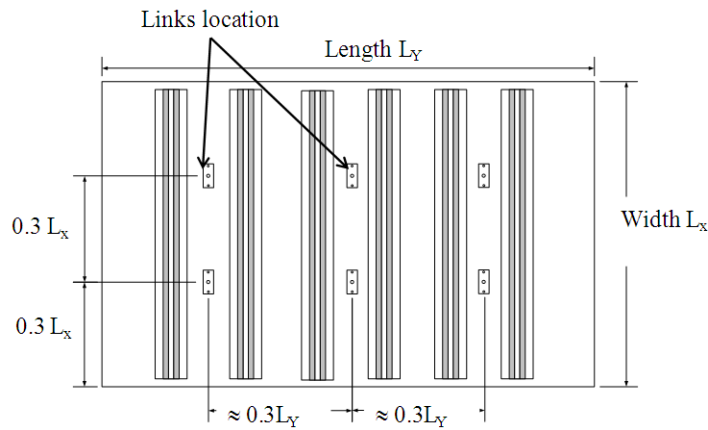


Figure 5.4 Composite stiffened panel: dimensions and links location.

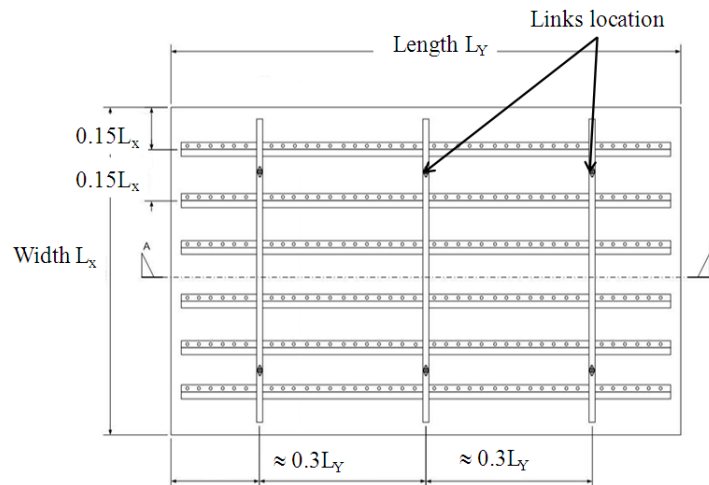


Figure 5.5 Aluminium stiffened panel: dimensions and links location.

### Transmission loss tests

The TL measurement follows ISO 15186-1 standard [144]. The structure is fixed between a reverberant and an anechoic room using a mounting frame. Joints between the panels and the frame are sealed using silicon and aluminium tape. The edges of the panels are sandwiched between two flat bars with a neoprene decoupler. A white-noise in the frequency range of 100 Hz to 10 kHz is generated in the reverberant room. The diffuse field low-frequency limit of the reverberation room is 200 Hz. The transmission loss of the structure is given by:

$$TL = (L_p - L_I - 6). \quad (5.18)$$

$L_p$  is the average sound pressure level in the source room, measured by a rotating microphone.  $L_I$  is the averaged intensity level over the measurement surface in the receiving room. The measurement is done by manually scanning the surface of the sample,  $A_i$ , with the intensimetry probe in order to obtain a spatial and temporal average. In the following discussion, the results are presented in one third-octave bands.

## 5.2.5 Results and discussion

In this section, transmission loss predictions using the double-wall SEA model are compared with experimental results. The influence of vibration isolators is then analysed and compared to a case without links and to a connection via rigid elements. The airborne and structure-borne transmissions are identified and the dominant transmission paths are analysed in each frequency range. Finally, improvements of the double-wall transmission loss are suggested, based on the observed dominant transmission paths.

### Influence of the structural connection

Theoretical and experimental transmission losses (TL) of the double-wall with the aluminium skin panel are compared considering 3 structural coupling configurations between panels: (1) structurally decoupled (Fig. 5.6), (2) coupling via rigid elements (Fig. 5.7) and (3) coupling via vibration isolators (Fig. 5.8).

Overall, for the uncoupled configuration (Fig. 5.6), theory underestimates the measured transmission loss up to 400 Hz. At higher frequencies, theory overestimates the experimental transmission loss by about 7 dB. The main discrepancies between theoretical and experimental results have been traced to three factors: (1) the influence of the stiffen-

ers, which are not accounted for in the predictions of the panel's SEA parameters, such as the modal density and radiation efficiency. At low frequencies it leads to an increase of the experimental transmission loss due to an added-mass effect. When the bending wavelength of the panel is smaller than the distance between horizontal stiffeners (for frequencies higher than 400 Hz), the transmission loss is dominated by the response of panel sections delimited by the stiffeners [23]. Since the radiation of the smaller sub-panels is higher than that of larger panels, the transmission loss decreases. In addition, radiation from stiffeners is not entirely attenuated by the porous layer, reducing the measured transmission loss compared to the theoretical one. (2) The overestimation of the sandwich panel experimental transmission loss (in a single-wall configuration), increasing thus the theoretical transmission loss of the double-wall between 1 kHz and 3 kHz; (3) a difficulty in accurately estimating the damping loss factor of the panels in their critical frequency region.

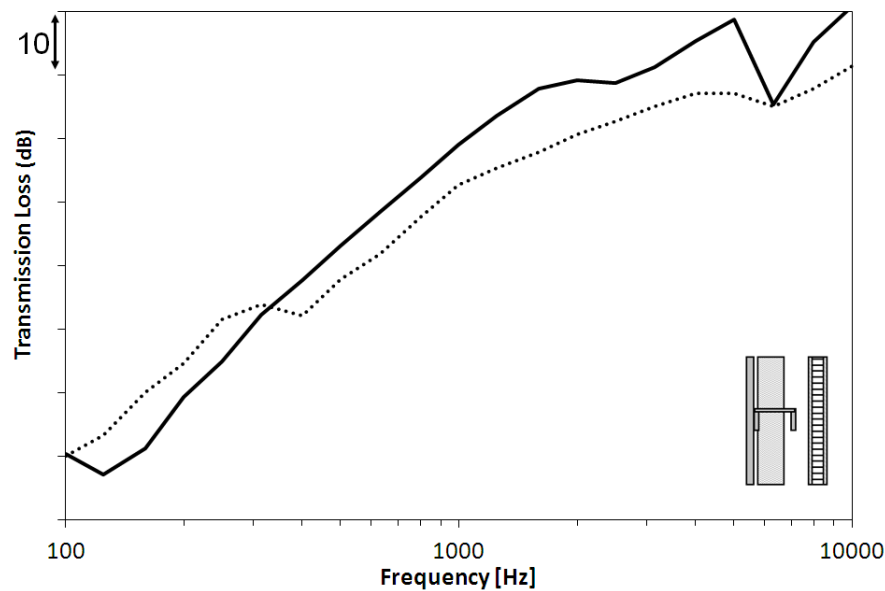


Figure 5.6 Transmission loss through the double-wall with the aluminium skin panel in a structurally decoupling configuration: — SEA and ..... measurements.

Results for the configuration where the skin panel is connected to the trim panel by rigid elements placed on vertical stiffeners are shown in Fig. 5.7. A first approach supposes that stiffeners also behave as rigid elements in the computation of the equivalent structural coupling using Eq. (5.12). This approach highly underestimates the transmission loss in the mid and high frequency ranges, showing the importance of accounting for the stiffeners dynamic response. Measured structural coupling loss factor, obtained from experimental

SEA results, is thus used in computations. A better agreement is obtained compared to the rigid stiffeners assumption.

Finally, results for the configuration where the panels are connected via vibration isolators placed on the vertical stiffeners of the skin panel are shown in Fig. 5.8. The structural coupling loss factor between panels is integrated using two approaches: (1) four-pole model, supposing that stiffeners act as rigid elements and the vibration isolator is the only resilient element between panels and (2) from experimental values. The assumption of rigid stiffeners in the four-pole model gives similar results as using experimental structural coupling loss factor. Stiffeners' dynamic contribution to the coupling loss factor increases when the dynamic stiffness of the isolators and stiffeners tend to be of the same order of magnitude. However, as shown in Fig. 5.8 for specific case the contribution is negligible when isolators are part of the connection (placed on stiffeners).

The accuracy of the model in assessing the influence of mechanical links is then addressed. Differences are presented between the transmission loss of an ideal uncoupled or a coupled via isolators double-wall, compared to a baseline rigid coupling configuration. Results are shown in Fig. 5.9 for the double-wall with the aluminium skin panel and in Fig. 5.10 for the composite skin panel.

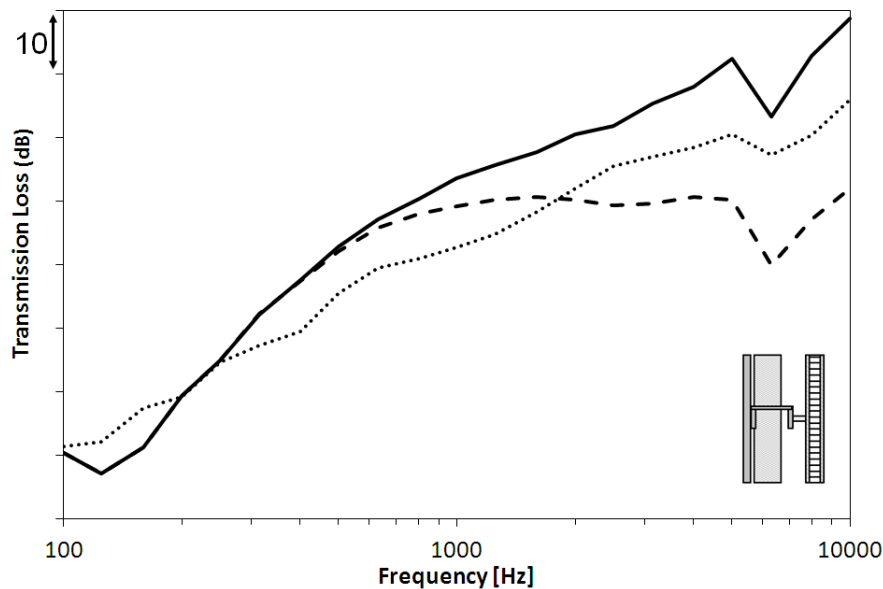


Figure 5.7 Transmission loss through the double-wall with the aluminium skin panel in a rigid coupling configuration: — SEA (dynamic stiffeners), - · - SEA (rigid stiffeners) and ···· measurements.

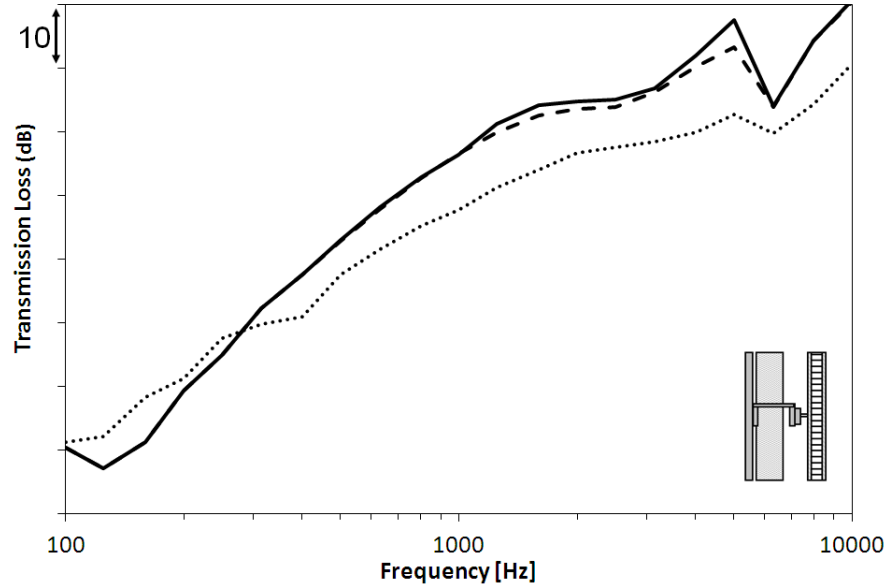


Figure 5.8 Transmission loss through the double-wall with the aluminium skin panel in a coupling via isolators configuration: — SEA (dynamic stiffeners), - · SEA (rigid stiffeners) and ···· measurements.

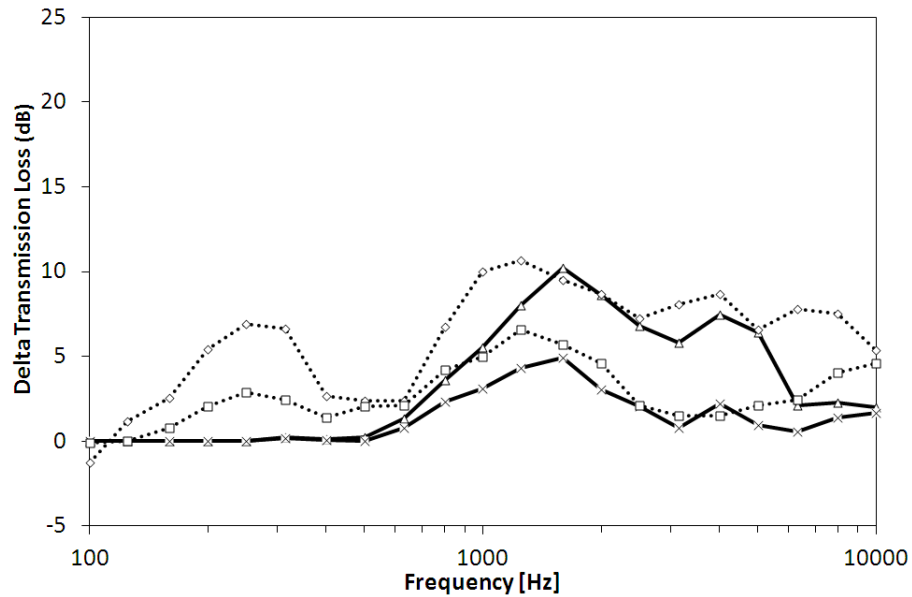


Figure 5.9 Theoretical and measured delta transmission loss of uncoupled or soft-coupled (via isolators) compared to a rigid-coupling configuration. Aluminium skin panel case. —△— Uncoupled - Rigid: SEA, -×- Soft - Rigid: SEA, ···· Uncoupled - Rigid: tests, ···· Soft - Rigid: tests.

For the first case (Fig. 5.9), all input parameters feeding the model are theoretical, except for the damping loss factor of the panels and the structural coupling loss factor via stiffen-

ers. The structural coupling loss factor via isolators is computed using the four-pole model assuming a mass of 6 g for the isolator. Experimental results show that isolators provide an acoustic benefit up to 5 dB in the mid-frequency range (around 1 kHz) compared to a rigid connection. In addition, an ideal uncoupled configuration is 10 dB higher than the rigid one in the same frequency region. Same trends are observed for the experimental and theoretical results between 600 Hz and 4 kHz. Good agreement between theory and measurements is obtained for the comparison between coupling via isolators and rigid coupling. It should be recalled that the model is not able to predict the TL of the double-wall at lower frequencies since stiffeners are not modelled. At frequencies higher than 4 kHz, the results are highly influenced by the damping of the skin panel, which is subjected to high uncertainties in the vicinity of the critical frequency of the skin panel. The agreement between theory and tests is further improved when the measured modal densities of the panels is integrated into the model (not shown for conciseness reasons).

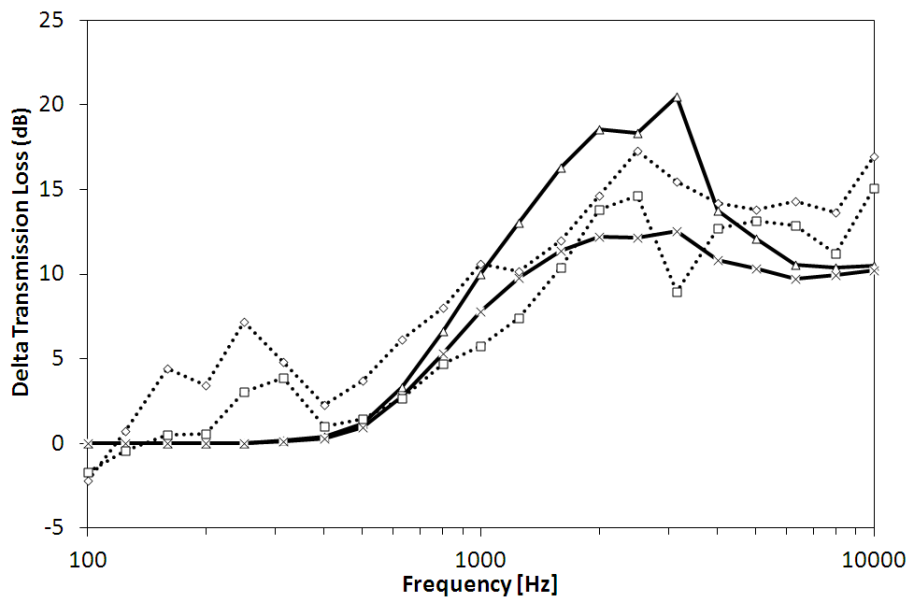


Figure 5.10 Theoretical and measured delta transmission loss of uncoupled or soft-coupled (via isolators) compared to a rigid-coupling configuration. Composite skin panel case.  $\blacktriangle$  Uncoupled - Rigid: SEA,  $\times$  Soft - Rigid: SEA,  $\diamond$  Uncoupled - Rigid: tests,  $\square$  Soft - Rigid: tests.

In the second case (Fig. 5.10), all input parameters of the model are theoretical except for the damping loss factor of the panels. The structural coupling between panels via studs and via isolators is computed using the four-pole modelling. For the connection via studs, a rigid dummy replaces the isolators and its estimated mass of 20 g is used in the computation. Similar conclusions to the first case can be drawn, showing that the

model is able to predict the effect of mechanical links. In addition, when experimental structural coupling loss factor is used in the model, similar delta results are obtained in the mid-frequency range, validating the theoretical approach. Since the structural elements connect directly the skin of each panel, the structural transmission path is more important than in the aluminium skin case, in which the isolators are placed on stiffeners. Indeed, a difference of about 17 dB is found between an uncoupled configuration and a connection via studs in the mid-frequency range. Moreover, isolators provide in this configuration an acoustic benefit of about 14 dB in the mid-frequency range. Finally, one limitation of the four-pole model is observed at 3 kHz, where a resonance of the double-wall appears due to the presence of isolators. The model is not able to capture this resonance since the dynamic stiffness of the isolators is obtained in the frequency range between 800 Hz and 2 kHz and is then linearly extrapolated up to 10 kHz.

### Transmission path decomposition

The contribution of each transmission path to the total TL of the double-wall is addressed in this section using the method presented in section 5.2.3. Results for the aluminium skin in an uncoupled configuration, as well as for the rigid coupling and for the coupling via isolators are shown in Fig. 5.11 to Fig. 5.13, respectively.

For all configurations, the non-resonant path of the double-wall is dominant around 125 Hz, the double-wall decoupling frequency region, which is given by eq. (5.15). This frequency is not observed in experimental curves in Fig. 5.11 to Fig. 5.13 due to the added-mass effect of the stiffeners. For the uncoupled configuration (Fig. 5.11), the non-resonant transmission through the trim plays an important role in the transmission up to the critical frequency region of the trim panel (around 2500 Hz). From 1 kHz to 4 kHz the trim's radiation due to airborne excitation via the inner cavity (path 1-3-4-5) dominates the transmission. At higher frequencies the direct path 1-2-3-4-5, accounting for the airborne radiation of the skin panel is the main transfer path (these two contributions are regrouped in the airborne radiation path).

It is observed for the rigid structural coupling configuration (Fig. 5.12) that the structure-borne path (1-2-4-5) dominates mainly in the mid frequency region, where it is responsible for the total transmission loss of the double-wall. At higher frequencies the transmission loss is governed by radiation contributions of the structure-borne and the airborne paths.

In the coupling via isolators configuration (Fig. 5.13), the structural transmission is also the main contributor in the mid-frequency range but, due to the isolation provided by the mounts, this path is more attenuated compared to the rigid configuration. Moreover,

its contribution decreases at high frequencies and only the radiation due to the airborne excitation dominates.

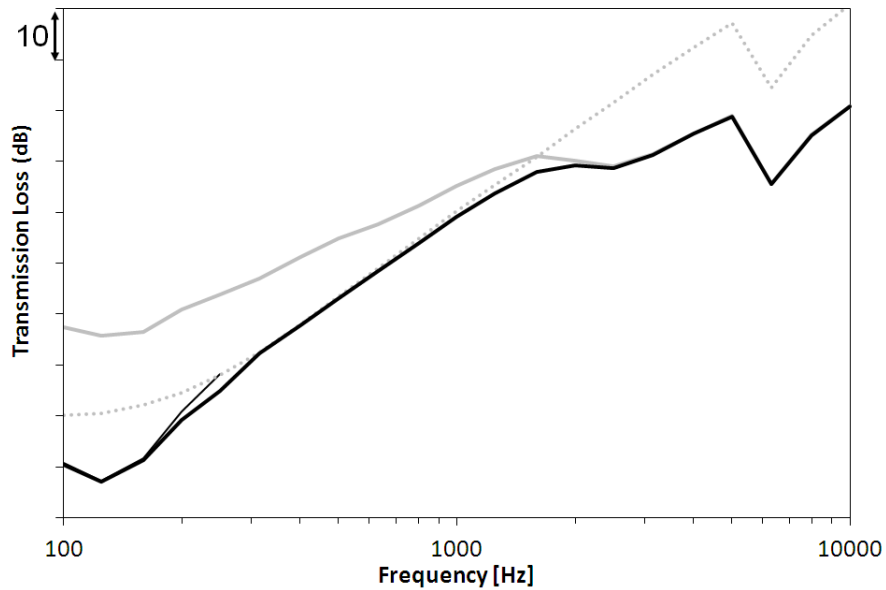


Figure 5.11 Theoretical transmission loss contributions of each transmission path: aluminium skin, uncoupled configuration. — double-wall non-resonant transmission, ..... trim non-resonant transmission, — trim airborne radiation, — total.

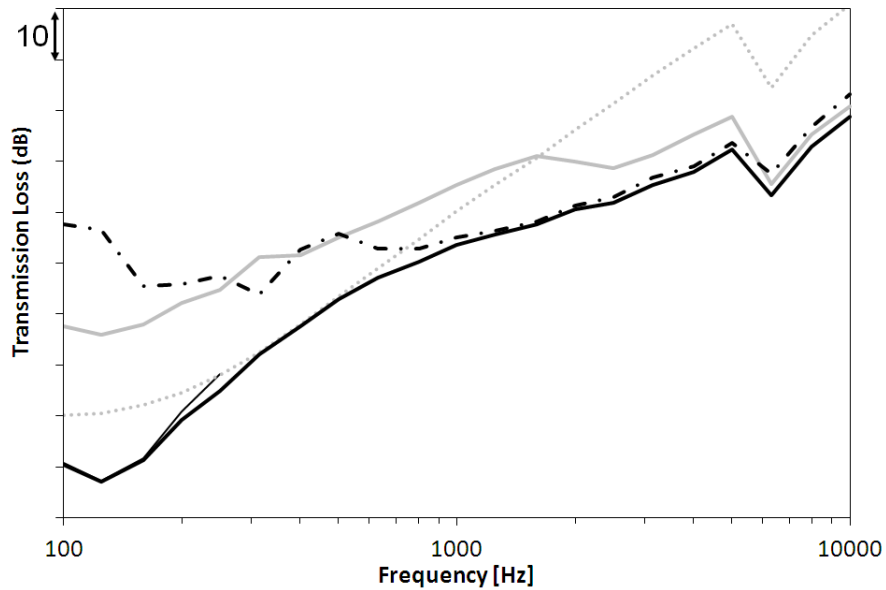


Figure 5.12 Theoretical transmission loss contributions of each transmission path: aluminium skin, rigid coupling configuration. — double-wall non-resonant transmission, ..... trim non-resonant transmission, — trim airborne radiation, - · trim structure-borne radiation, — total.

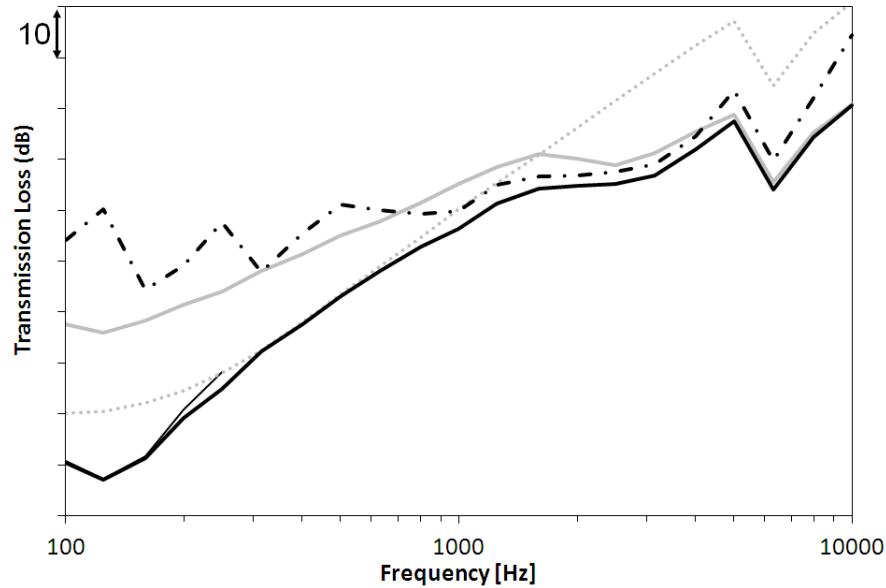


Figure 5.13 Theoretical transmission loss contributions of each transmission path: aluminium skin, coupling via isolators configuration. — double-wall non-resonant transmission, ..... trim non-resonant transmission, — trim airborne radiation, - · trim structure-borne radiation, — total.

Transfer path analysis results for the double-wall with the composite skin panel are shown in Fig. 5.14 to Fig. 5.16 for the uncoupled, rigid coupling and coupling via isolators, respectively. Similar trends are obtained compared with the aluminium skin panel. However, in a rigid coupling configuration, the structure-borne path has a higher transmission contribution in comparison to the other paths and in comparison with the aluminium skin case. This explains the differences in levels observed for the two cases in terms of Delta TL (Fig. 5.9 and Fig. 5.10). Moreover, the structure-borne path via the isolators has different contributions depending on the double-wall studied (with aluminium or composite skin panel), putting in evidence the fact that the efficiency of isolators depend on the entire double-wall assembly characteristics [146].

The transfer path analysis helps the decision between different solutions in terms of noise control treatments to increase the transmission loss of the double-wall. While for the structurally decoupled double-wall, having a porous material with better acoustic properties will lead to an increase of the transmission loss in the entire frequency range, for the case with isolators, the increase will be limited to the mid frequency range, where the structure-borne transmission dominates. For the rigid coupling configuration, this solution would be inefficient in the mid-frequency range, since the structure-borne transmission is

the only contributor to the TL. It would also have a limited impact in the high-frequency range due to the structure-borne portion of the transmission.

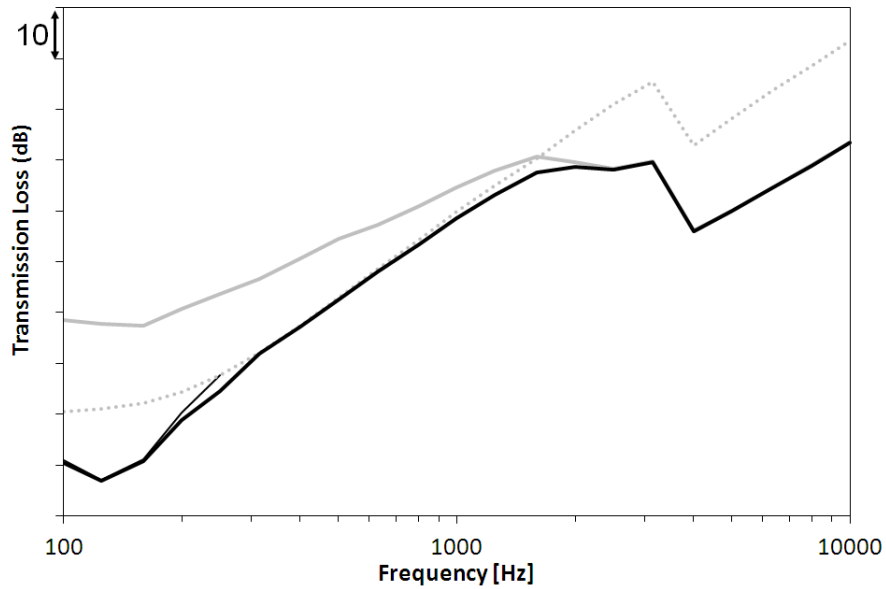


Figure 5.14 Theoretical transmission loss contributions of each transmission path: composite skin, uncoupled configuration. — double-wall non-resonant transmission, ..... trim non-resonant transmission, — trim airborne radiation, — total.

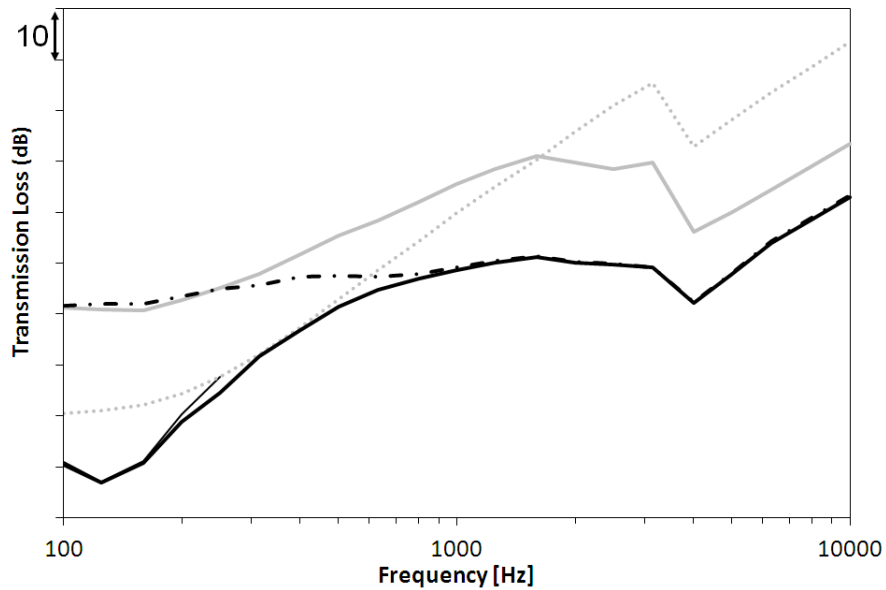


Figure 5.15 Theoretical transmission loss contributions of each transmission path: composite skin, rigid coupling configuration. — double-wall non-resonant transmission, ..... trim non-resonant transmission, — trim airborne radiation, - · trim structure-borne radiation, — total.

In order to increase the TL at low frequencies, near the double-wall decoupling frequency, an increase of the mass of the panels and of the inner cavity thickness are the main driver parameters, according to Eq. (5.15). Employing isolators with softer dynamic stiffness would lead to an increase of the TL mainly in the mid- and high-frequency range. Results of eliminating this path will lead to the ideal case of a structurally-decoupled double-wall TL (Fig. 5.11 and Fig. 5.14). Finally, increasing the damping of the panels will have mainly two impacts in the TL: (1) a decrease of the radiation via airborne paths, i.e. in the critical frequency region of the panels, (2) a decrease of the mean square velocity of the panels and consequently of the coupling via the structure-borne path.

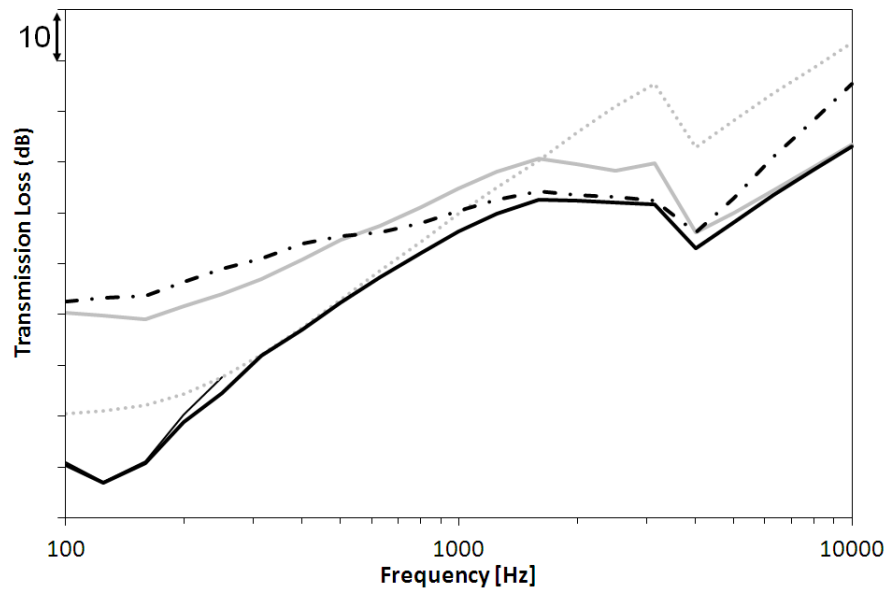


Figure 5.16 Theoretical transmission loss contributions of each transmission path: composite skin, coupling via isolators configuration. — double-wall non-resonant transmission, ..... trim non-resonant transmission, — trim airborne radiation, - · - trim structure-borne radiation, — total.

## 5.2.6 Conclusion

The effect of rigid coupling or coupling via vibration isolators on the double-wall transmission loss of aircraft panels is investigated in this paper. SEA results are compared with measurements for two sets of double-walls. The model allows the prediction of the benefit in terms of TL of fully decoupling a double-wall or of applying vibration isolators on the structural connection between panels. The benefit of decoupling elements is found maximum in the mid-frequency range (around 1 kHz). Good agreement is obtained between 400 Hz and the skin panel's critical frequency region. Low frequency limitations are linked to the fact that stiffeners are not included in the SEA modelling. At and above the

critical frequency of the skin panel, measurements of the panel's damping loss factor are subjected to high variability, which is propagated to the TL predictions.

Decoupling via isolators leads to an increase of about 14 dB in the TL compared to a direct connection between the skins of the panels. For a more realistic connection, in which isolators are mounted on the stiffeners of the skin panel, the decoupling results in an increase of about 5 dB in the TL. This latter result shows the influence of stiffeners as part of the structural connection. Their dynamic behaviour should be taken into account in order to obtain accurate predictions of the structural coupling loss factor between panels and consequently the transmission loss of the double-wall.

Finally, a transfer path analysis shows that up to the double-wall decoupling frequency (around 125 Hz), the contribution of the non-resonant path representing the transmission of a single-wall with equivalent mass is dominant. Then, the non-resonant transmission through the trim panel plays an important role in the transmission up to the bridge frequency (around 1 kHz), from which structural transmission is preponderant. It is clearly observed that the structure-borne path is attenuated by the presence of the isolators compared to a rigid coupling configuration. At the critical frequency of the skin panel and above, the radiation of the trim due to the airborne excitation via the inner cavity dominates. Being so, the improvement of the double-wall transmission loss may be achieved by attenuating in parallel both airborne and structure-borne transmission paths, e.g. by employing isolators with softer dynamic stiffness and more efficient porous materials.

It should be recalled that contributions of structure-borne and airborne transmissions depend on the excitation field. Therefore, a transfer path analysis under more representative excitation fields, such as the turbulent boundary layer, should be performed on the framework of optimising noise control treatments for an aircraft double-wall under flight conditions.

## Acknowledgements

Maxime Bolduc and Patrick Levesque, from University of Sherbrooke, are acknowledged for their technical assistance. Lord Corporation is also acknowledged for contributing materials used in experiments.

## 5.3 Double-wall SEA modelling under structural excitation (uncorrelated point forces)

### Description of the model

The double-wall SEA model under structural excitation is shown in Fig. 5.17. The same notations of the case under diffuse acoustic field are kept here, with subsystem 2 representing the skin panel, subsystem 3 the inner cavity and subsystem 4 the trim panel. Since the power is injected directly to the skin panel, the modelling of a source cavity is not necessary. Moreover, assuming that the trim panel radiates towards a semi infinite medium, there is no need to model a reception cavity. In order to account for radiation losses from each panel towards the outer media, the radiation loss factor of the panels is added to the internal damping loss factor. The direct losses from the inner cavity to the outer media (representing the non resonant transmission of the trim panel) are also added to its damping loss factor.

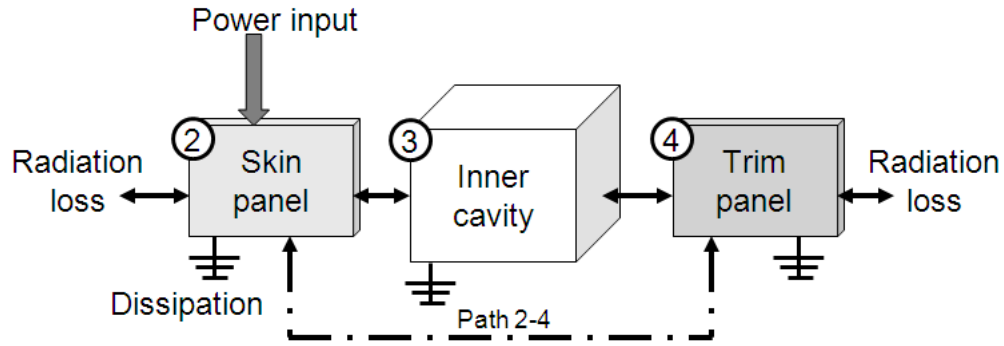


Figure 5.17 SEA representation of the double-wall system under structural excitation.

The SEA matrix under structural excitation, keeping the same notations described in the paper presented in this chapter is:

$$\begin{bmatrix} \eta_{22} + \sum_{i \neq 2} \eta_{2i} & -\eta_{32} & -\eta_{42} \\ -\eta_{23} & \eta_{33} + \sum_{i \neq 3} \eta_{3i} & -\eta_{43} \\ -\eta_{24} & -\eta_{34} & \eta_{44} + \sum_{i \neq 4} \eta_{4i} \end{bmatrix} \begin{bmatrix} E_2 \\ E_3 \\ E_4 \end{bmatrix} = \begin{bmatrix} \frac{\Pi_2}{\omega} \\ 0 \\ 0 \end{bmatrix}. \quad (5.19)$$

$\Pi_2$  is the power injected by the uncorrelated point forces ( $F$ ), given by:

$$\Pi_2 = \frac{|F^2|}{2} \frac{\pi}{2m_2 A_2} n(\omega). \quad (5.20)$$

The two vibroacoustic indicators studied are (1) the vibration transmissibility ( $VT$ ), given by eq. (5.21) and representing the logarithm ratio between the mean quadratic velocity of the trim and the skin panels ( $\langle v_4^2 \rangle$  and  $\langle v_2^2 \rangle$ , respectively); and (2) the ratio between transmitted and injected powers in dB, denoted AMCE (Acoustic/Mechanical conversion efficiency) and given by eq. (5.22).

$$VT = 10 \log_{10} \left( \frac{\langle v_4^2 \rangle}{\langle v_2^2 \rangle} \right). \quad (5.21)$$

$$AMCE = 10 \log_{10} \left( \frac{1}{\tau} \right), \quad (5.22)$$

$\tau = \frac{\Pi_{rad}}{\Pi_{inj}}$ ,  $\Pi_{inj}$  is the power injected to the skin panel and  $\Pi_{rad}$  is the power transmitted by the trim panel. It is computed from the sum of the contributions of transmission paths shown in Fig. 5.18 and defined as follows:

Path  $DWL(nr)$ : represents the non-resonant transmission of the double-wall, comprising the non-resonant transmission of a single-wall with equivalent mass (path 1) and the non-resonant transmission of each panel ( with coefficients  $\tau_{2(nr)}$  and  $\tau_{4(nr)}$ ). This path is computed independently using the transfer matrix method, by modelling the panels as rigid masses and the excitation as an imposed velocity (piston motion).

Path  $\tau_{2(nr)}\tau_{4(r)}$ : the radiation of the trim panel (with coefficient  $\tau_{4(r)}$ ) due to non-resonant transmission of the skin panel. The power transmitted by this path ( $\Pi_{2(nr)4(r)}$ ) is obtained from the following power balance relation:

$$\Pi_{2(nr)4(r)} = \omega \eta_{4(r)} E_{4\_2(nr)4(r)}. \quad (5.23)$$

where,  $\eta_{4(r)}$  is the radiation loss factor of the trim panel,  $E_{4\_2(nr)4(r)}$  is the portion of trim's energy due to this transmission path. This energy is computed from the following power balance relation:  $E_{4\_2(nr)4(r)} = \frac{\Pi_{inj(2(nr)4(r))}}{\omega \bar{\eta}_4}$ .  $\Pi_{inj(2(nr)4(r))} \omega \bar{\eta}_4$  is the power injected to the receiving panel due to this transmission path and is obtained from the following power balance relation:  $\Pi_{inj(2(nr)4(r))} = \omega \eta_{34} E_{3\_2(nr)}$ .  $E_{3\_2(nr)}$  is the portion of inner cavity's energy due to the non-resonant transmission through the skin panel. This energy

is obtained using the following formulation: ( $E_{3\_2(nr)} = \tau_{2(nr)}\Pi_{inj(p)}$ ).  $\Pi_{inj(p)}$  is the power injected when the skin is driven by a velocity spectrum (piston motion)  $\langle v_2^2 \rangle$ , assumed:

$$\langle v_2^2 \rangle = \frac{\Pi_2}{\omega\eta_{22}m_2A_2}. \quad (5.24)$$

Path  $\tau_{2(st)}\tau_{4(r)}$ : represents the radiation of the trim panel due to structure-borne excitation via links ( $\tau_{2(st)}$ ).

Path  $\tau_{2(r)}\tau_{4(nr)}$ : represents the radiation from the skin panel ( $\tau_{2(r)}$ ) and non-resonant transmission of the trim panel. The non-resonant transmission through the trim panel is obtained from its mass-law under normal incidence plane wave excitation.

Path  $\tau_{2(r)}\tau_{4(r)}$ : represents the direct path through radiation from both skin and trim panels.

The last three paths are computed from the transfer path analysis proposed by Craik [68] and explained in the paper presented in this chapter. It should be noted that this transfer path analysis is equivalent to the solution of eq. (5.19) when return paths are neglected.

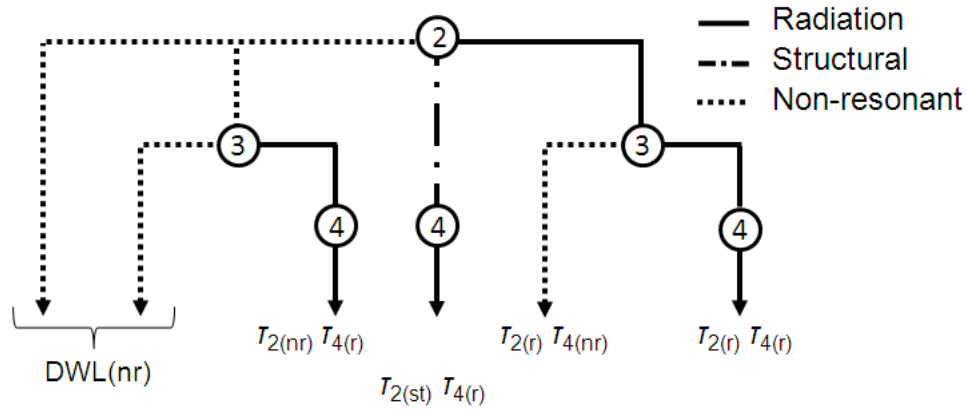


Figure 5.18 Sound transmission paths of the double-wall SEA system. 2- skin panel, 3-inner cavity, 4-trim panel.

Finally, using the relations above and the transfer path analysis, the ratio  $\tau$  is given by:

$$\tau = \frac{1}{\Pi_2} \left( \tau_{DWL(nr)}\Pi_{inj(p)} + \tau_{2(nr)}\Pi_{inj(p)} \frac{\eta_{34}\eta_{4(nr)}}{\eta_3\eta_4} + \omega\eta_{4(r)} \frac{\eta_{24}}{\eta_4} E_2 + \omega\eta_{4(nr)} \frac{\eta_{23}}{\eta_3} E_2 + \omega\eta_{4(r)} \frac{\eta_{23}\eta_{34}}{\eta_3\eta_4} E_2 \right),$$

where  $\eta_{4(nr)}$  is the non-resonant coupling loss factor through the trim panel's mass-law.

## Validation of the model for a simple double-wall

In order to determine the accuracy and limits of the developed SEA model, vibration transmissibility and AMCE results for a simple double-wall are compared with FEM simulations using GAUS's in-house NOVAFEM software. The double-wall is composed of an unstiffened 2 mm aluminium panel, 2 in. of glass-wool, 2 in. air gap and an unstiffened 3 mm aluminium panel. Panels and porous materials properties are the same defined in the paper above. In addition, results of the transfer matrix method with finite-size correction (FTMM) are also compared. The TMM model description is given in the paper above. The implementation of the rain-on-the-roof excitation in the TMM formulation is explained in [5].

The NOVAFEM model has a total of 64528 nodes. The plates are modelled using isotropic thin shell theory and the surface is meshed using linear quadrangular elements of 14.3 mm lateral size. The boundary conditions are simply supported and the structure is immersed in air and inserted in a rigid baffle. For the inner cavity, linear hexahedral elements are used, having a thickness of 12.7 mm. The porous layer is modelled using the limp frame theory. The excitation is a point force of unit magnitude, placed at three different locations. Results, computed for each excitation location, are then averaged in order to simulate a rain-on-the-roof excitation. The indicators are computed at 315 frequency points between 100 Hz to 5 kHz using a logarithm step and averaged in one-third octave bands.

Fig. 5.19 shows FTMM, SEA and FEM vibration transmissibility results. SEA results are split into non-resonant and resonant contributions. The first is computed using path  $DWL(nr)$  and the second is computed from the resonant response of the receiving panel (paths  $\tau_{2(nr)}\tau_{4(r)}$  and  $\tau_{2(r)}\tau_{4(r)}$ ). Good agreement is obtained between FEM and SEA results. In addition, it can be observed that the vibration transmissibility is driven by the non-resonant contribution, up to the coincidence region of the panels, at which resonant transmission dominates. Finally, TMM results underestimate FEM, implying that part of the transmission is not captured by this approach. Classical SEA (solution of eq. (5.19)) also does not capture this path. It is the added non-resonant path (piston driven skin panel) that allows for this good agreement.

AMCE results of the double-wall are shown in Fig. 5.20. While SEA correctly predicts the FEM vibration transmissibility, it underestimates FEM AMCE results. This issue is to be investigated. It is due to the assumption made in order to compute the magnitude of the imposed velocity (eq. (5.24)) and consequently its injected power ( $\Pi_{inj(p)}$ ). Moreover,

TMM results overestimate the double-wall AMCE, corroborating the conclusion that part of the sound transmission is not well represented in this approach.

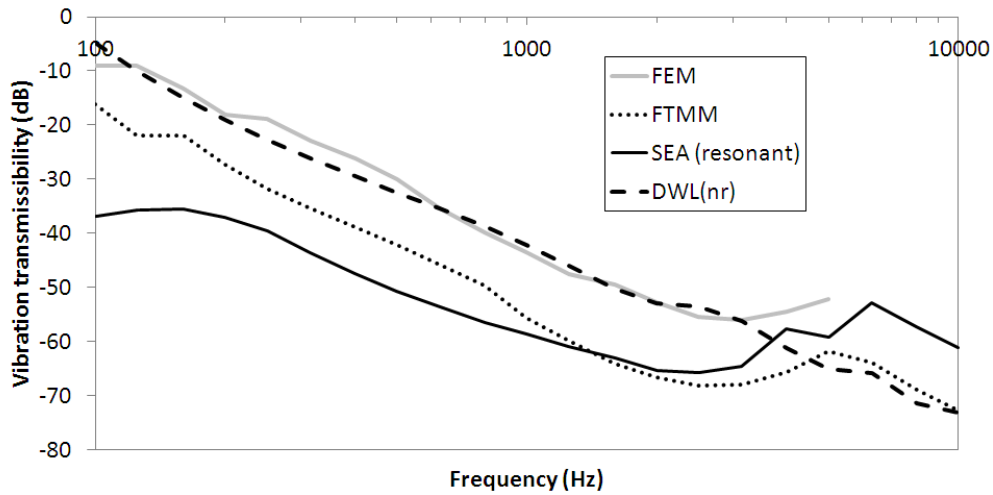


Figure 5.19 Vibration transmissibility of the double-wall composed of a 2 mm unstiffened panel, 2 in. of glass wool, 2 in. of air gap and a 3 mm aluminium panel: comparisons between FEM, TMM and SEA.

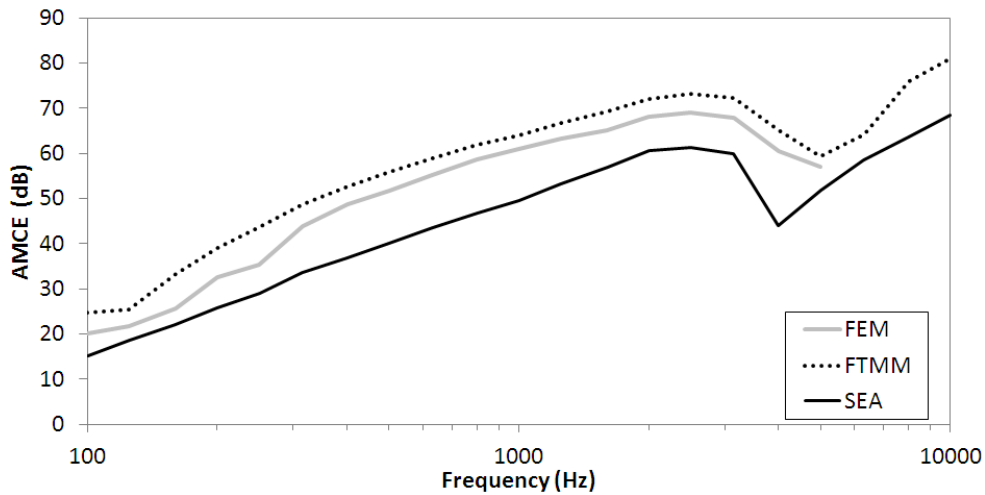


Figure 5.20 AMCE of the double-wall composed of a 2 mm unstiffened panel, 2 in. of glass wool, 2 in. of air gap and a 3 mm aluminium panel: comparisons between FEM, TMM and SEA.

Finally, Fig. 5.21 shows results of the transfer path analysis for the double-wall AMCE. It can be concluded that the transmission is driven by path DWL(nr) up to the coincidence region of the 3 mm panel, at which its radiation dominates via the path  $\tau_{2(nr)}\tau_{4(r)}$ . From the coincidence region of the 2 mm panel on, the transmission path including its radiation ( $\tau_{2(r)}\tau_{4(r)}$ ) becomes also important. Moreover, contribution of the non-resonant transmis-

sion of the second panel, excited by the first panel radiation response ( $\tau_{2(r)}\tau_{4(nr)}$ ) is found negligible.

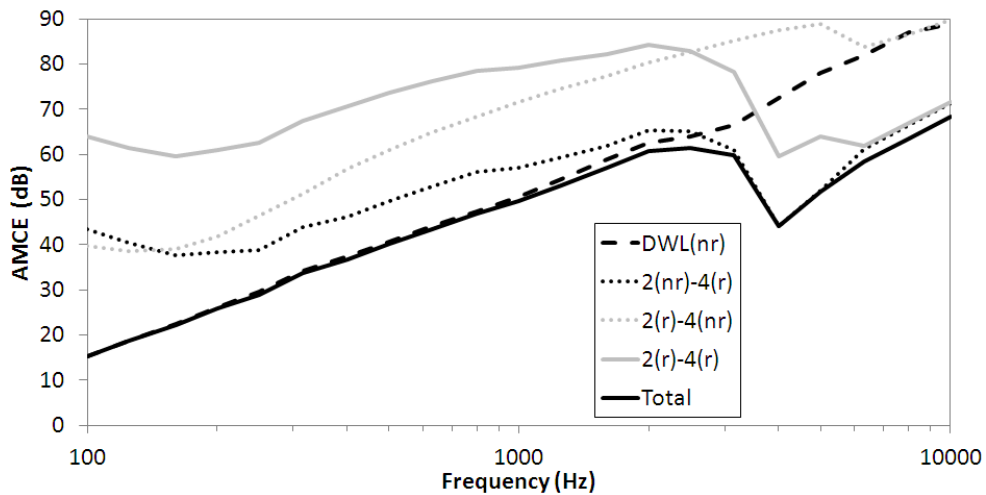


Figure 5.21 Transfer path analysis of the double-wall composed of a 2 mm unstiffened panel, 2 in. of glass wool, 2 in. of air gap and a 3 mm aluminium panel, using the SEA model.

## Validation of the model for aircraft double-walls

In this section, the aircraft double-walls analysed in the above paper are studied under structural excitation. Results of the SEA model are compared to FEM, FTMM and tests. The test procedure is described in the above paper, except that the excitation is provided by a shaker in the reverberant room at three random locations and the results are averaged over locations. Absorbing materials are placed in front of the skin panel in order to prevent coupling with the reverberation room.

The FEM geometry of the double-walls are shown in Fig. 5.22 and Fig. 5.23, for the system with the aluminium and laminate composite skin panels, respectively. FEM simulations are performed using the software Actran 12.0. In order to study the influence of the stiffeners, additional FEM results are obtained for the double-walls in the uncoupled configuration, without stiffeners, using GAUS's in-house NOVAFEM software (following mesh criteria described in previous section).

In the Actran FEM model, the panels are modelled using linear quadrangular elements. The spacing between nodes for the aluminium and the laminate composite skin panel is 10 mm in the x and y directions. The first is modelled using isotropic thin shell theory, the second is modelled using thin orthotropic shell theory. The porous layer is modelled using limp frame theory. For the inner cavity, the spacing between nodes in the thickness

direction is 10 mm. The trim skins are modelled as thin isotropic shells while the core is modelled as an orthotropic shell with one element in the thickness direction. The spacing between nodes in the x and y directions is 10 mm. The boundary conditions are clamped and the structure is immersed in air and inserted in a rigid baffle. The excitation is a point force of unit magnitude, placed at three different locations. Results, computed for each excitation location, are then averaged in order to simulate a rain-on-the-roof excitation. The indicators are computed at 50 frequency points between 100 Hz to 5 kHz using a logarithm step and averaged in one-third octave bands.

Vibration transmissibility results for the uncoupled double-wall with the aluminium skin panel are shown in Fig. 5.24. FEM (stiffened model) results are in good agreement with tests up to 2.5 kHz. Comparisons between FEM unstiffened and stiffened models show that stiffeners have a high influence on the results, from 200 Hz on. The SEA model agrees well with FEM (unstiffened results) such as observed in previous section. Moreover, TMM values underestimate FEM and experimental results.

AMCE results for the uncoupled double-wall with the aluminium skin panel are shown in Fig. 5.25. The same assumption made in previous section for the computation of the injected power from a imposed velocity is also made in this section. As in previous section, SEA results underestimate FEM results (considering an unstiffened skin panel). However, trends given by the SEA model are in agreement with FEM. Measurement results at high frequencies (7 kHz or higher) are subjected to high uncertainties due to limitations in injecting power to the structure via the shaker. Finally, TMM results overestimate FEM and experiments.

The transfer path analysis is shown in Fig. 5.26. A similar distribution of paths is obtained compared to the double-wall in the previous section (Fig. 5.21). The difference is that the coincidence region of the sandwich trim panel is broader than that of the 3 mm aluminium panel, therefore, path  $\tau_{2(nr)}\tau_{4(r)}$  dominates in a wider frequency range than in previous section.

Results for the rigid (via stiffeners) coupling configuration are analysed next. Structural coupling loss factor is accounted for experimentally for this configuration. Fig. 5.27 shows the AMCE of the double-wall and Fig. 5.28 shows the corresponding transfer path analysis. Overall, good agreement is obtained between SEA, FEM and tests. It is observed that structure-borne transmission dominates from 500 Hz up to 5 kHz (path  $\tau_{2(st)}\tau_{4(r)}$ ). Moreover, transmission through this path is higher than airborne radiation via the trim panel (path  $\tau_{2(nr)}\tau_{4(r)}$  and path  $\tau_{2(r)}\tau_{4(r)}$ ).

For a coupling via isolators (Fig. 5.29), the structural coupling loss factor is modelled via the four-pole approach. It can be observed that SEA results capture experimental trends. The transfer path analysis (Fig. 5.30) shows that structure-borne transmission dominates between 600 Hz and 3 kHz. At the trim panel's coincidence region, airborne and structure-borne transmissions are of the same order of magnitude.

Finally, the influence of mechanical links is analysed under structural excitation from the delta between uncoupled or coupling via isolators response compared to a baseline rigid coupling. Results for the double-wall with the aluminium and laminated composite skin panels are shown in Fig. 5.31 and Fig. 5.32 respectively. For the first case, SEA capture experimental trends between coupling via isolators and rigid coupling. The trends of the comparison between uncoupled and rigid couplings are also captured, however discrepancies are observed in mid frequencies since the SEA model overestimates the AMCE in this frequency range for the uncoupled configuration (as shown in Fig. 5.25). For the double-wall with the laminate skin panel, the model is able to predict experimental trends in the mid frequency range. Discrepancies at low frequencies are mainly due to the influence of stiffeners and at high frequencies to uncertainties in the trim's radiation efficiency and in the panels' damping loss factors.

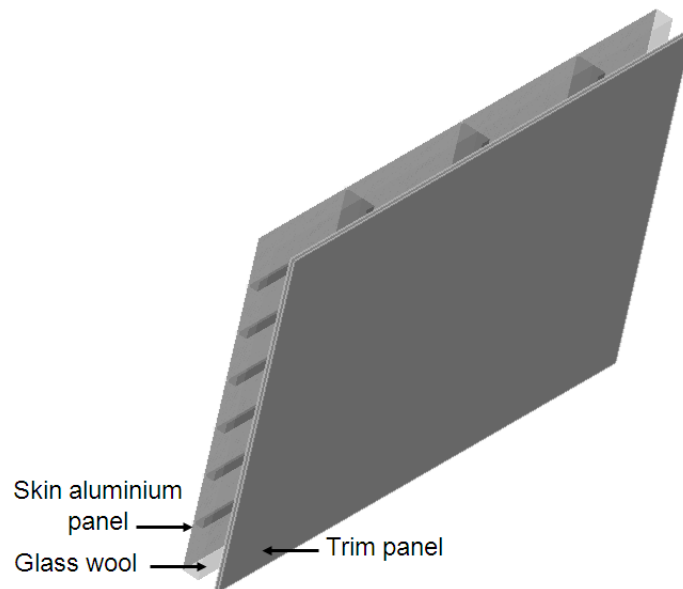


Figure 5.22 FEM representation of the double-wall system with the orthogonally stiffened aluminium panel.

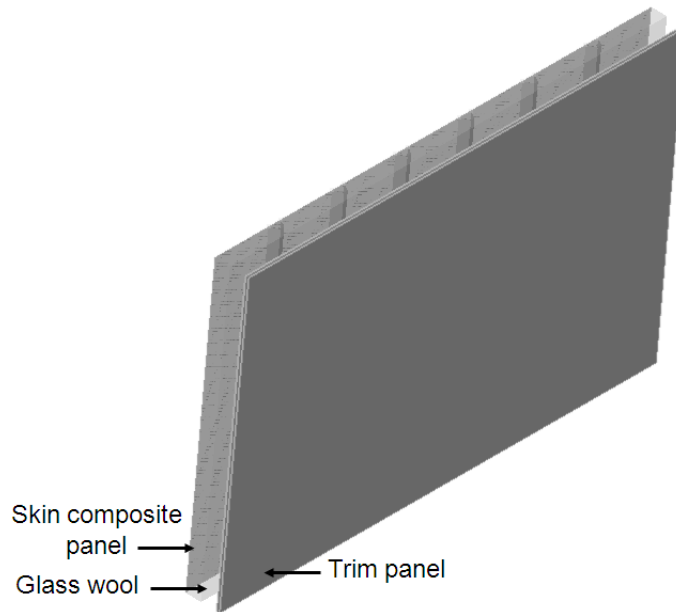


Figure 5.23 FEM representation of the double-wall system with the uni-directionally stiffened laminate composite panel.

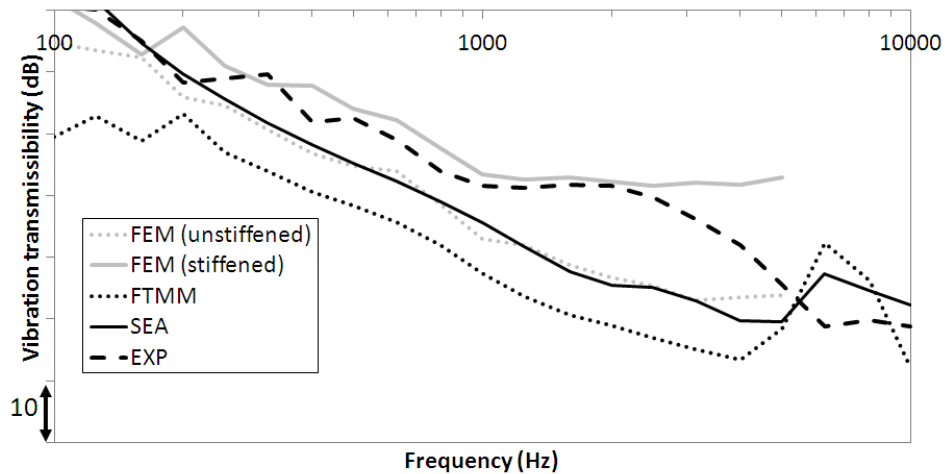


Figure 5.24 Vibration transmissibility of the uncoupled double-wall composed of the 2 mm stiffened aluminium panel, 2 in. of glass wool, 2 in. of air gap and the sandwich trim panel: comparisons between FEM, TMM, SEA and tests.

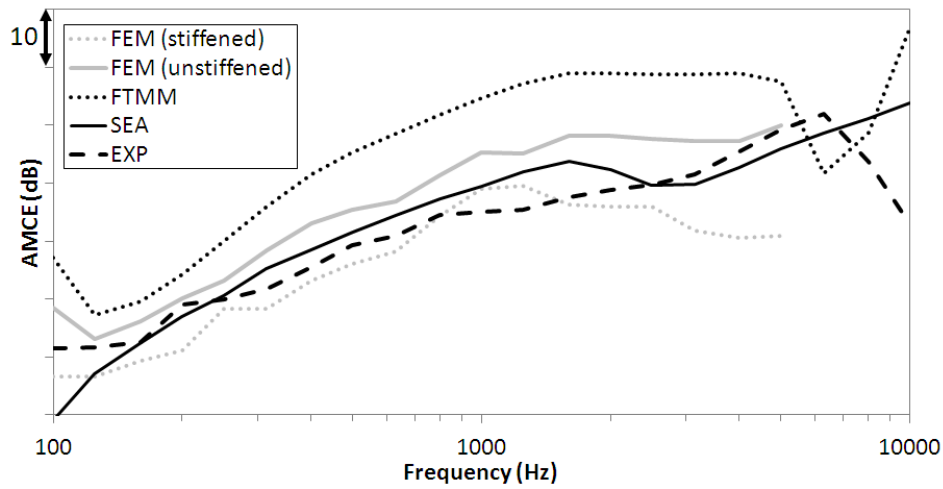


Figure 5.25 AMCE of the double-wall composed of the 2 mm stiffened aluminium panel, 2 in. of glass wool, 2 in. of air gap and the sandwich trim panel: comparisons between FEM, TMM, SEA and tests. Uncoupled configuration.

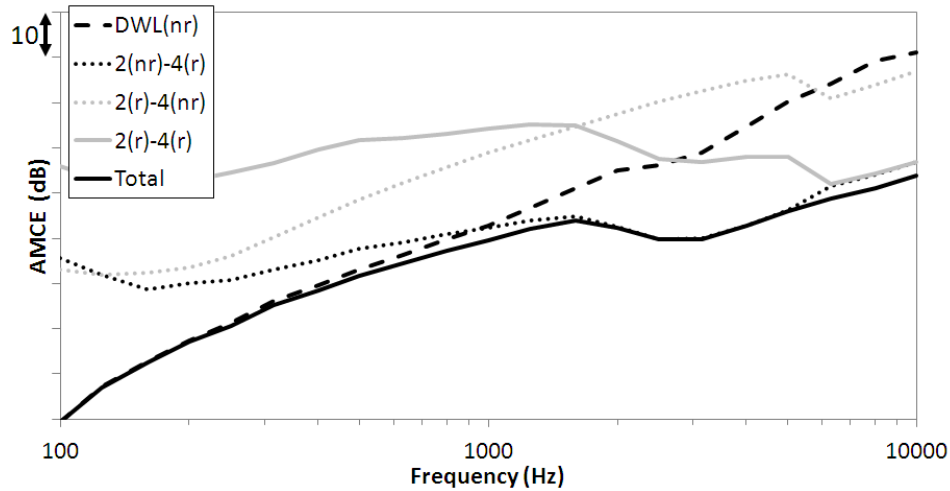


Figure 5.26 Transfer path analysis of the double-wall composed of the 2 mm stiffened aluminium panel, 2 in. of glass wool, 2 in. of air gap and the sandwich trim panel: uncoupled configuration.

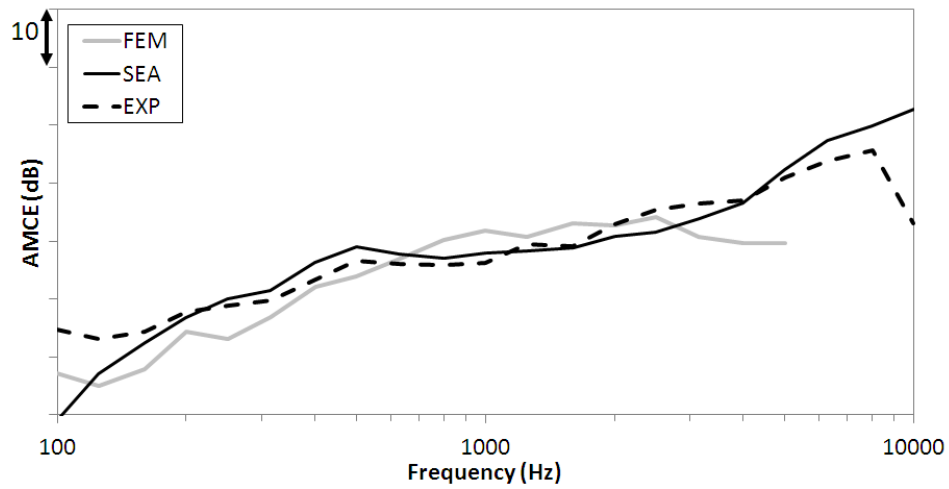


Figure 5.27 AMCE of the double-wall composed of the 2 mm stiffened aluminium panel, 2 in. of glass wool, 2 in. of air gap and the sandwich trim panel: comparisons between FEM, SEA and tests. Rigid coupling configuration.

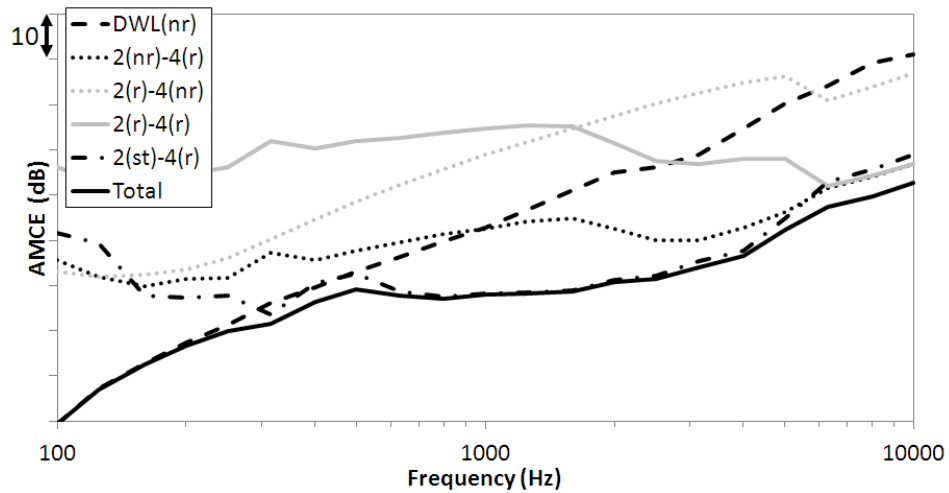


Figure 5.28 Transfer path analysis of the double-wall composed of the 2 mm stiffened aluminium panel, 2 in. of glass wool, 2 in. of air gap and the sandwich trim panel: rigid coupling configuration.

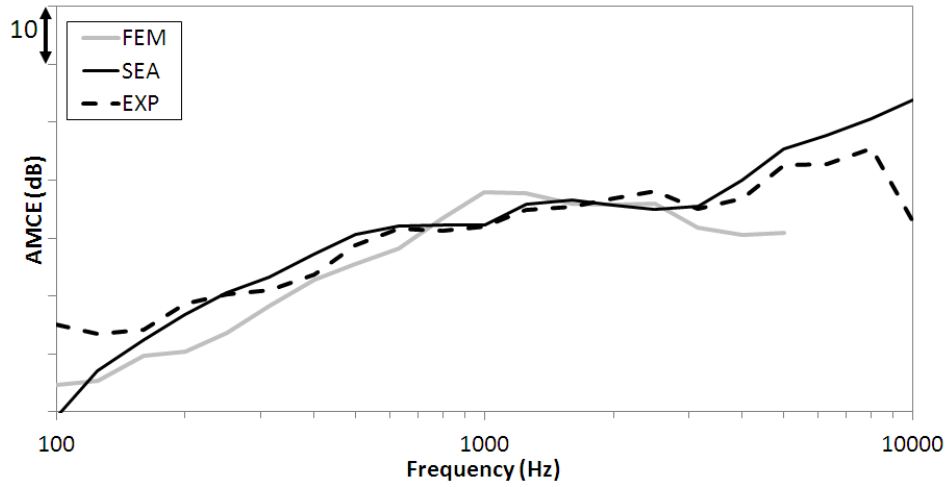


Figure 5.29 AMCE of the double-wall composed of the 2 mm stiffened aluminium panel, 2 in. of glass wool, 2 in. of air gap and the sandwich trim panel: comparisons between FEM, SEA and tests. Coupling via isolators configuration.

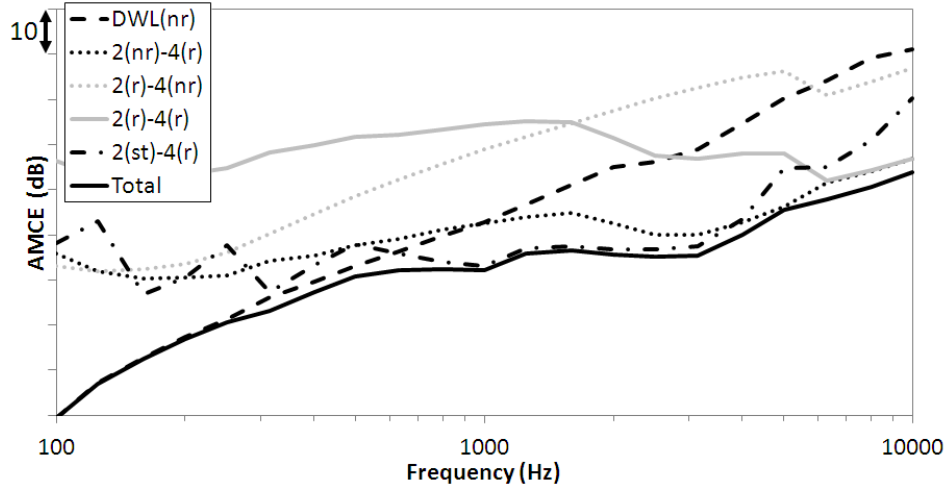


Figure 5.30 Transfer path analysis of the double-wall composed of the 2 mm stiffened aluminium panel, 2 in. of glass wool, 2 in. of air gap and the sandwich trim panel: comparisons between FEM, SEA and tests. Coupling via isolators configuration.

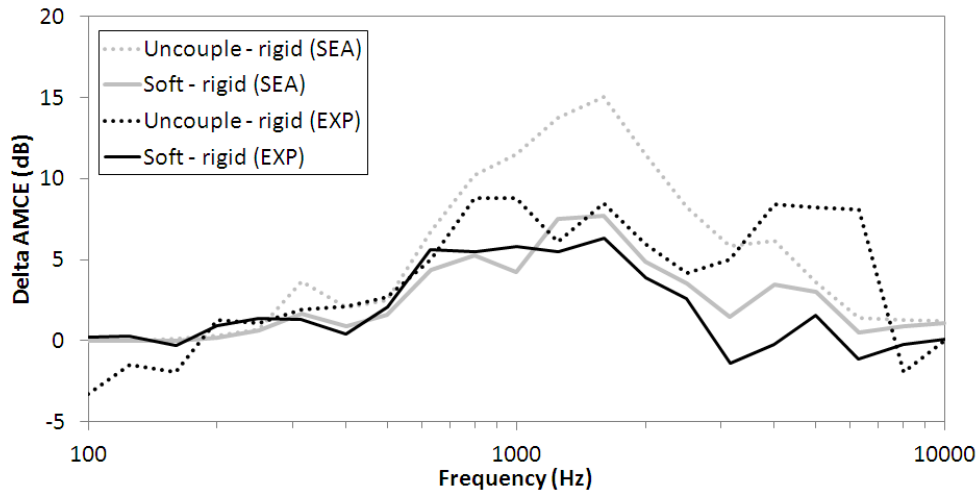


Figure 5.31 Influence of mechanical links on the AMCE of the double-wall composed of the 2 mm stiffened aluminium panel, 2 in. of glass wool, 2 in. of air gap and the sandwich trim panel: comparisons between SEA and tests.

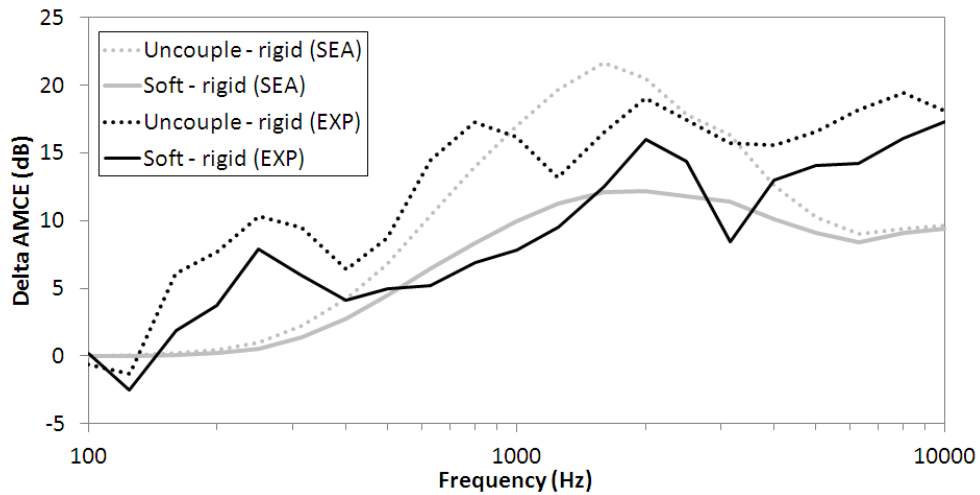


Figure 5.32 Influence of mechanical links on the AMCE of the double-wall composed of the 2.75 mm stiffened laminate panel, 2 in. of glass wool, 2 in. of air gap and the sandwich trim panel: comparisons between SEA and tests.



# CHAPTER 6

## GENERAL CONCLUSION AND FUTURE WORK

The main objective of this work was to develop a fast and accurate vibroacoustic model of aircraft double-walls for noise control optimisation to be used in the design & conception phases of an aircraft. Typical aircraft double-walls are composed of a stiffened aluminium or laminate composite panel (fuselage), a thermo-ponic insulation (porous layer) and a sandwich composite panel (trim). Both panels may be connected by rigid links or soft mounts. The developed approach is based on Statistical Energy Analysis (SEA) and integrates the modelling of: (1) isotropic, orthotropic and sandwich unstiffened flat panels, (2) porous layer by equivalent fluid or Biot theory, (3) mounts by a four-pole approach. The transmission through the double wall is studied under acoustic or mechanical excitation in the [100 Hz - 10 kHz] frequency range. The contributions to resonant and non-resonant transmission of airborne and structure-borne paths are identified.

The carried out research was divided into three specific tasks: (1) characterisation of the effects of porous materials compression on the sound transmission through the fuselage structure; (2) integration of the effect of mechanical links in the modelling of sound transmission through double-walls; (3) analysis of the transmission mechanisms and identification of dominant transmission paths under acoustic and structural excitations. In parallel, an extensive database of experimental results was acquired for validation purposes, comprising measurements on aircraft-representative single- and double-walls as well as on dynamic stiffness of shock mounts.

### Main achievements

First it has been shown that the compression of the porous layer against a single-wall decreases the transmission loss in the mid-frequency range up to 5 dB for a 50% compression rate. This is due to a resonance of the porous material, increasing the radiation efficiency. For an aircraft, the effect is found minor since the compression rate is much lower and occurs locally.

Concerning the structure-borne transmission through mounts, it is shown that a simple four-pole modelling using experimental dynamic stiffness is able to capture the trends. However, when connected through stiffeners, the latter should be accounted for as a dy-

dynamic element. The transmission via mounts is shown to be dominant in the mid-frequency range (around 1 kHz), for frequencies lower than the critical frequencies of the panels.

Comparisons between TMM and SEA for the prediction of transmission loss through structurally-decoupled double-walls under acoustic excitation show that the two approaches are in agreement. Additional experimental and numerical comparisons for an academic double-wall composed of two aluminium panels and a inner cavity, filled or not with porous materials (foam or fibrous), corroborate this conclusion. On the other hand, under structural excitation, TMM overestimates the ratio between transmitted and injected powers, due to limitations in assessing the non-resonant transmission under this type of excitation. SEA results are in better agreement with experiments when the non-resonant transmission paths are computed using an imposed velocity excitation.

Stiffeners have three main effects on the vibroacoustic behaviour of the double-wall: (1) they act as an added-mass and bending stiffness in the low frequency range; (2) they have a dynamic behaviour as part of the structural connection and (3) they increase the radiation into the inner cavity. Since the used TMM and SEA simulations of the double-wall do not integrate stiffeners, simulated TL overestimates test results over a large frequency range. However, the models are adapted to respond to industrial objectives such as (1) the prediction of differences in the TL between two configurations and (2) the prediction of the influence of structural transmission using the SEA model.

Finally, the benefit of decoupling elements is found maximum in the mid-frequency range (around 1 kHz). Similar trends are obtained under acoustic and structural excitations. However, in low and mid-frequencies (up to 2 kHz), decoupling via isolators is more efficient under structural excitation (around 2 dB). A transfer path analysis shows that at low frequencies, non-resonant transmission dominates up to around 1 kHz, from which structural transmission via links is preponderant. In the coincidence region of the skin panel and above, radiation due to airborne excitation dominates.

## Future work

The remaining open questions are related to the transposition of the modelling to in-flight conditions. Besides, correlation between experimental and numerical vibroacoustic approaches for a double-wall under turbulent boundary layer are still on debate, especially at high frequencies. On one side this is due to computational limitations and on the

other side to difficulties in reproducing experimentally the real excitation field. From the conclusions of the carried out research, several improvements of the double-wall modelling in line with in-flight aircraft applications are proposed hereafter.

In order to improve the double-wall sound transmission predictions, the modelling of stiffened panels is essential. The first step on the transposition of the modelling into aircraft level is to identify the limits of the model by comparisons with on ground measurements on real aircraft sidewalls. Then, the implementation of turbulent boundary layer excitation in the model is necessary to allow for predictions under flight conditions. Effects such as curvature and pressurization shall thus be studied. Moreover, a confidence interval for the theoretical results could be estimated based on uncertainties linked to input parameters.

Concerning links, applications could be foreseen for structures submitted to important loads in non-axial directions. In these cases, the non-axial terms of the dynamic stiffness, mainly linked to rotational and shear components, should be included in the model. For optimisation purposes, effects of temperature, pre-strain and excitation level on isolators' performance should be analysed. Finally, the effect at the structural resonance of the system composed by the skin, isolators and trim could be integrated in the dynamic stiffness feeding the four-pole model.

In regard to the experimental characterisation of panels, the measurement of input parameters, such as the modal density or the radiation efficiency should be improved, notably at high frequencies, for application or validation purposes on more complex structures. In addition, the measurement of damping loss factor in the coincidence region should be further investigated (e.g. the breakdown between internal and radiation loss factors).

Finally, the model could be extended to account for whole cockpit and cabin fuselage sections. Studies could be performed on the implementation, in the context of SEA, of other excitation fields, e.g. the environment control system (ECS) and noise due to the engine. In addition, since part of the transmission occurs through the windows, the impact of their contributions should also be evaluated.



# ANNEX A

## Principles for double-wall SEA modelling under aerodynamic excitation (turbulent boundary layer)

The SEA model developed in chapter 5 for double-walls under structural excitation could be extended to account for turbulent boundary layer excitation (TBL). Under TBL, the input power is given by [147]:

$$\Pi_2 = S_{pp}(\omega) \frac{\pi A_2}{m_2} n(\omega) j^2(\omega), \quad (\text{A.1})$$

where,  $S_{pp}$  is the power auto-spectral density of the fluctuating wall pressure,  $j^2 = \frac{1}{\Delta N} \sum_{mn} j_{mn}^2$  is the band averaged modal joint acceptance function,  $\Delta N$  is the number of modes in the frequency band and  $j_{mn}^2$  is the modal joint acceptance function. In space-frequency domain, the latter is given by:

$$j_{mm}^2 = \frac{1}{A_2^2} \int_{A_2} \int_{A_2} \phi_{mn}(x, y) \phi(\omega, x - x', y - y') \phi_{mn}(x', y') dA_2 dA_2', \quad (\text{A.2})$$

where,  $\phi_{mn}$  represents the panel's mode shapes and  $\phi(\omega, x - x', y - y')$  the spatial coherence of the cross-spectral density of the wall pressure. The latter is a function of the TBL model (e.g. Corcos [13, 46], Efimtsov [148], Cockburn-Robertson [149]). Finally,  $(x, y)$  and  $(x', y')$  are coordinates of two points on the panel. Closed form and numerical solutions are available [147].

The AMCE indicator can be used in order to compare sound transmission results under structural and TBL excitations. A transmission loss can also be derived in order to compare results with acoustic excitation:  $TL = 10 \log_{10} \left( \frac{\Pi_{in,eq}}{\Pi_{trans}} \right)$ , where  $\Pi_{in,eq}$  is the equivalent incident power (based on the analogy with a diffuse acoustic field). It is given by [6]:

$$\Pi_{in,eq} = \frac{S_{pp}(\omega)}{8\rho_0 c_0} A_2. \quad (\text{A.3})$$

The resonant transmission can be computed as for the case under structural excitation, presented in Chapter 5 (Fig. 5.17 and eq. (5.19)), by using the injected power estimated from eq. (A.1). The non-resonant transmission under TBL excitation should be further investigated. A first approximation is to consider the panels as a mass and to compute the non-resonant transmission coefficient using eq. (A.1). Supplementary analysis and

comparisons with FEM results are needed at this stage in order to adapt the formulation proposed in Fig. 5.18 for computations under TBL excitation.

# LIST OF REFERENCES

- [1] B. Efimtsov, L. Lazarev, Forced vibrations of plates and cylindrical shells with regular orthogonal system of stiffeners, *Journal of Sound and Vibration* 327 (1-2) (2009) 41 – 54.
- [2] C. Maury, P. Gardonio, S. J. Elliott, A wavenumber approach to modelling the response of a randomly excited panel, Part I: General theory, *Journal of Sound and Vibration* (2002) 83 – 113.
- [3] R. J. M. Craik, R. Wilson, Sound transmission through masonry cavity walls, *Journal of Sound and Vibration* 179 (1) (1995) 79 – 96.
- [4] P. Neple, Interior Noise and Sound Transmission, in *Encyclopedia of Aerospace Engineering*, John Wiley and Sons Ltd, 2010.
- [5] J.-F. Allard, N. Atalla, Propagation of sound in porous media: Modeling sound absorbing materials, 2nd edition, John Wiley & Sons Ltd, 2009.
- [6] O. Collery, Optimisation de la vérification de l'équation vibroacoustique des plaques sur un échantillonnage spatial, PhD dissertation, Institut National des Sciences Appliquées de Lyon, Lyon, France, 2010.
- [7] C. Guigou, C. Fuller, Control of aircraft interior broadband noise with foam-PVDF smart skin, *Journal of Sound and Vibration* 220 (3) (1999) 541 – 557.
- [8] J. Griffin, The control of interior cabin noise due to a turbulent boundary layer noise excitation using smart foam elements, Master's thesis, Virginia Polytechnic Institute, USA, Department of Mechanical engineering, 2006.
- [9] A. Kundu, A. Berry, Active control of transmission loss with smart foams, *The Journal of the Acoustical Society of America* 129 (2) (2011) 726–740.
- [10] J. Wilby, Aircraft interior noise, *Journal of Sound and Vibration* 190 (3) (1996) 545 – 564.
- [11] V. Kuznetsov, Noise control problems of passenger airplanes (A review), *Acoustical Physics* 49 (2003) 241–262.
- [12] C. Maury, P. Gardonio, S. J. Elliott, A wavenumber approach to modelling the response of a randomly excited panel, Part II: Application to aircraft panels excited by a turbulent boundary layer, *Journal of Sound and Vibration* (2002) 115 – 139.
- [13] G. M. Corcos, The structure of the turbulent pressure field in boundary-layer flows, *Journal of Fluid Mechanics* 18 (1964) 353 – 378.
- [14] W. W. Willmarth, Wall pressure fluctuations in a turbulent boundary layer, NACA Technical note 4139 .

- [15] W. W. Willmarth, Space-time correlations and spectra of wall pressure in a turbulent boundary layer, NACA Memorandum 3-17-59W .
- [16] M. K. Bull, Wall-pressure fluctuations beneath turbulent boundary layers: some reflections on the forty years of research, *Journal of Sound and Vibration* (1996) 299 – 315.
- [17] P. Neple, B. Campolina, J.-P. Coyette, Noise reduction of aircraft structures through aerodynamic (Corcos model) and acoustic excitation, *Proceedings of Noise-Con 08*, (2008) .
- [18] J. Wilby, F. Gloyna, Vibration measurements of an airplane fuselage structure II. Jet noise excitation, *Journal of Sound and Vibration* 23 (4) (1972) 467 – 486.
- [19] H. H. Hubbard, *Aeroacoustics of Flight Vehicles: Theory and Practice. Volume 1: Noise Sources, Theory and Practice* 1 (1258).
- [20] R. E. Hayden, B. S. Murray, M. A. Theobald, A study of interior noise levels, noise sources and transmission paths in light aircraft, NASA CR-172152 .
- [21] A. W. Leissa, *Vibration of plates*, NASA SP-160, 1969, Reprinted by The Acoustical Society of America, 1993.
- [22] M. Heckl, Wave Propagation on Beam-Plate Systems, *The Journal of the Acoustical Society of America* (1961) 640–651.
- [23] P. G. Bremner, Vibroacoustic of ribbed structures - a compact modal formulation for SEA models, *Noise-Con 94*, Ft. Lauderdale, Florida, USA .
- [24] W. Graham, A comparison of models for the wavenumber-frequency spectrum of turbulent boundary layer pressures, *Journal of Sound and Vibration* 206 (4) (1997) 541 – 565.
- [25] F. Han, L. G. Mongeau, R. J. Bernhard, A model for vibroacoustic response of plates excited by complex flows, *Journal of Sound and Vibration* 246 (5) (2001) 901 – 926.
- [26] B. Liu, L. Feng, A. Nilsson, Sound transmission through curved aircraft panels with stringer and ring frame attachments, *Journal of Sound and Vibration* (2007) 949 – 973.
- [27] A. Mejdi, N. Atalla, Dynamic and acoustic response of bidirectionally stiffened plates with eccentric stiffeners subject to airborne and structure-borne excitations, *Journal of Sound and Vibration* 329 (21) (2010) 4422 – 4439.
- [28] J. Legault, A. Mejdi, N. Atalla, Vibro-acoustic response of orthogonally stiffened panels: The effects of finite dimensions, *Journal of Sound and Vibration* 330 (24) (2011) 5928 – 5948.
- [29] S. Ghinet, N. Atalla, Vibro-acoustic behavior of multi-layer orthotropic panels, *Canadian Acoustics*, 30(3) (2002) 72–73.

- [30] S. Ghinet, N. Atalla, Vibro-acoustic behavior of flat sandwich composite panels, CSME Transactions (2006) vol. 30, Issue 4.
- [31] A. Mejudi, J. Legault, N. Atalla, Transmission loss of periodically stiffened laminate composite panels: Shear deformation and in-plane interaction effects, The Journal of the Acoustical Society of America 131 (1) (2012) 174–185.
- [32] S. Ghinet, N. Atalla, H. Osman, Diffuse field transmission into infinite sandwich composite and laminate composite cylinders, Journal of Sound and Vibration (2006) 745 – 778.
- [33] S. Ghinet, N. Atalla, H. Osman, The transmission loss of curved laminates and sandwich composite panels, The Journal of the Acoustical Society of America (2005) 774–790.
- [34] G. Maidanik, Response of ribbed panels to reverberant acoustic fields, Journal of Acoustical society of America, 34 (1962) 8029 – 826.
- [35] F. Fahy, P. Gardonio, Sound and Structural Vibration (Second Edition), Elsevier, Amsterdam, 2007.
- [36] C. Guigou-Carter, M. Villot, Modelling of Sound Transmission Through Lightweight Elements with Stiffeners, Building Acoustics 10 (3) (2003) 193 – 209.
- [37] P. Neple, F. Besluau, C. Lesueur, Stiffeners effect on sound transmission through complex aircraft structures, The 33rd International Congress and Exposition on Noise Control Engineering, (2004) .
- [38] C. Lesueur, Rayonnement acoustique des structures, Eyrolles, first edn., 1988.
- [39] P. Neple, J. Manera, N. Pellegrin, J.-P. Coyette, Stiffeners effect on sound transmission through a thin plate excited by a turbulent boundary layer (corcos model) - comparison with a diffuse sound field, Proceedings of the 14th International Congress of Sound and Vibration, Cairns, Australia .
- [40] L. R. Koval, Effect of air flow, panel curvature, and internal pressurization on field-incidence transmission loss, The Journal of the Acoustical Society of America 59 (6) (1976) 1379–1385.
- [41] L. R. Koval, On sound transmission into a stiffened cylindrical shell with rings and stringers treated as discrete elements, Journal of Sound and Vibration 71 (4) (1980) 511 – 521.
- [42] P. Ramachandran, S. Narayanan, Evaluation of modal density, radiation efficiency and acoustic response of longitudinally stiffened cylindrical shell, Journal of Sound and Vibration 304 (1-2) (2007) 154 – 174.
- [43] A. Pellicier, N. Trompette, A review of analytical methods, based on the wave approach, to compute partitions transmission loss, Applied Acoustics (2007) 1192 – 1212.

- [44] J. S. Bolton, N. M. Shiau, Y. J. Kang, Sound transmission through multi-panel structures lined with elastic porous materials, *Journal of Sound and Vibration* (1996) 317 – 347.
- [45] M. Norton, D. Karczub, *Fundamentals of Noise and Vibration Analysis for Engineers*, Cambridge University Press, 2nd edn., 2003.
- [46] G. M. Corcos, Resolution of Pressure in Turbulence, *The Journal of the Acoustical Society of America* (1963) 192–199.
- [47] B. Brouard, D. Lafarge, J. F. Allard, A general method of modelling sound propagation in layered media, *Journal of Sound and Vibration* 183 (1) (1995) 129 – 142.
- [48] M. Villot, C. Guigou, L. Gagliardini, Predicting the acoustical radiation of finite size multi-layered structures by applying spatial windowing on infinite structures, *Journal of Sound and Vibration* 245 (3) (2001) 433 – 455.
- [49] D. Rhazi, N. Atalla, A simple method to account for size effects in the transfer matrix method, *The Journal of the Acoustical Society of America* 127 (2) (2010) EL30–EL36.
- [50] T. E. Vigran, Sound transmission in multilayered structures - Introducing finite structural connections in the transfer matrix method, *Applied Acoustics* (2010) 39 – 44.
- [51] B. H. Sharp, Prediction methods for the sound transmission of building elements, *Noise Control Engineering Journal* 11 (1978) 53 – 63.
- [52] T.E., Vigran, Sound insulation of double-leaf walls - Allowing for studs of finite stiffness in a transfer matrix scheme, *Applied Acoustics* 71 (7) (2010) 616 – 621.
- [53] R. H. Lyon, R. G. DeJong, *theory and application of statistical energy analysis*, Butterworth-Heinemann, Boston, 2nd edn., 1995.
- [54] M. J. Crocker, A. J. Price, Sound transmission using statistical energy analysis, *Journal of Sound and Vibration* (1969) 469 – 486.
- [55] F. Fahy, *Statistical Energy Analysis - A Guide for Potential Users*, Institute of Sound and Vibration Research, University of Southampton, UK, URL <http://www.seanet.be>, 2002.
- [56] F. Fahy, *Statistical Energy Analysis: A Critical Overview*, *Philosophical Transactions: Physical Sciences and Engineering* (1994) 431–447.
- [57] A. J. Price, M. J. Crocker, Sound Transmission through Double Panels Using Statistical Energy Analysis, *The Journal of the Acoustical Society of America* 47 (3A) (1970) 683–693.
- [58] S. Schoenwald, Flanking sound transmission through lightweight framed double leaf walls: Prediction using statistical energy analysis, PhD dissertation, Technische Universiteit Eindhoven, Eindhoven, The Netherlands, 2008.

- [59] T. Wang, J. Maxon, Application of statistical energy analysis and optimization in the design of Gulfstream large-cabin aircraft interior thermal/acoustic package, INCE Conference Proceedings 210 (1) (2008) 2073–2084.
- [60] B. L. Clarkson, R. J. Pope, Experimental determination of modal densities and loss factors of flat plates and cylinders, *Journal of Sound and Vibration* (1981) 535 – 549.
- [61] J. Legault, N. Atalla, Numerical and experimental investigation of the effect of structural links on the sound transmission of a lightweight double panel structure, *Journal of Sound and Vibration* 324 (3-5) (2009) 712 – 732.
- [62] J. Legault, N. Atalla, Sound transmission through a double panel structure periodically coupled with vibration insulators, *Journal of Sound and Vibration* 329 (15) (2010) 3082 – 3100.
- [63] M. Bolduc, Acquiring Statistical Energy Analysis Damping Loss Factor for Complex Structures with Low to High Damping Characteristics, PhD dissertation, University of Sherbrooke, Sherbrooke, Quebec, Canada, Department of Mechanical engineering, 2007.
- [64] D. A. Bies, S. Hamid, In situ determination of loss and coupling loss factors by the power injection method, *Journal of Sound and Vibration* (1980) 187 – 204.
- [65] N. Lalor, Practical Considerations for The Measurement of Internal and Coupling Loss Factors on Complex Structures, ISVR Technical Report No 182 .
- [66] N. Lalor, The Practical Implementation of SEA, Proceedings of the IUTAM symposium on SEA (1997) 257–268.
- [67] K. Renji, M. Mahalakshmi, High frequency vibration energy transfer in a system of three plates connected at discrete points using statistical energy analysis, *Journal of sound and vibration* (2006) 539–553.
- [68] R. Craik, Sound Transmission Paths through statistical energy analysis model, *Applied Acoustics* 30 (1990) 45 – 55.
- [69] E. Davis, By Air By SEA, *Sound and Vibration Magazine* 2005 .
- [70] J. A. Lin, Airplane Interior Noise Modeling Using a Statistical Energy Analysis Approach, AIAA Aeroacoustics Conference and Exhibit 1999 .
- [71] J. Cordioli, S. Gerges, A. Pererira, M. Carmo, C. Grandi, Vibro-Acoustic Modeling of Aircrafts Using Statistical Energy Analysis, SAE Technical Paper 2004-01-3337 .
- [72] J. Cordioli, F. Klug, S. Gerges, M. Santos, R. de Mello, Vibro-Acoustic Modeling of Aircrafts Using Statistical Energy Analysis, SAE Technical Paper 2008-36-0066 .
- [73] V. Cotoni, B. Gardner, J. Carneal, C. Fuller, Modeling methods for vibro-acoustic analysis of commercial aircrafts, Proceedings of Noise-Con 07, (2007) .

- [74] I. Dandaroy, D. Hartley, R. Hund, Interior noise prediction of Hawker Horizon aircraft using Statistical Energy Analysis, INCE Conference Proceedings 113 (1) (2004) 333–346.
- [75] J. W. Maxon, J. A. Malluck, Application of statistical energy analysis and optimization in the design of Gulfstream’s G150 interior thermal/acoustic package, INCE Conference Proceedings 115 (1) (2006) 3011–3020.
- [76] M. Moeller, M. Gmerek, A. Nagi, Power Transfer Functions for Aircraft Statistical Energy Analysis Model Validation, AIAA Aeroacoustics Conference and Exhibit 2009 .
- [77] A. Peiffer, S. Tewes, Interior noise prediction of aircraft section using hybrid FEM/SEA methods, Proceedings of Noise-Con 08, (2008) .
- [78] B. H. Sharp, A study of techniques to increase the sound insulation of building elements, Wyle Laboratories Report WR73-5, El Segundo, CA, USA, 1973.
- [79] Q. Gu, J. Wang, Effect of resilient connection on sound transmission loss of metal stud double panel partitions, Chinese Journal of Acoustics 2 (1983) 113 – 126.
- [80] J. L. Davy, Predicting the sound insulation of stud walls, Proceedings of Internoise 91, vol. 1, Sydney, Australia (1991) 251 – 254.
- [81] The sound transmission of cavity walls due to studs, Proceedings of Internoise 93, vol. 1 (1993) 975 – 978.
- [82] B. A. J. Mustafa, R. Ali, Prediction of natural frequency of vibration of stiffened cylindrical shells and orthogonally stiffened curved panels, Journal of Sound and Vibration 113 (1987) 317 – 327.
- [83] M. Barrette, A. Berry, O. Beslin, Vibration of stiffened plates using hierarchical trigonometric functions, Journal of Sound and Vibration 235 (8) (2000) 727 – 747.
- [84] D. W. Fox, V. G. Sigillito, Bounds for frequencies of rib reinforced plates, Journal of Sound and Structural vibration 69 (4) (1982) 497 – 507.
- [85] D. W. Fox, V. G. Sigillito, Bounds for eigen frequencies of a plate with an elastically attached reinforcing rib, International Journal of Solids and Structures 18 (3) (1982) 235 – 247.
- [86] E. J. Sapountzakis, J. T. Katsikadelis, Dynamic analysis of elastic plates reinforced with beams of doubly-symmetrical cross section, Computational Mechanics 23 (5-6) (1999) 430 – 439.
- [87] V. Cotoni, P. J. Shorter, R. S. Langley, Numerical and experimental validation of a hybrid finite element-statistical energy analysis method, The Journal of the Acoustical Society of America (2007) 259 – 270.
- [88] V. Cotoni, R. S. Langley, P. J. Shorter, A statistical energy analysis subsystem formulation using finite element and periodic structure theory, Journal of Sound and Vibration 318 (2008) 1077 – 1108.

- [89] R. S. Langley, P. J. Shorter, The wave transmission coefficients and coupling loss factors of point connected structures, *The Journal of the Acoustical Society of America* (2003) 1947 – 1964.
- [90] P. J. Shorter, R. S. Langley, On the reciprocity relationship between direct field radiation and diffuse reverberant loading, *The Journal of the Acoustical Society of America* (2005) 85–95.
- [91] P. J. Shorter, V. Cotoni, R. S. Langley, Numerical and Experimental Validation of Hybrid FE-SEA Method, *Proceedings of Noise-Con 04* (2004) 380 – 388.
- [92] P. J. Shorter, R. S. Langley, Modeling structure-borne noise with the hybrid FE-SEA method, *Proceedings of Eurodyn 05* (2005) 1205 – 1210.
- [93] P. J. Shorter, R. S. Langley, Vibro-acoustic analysis of complex systems, *Journal of Sound and Vibration* (2005) 669 – 699.
- [94] E. Poulain, *Approches de modélisation hybrides pour la prédiction du bruit solide dans les structures aéronautiques*, Master thesis, University of Sherbrooke, Sherbrooke, Quebec, Canada, 2008.
- [95] B. Castagnède, A. Aknine, B. Brouard, V. Tarnow, Effects of compression on the sound absorption of fibrous materials, *Applied Acoustics* 61 (2) (2000) 173 – 182.
- [96] C. Zwikker, C. W. Kosten, *Sound absorbing materials*, Elsevier Publishing Co., New York, 1949.
- [97] K. Attenborough, Acoustical characteristics of rigid fibrous absorbents and granular materials, *The Journal of the Acoustical Society of America* 73 (3) (1983) 785–799.
- [98] D. L. Johnson, J. Koplik, R. Dashen, Theory of dynamic permeability and tortuosity in fluid-saturated porous media, *Journal of Fluid Mechanics Digital Archive* 176 (-1) (1987) 379–402.
- [99] R. Panneton, Comments on the limp frame equivalent fluid model for porous media, *The Journal of the Acoustical Society of America* 122 (6) (2007) EL217–EL222.
- [100] O. Doutres, N. Dauchez, J.-M. Génevaux, O. Dazel, Validity of the limp model for porous materials: A criterion based on the Biot theory, *The Journal of the Acoustical Society of America* 122 (4) (2007) 2038–2048.
- [101] O. Doutres, N. Dauchez, J.-M. Génevaux, O. Dazel, A Frequency Independent Criterion for Describing Sound Absorbing Materials by a Limp Frame Model, *Acta Acustica united with Acustica* 95 (1) (2009) 178–181.
- [102] B. Castagnède, J. Tizianel, A. Moussatov, A. Aknine, B. Brouard, Parametric study of the influence of compression on the acoustical absorption coefficient of automotive felts, *Comptes Rendus de l'Académie des Sciences - Series IIB - Mechanics* 329 (2) (2001) 125 – 130.
- [103] C.-N. Wang, Y.-M. Kuo, S.-K. Chen, Effects of compression on the sound absorption of porous materials with an elastic frame, *Applied Acoustics* 69 (1) (2008) 31 – 39.

- [104] N. Atalla, R. Panneton, P. Debergue, A mixed displacement-pressure formulation for poroelastic materials, *The Journal of the Acoustical Society of America* 104 (3) (1998) 1444–1452.
- [105] O. Dazel, B. Brouard, C. Depollier, S. Griffiths, An alternative Biot’s displacement formulation for porous materials, *The Journal of the Acoustical Society of America* 121 (6) (2007) 3509–3516.
- [106] F. Petrone, M. Lacagnina, M. Scionti, Dynamic characterization of elastomers and identification with rheological models, *Journal of Sound and Vibration* 271 (1-2) (2004) 339 – 363.
- [107] L. R. Miller, M. Ahmadian, Active mounts - A discussion of future technological trends, Lord Corporation, Thomas Lord Research Center, 405 Gregson Drive, Cary NC 27511 .
- [108] ISO 10846-1, Acoustics and vibration – Laboratory measurement of vibro-acoustic transfer properties of resilient elements – Part 1: Principles and guidelines, International Organization for Standardization, Geneva, Switzerland, 2008-08-05 .
- [109] ISO 10846-2, Acoustics and vibration – Laboratory measurement of vibro-acoustic transfer properties of resilient elements – Part 2: Direct method for determination of the dynamic stiffness of resilient supports for translatory motion, International Organization for Standardization, Geneva, Switzerland, 2008-08-05 .
- [110] ISO 10846-3, Acoustics and vibration – Laboratory measurement of vibro-acoustic transfer properties of resilient elements – Part 3: Indirect method for determination of the dynamic stiffness of resilient supports for translatory motion, International Organization for Standardization, Geneva, Switzerland, 2007-12-17 .
- [111] ASD-STAN prEN 4662, Aerospace series test specification for vibration control components, Aerospace and defense industries association of Europe - Standardization, Brussels, Belgium, 2009-03-31 .
- [112] T. R. Lin, N. H. Farag, J. Pan, Evaluation of frequency dependent rubber mount stiffness and damping by impact test, *Applied Acoustics* (2005) 829 – 844.
- [113] Y. Yu, N. G. Naganathan, R. V. Dukkipati, A literature review of automotive vehicle engine mounting systems, *Mechanism and Machine Theory* (2001) 123 – 142.
- [114] J. Zhang, C. M. Richards, Dynamic analysis and parameter identification of a single mass elastomeric isolation system using Maxwell Voigt model, *ASME Journal of Vibration and Acoustics* (2006) 713–721.
- [115] J. Zhang, C. M. Richards, Parameter identification of analytical and experimental rubber isolators represented by Maxwell models, *Mechanical Systems and Signal Processing* (2007) 2814 – 2832.
- [116] N. Vahdati, L. K. L. Saunders, High frequency testing of rubber mounts, *ISA Transactions* (2002) 145 – 154.

- [117] B. Gardner, P. Shorter, V. Cotoni, Modeling vibration isolators at mid and high frequency using Hybrid FE-SEA analysis, Proceedings of Internoise (2005), Rio de Janeiro, Brazil .
- [118] I. L. Hidalgo, A. Nabarrete, M. Santos, Structure-borne transmissibility evaluation through modeling and analysis of aircraft vibration dampers, *Journal of Aerospace Technology and Management* 3 (2) (2011) 147 – 158.
- [119] D. Thorby, *Structural dynamics and vibration in practice*, Butterworth-Heinemann, first edn., 2008.
- [120] M. R. Schroeder, Binaural dissimilarity and optimum ceilings for concert halls: More lateral sound diffusion, *The Journal of the Acoustical Society of America* 65 (4) (1979) 958–963.
- [121] F. P. Mechel, The Wide-angle Diffuser a Wide-angle Absorber?, *Acta Acustica united with Acustica* 81 (4) (1995) 379–401.
- [122] L. Beranek, L. Istvan, *Noise and vibration control Engineering: Principles and applications*, John Wiley and Sons Inc., New York, New York, 1992.
- [123] W. Frommhold, H. Fuchs, S. Sheng, Acoustic Performance of Membrane Absorbers, *Journal of Sound and Vibration* 170 (5) (1994) 621 – 636.
- [124] M. R. Stinson, G. A. Daigle, Electronic system for the measurement of flow resistance, *The Journal of the Acoustical Society of America* 83 (6) (1988) 2422–2428.
- [125] N. Dauchez, M. Etchessahar, S. Sahraoui, On measurement of mechanical properties of sound absorbing materials, 2nd Biot Conference on Poromechanics .
- [126] B. Brouard, D. Lafarge, J. F. Allard, A general method of modelling sound propagation in layered media, *Journal of Sound and Vibration* 183 (1) (1995) 129 – 142.
- [127] M. Villot, C. Guigou, L. Gagliardini, Predicting the acoustical radiation of finite size multi-layered structures by applying spatial windowing on infinite structures, *Journal of Sound and Vibration* 245 (3) (2001) 433 – 455.
- [128] F. J. Fahy, *Sound intensity*, Elsevier Applied Science, London, 1989.
- [129] D. Rhazi, N. Atalla, Transfer matrix modelling of the vibroacoustic response of multi-materials structures under mechanical excitation, *Journal of Sound and Vibration* 329 (2010) 2532–2546.
- [130] O. Doutres, N. Dauchez, J.-M. Génevaux, Porous layer impedance applied to a moving wall: Application to the radiation of a covered piston, *The Journal of the Acoustical Society of America* 121 (1) (2007) 206–213.
- [131] O. Doutres, N. Atalla, Experimental estimation of the transmission loss contributions of a sound package placed in a double wall structure, *Applied Acoustics* 72 (6) (2011) 372 – 379.

- [132] R. Craik, R. Wilson, Sound transmission through masonry cavity walls, *Journal of Sound and Vibration* 179 (1) (1995) 79 – 96.
- [133] J. Poblet-Puig, A. Rodriguez-Ferran, C. Guigou-Carter, M. Villot, The Role of Studs in the Sound Transmission of Double Walls, *Acta Acustica united with Acustica* 95 (2009) 555–567(13).
- [134] M. Ewing, K. Vatti, I. Vaz, Coupling loss factor estimation for plates joined at a point: Analysis and experiment, *Proceedings of Noise-con* (2010), Baltimore, USA .
- [135] T. Wang, J. Maxon, Isolator modeling in SEA, *Proceedings of Internoise* (2010), Lisbon, Portugal .
- [136] L. Kari, Dynamic transfer stiffness measurements of vibration isolators in the audible frequency range, *Noise Control Engineering Journal* 49 (2001) 88–102.
- [137] S. Ghinet, N. Atalla, Vibro-acoustic behaviors of flat sandwich composite panels, *CSME Journal* 30(4) (2006) 473–493.
- [138] B. Cimerman, T. Bharj, G. Borello, Overview of the Experimental Approach to Statistical Energy Analysis, *SAE Technical papers* .
- [139] T. Zmijevski, J. Weisbeck, R. Sanetick, Structureborne noise control of oscillating pumps, *Proceedings of Internoise* (2009), Ottawa, Canada .
- [140] V. Hongisto, Sound insulation of double panels - comparison of existent prediction models, *Acta Acustica* 92 92 (2006) 61 – 78.
- [141] R. J. M. Craik, Non-resonant sound transmission through double walls using statistical energy analysis, *Applied Acoustics* 64 (3) (2003) 325 – 341.
- [142] H. Kuttruff, *Room acoustics*, Applied Science Publishers, London, UK, 1979.
- [143] F. G. Leppington, E. G. Broadbent, K. H. Heron, The Acoustic Radiation Efficiency of Rectangular Panels, *Proceedings of the Royal Society of London. A. Mathematical and Physical Sciences* 382 (1982) 245–271.
- [144] ISO 15186-1:2000, *Acoustics – Measurement of sound insulation in buildings and of building elements using sound intensity – Part 1: Laboratory measurements*, 2000.
- [145] B. Campolina, N. Atalla, N. Dauchez, P. Neple, Validation of a four-pole modelling for coupling loss factor between two plates connected via vibration isolators under mechanical excitation, *Proceedings of Noise-Con* (2011), Portland, USA .
- [146] P. Neple, B. Campolina, N. Atalla, M. Bolduc, Sound transmission through double wall aircraft structures: Effect of attachments and sensitivity to the assembly characteristics and the excitation field, *Proceedings of Noise-Con* (2011), Portland, USA .
- [147] A. Mejdj, *Etude numérique et expérimentale de la réponse vibro-acoustique des structures raidies à des excitations aériennes et solidiennes*, PhD dissertation, Uni-

versity of Sherbrooke, Sherbrooke, Quebec, Canada, Department of Mechanical engineering, 2011.

- [148] B. M. Efimtsov, Characteristics of the field of turbulent wall pressure fluctuations at large Reynolds numbers, *Soviet Physics Acoustics* 28 (4) (1982) 289 – 292.
- [149] J. Cockburn, J. Robertson, Vibration response of spacecraft shrouds to in-flight fluctuating pressures, *Journal of Sound and Vibration* 33 (4) (1974) 399 – 425.





